Low temperature synthesis and cold sintering of natural source derived hydroxyapatite for bone tissue engineering applications

Anna Galotta

September 2023

Low temperature synthesis and cold sintering of natural source derived hydroxyapatite for bone tissue engineering applications

Anna Galotta

anna.galotta@unitn.it

Approved by

Prof. Vincenzo Maria Sglavo
Department of Industrial Engineering
University of Trento

PhD Commitee

Prof. Gian Domenico Sorarù
Department of Industrial Engineering
University of Trento

Prof. Cekdar Vakif Ahmetoglu
Department of Materials Science and Engineering
Izmir Institute of Technology

Prof. Christophe Drouet
CIRIMAT
University of Toulouse

University of Trento - Department of Industrial Engineering

Doctoral Thesis

Anna Galotta – September 2023

Published in Trento (Italy) – by University of Trento

Abstract

The present thesis work is focused on the low-temperature transformation of food industry wastes like mussel shells into nanocrystalline ions-substituted hydroxyapatite powder, having similarities with natural bone apatite, on the consolidation of such powder by cold sintering, and on the physicochemical characterization of the raw materials, synthesised powders and sintered pellets. Nonetheless the evaluation of the mechanical and biological properties was carried out to address cold sintered bodies to possible scaffolds for bone tissue engineering applications.

Mussel shells, like other biogenic source of calcium carbonate/phosphate, have the attractive of being a "zero"-cost raw material because they are a waste, but also of having trace elements (Mg, Na, Sr, etc.) which, if found in a bioceramic, have a positive effect on the biological properties. Therefore, mussel shell-derived hydroxyapatite could resemble the mineralized bone tissue, being natural apatite nanometric, ion substituted and with low crystalline tenor.

In the first part of the manuscript, two production methods were explored: mechanochemistry and dissolution-precipitation synthesis. Mechanochemistry was carried out at room temperature by directly mixing crushed mussel shells with phosphoric acid in a ball mill. Nanocrystalline multi-ions substituted hydroxyapatite was produced after 4 h of milling and drying at 150°C. Conversely, dissolution-precipitation synthesis was carried out in two steps: the dissolution of crushed mussel shells by adding phosphoric and chloric acid occurred at room temperature, whereas the precipitation of calcium phosphates induced by soda solution, occurred at 45°C. Dissolution-precipitation was further implemented to produce a homogeneous composite material in a single-step by introducing chitosan (in a 2/5/10 wt%)

during the dissolution step. The idea was to produce a composite material able to mimic the natural bone tissue composition.

In the second part of the manuscript, cold sintering was investigated for the consolidation of the synthesised hydroxyapatite and hydroxyapatite-based composites at a maximum temperature of 200 °C to avoid phase transformation, limit grain growth and preserve the osteoconduction of the bioceramic materials. The effect of the main process parameters such as solvent amount, pressure, temperature and holding time was discussed. Pressure-solution creep and plastic deformation were pointed out as the fundamental consolidation mechanisms in cold sintering, the pressure playing the major role. With a synergistic combination of pressure (600 MPa), temperature (200°C) and liquid phase (20 wt%) it was possible to consolidate hydroxyapatite above 80% relative density in only 15 min. Furthermore, pressure and temperature act a complementary agent during cold sintering. In fact, it was possible to consolidate nanometric HAp and HAp/chitosan composites above 90% relative density by increasing the applied pressure up to 1.5 GPa at room temperature.

The mechanical properties of cold sintered pellets were investigated, and resulted in a flexural bending strength and Vickers microhardness, respectively, of 45 MPa and 1.1 GPa for pure hydroxyapatite and of 55 MPa and 0.8 GPa for HAp/chitosan composite.

In the frame of bone tissue engineering applications, cold sintered bodies were also preliminarily tested in vitro to establish their bioactivity, their cellular viability through cytotoxicity assessment, and the ability to sustain cells adhesion, osteogenic differentiation. And extracellular matrix mineralization.

Table of Contents

Chapter I Introduction

Dealing with bone tissue engineering implies a multidisciplinary approach where biology, physics, chemistry, medicine, material science, engineering, and technology combine together to design functional biological substitutes able to restore or improve the function of damaged tissues [1]–[3]. However, the present thesis work will mainly focus on the bioceramics and the processing routes to manufacture bone scaffolds from discarded biogenic sources. The incoming sections will first briefly describe the motivations behind skeletal tissue engineering, the main features of bone tissue biology, the material selection within bone tissue engineering with a special attention to calcium phosphates and their biogenic sources. The frame of this thesis will be then completed by a brief overview of low temperature synthesis and cold sintering.

1.1. Skeletal tissue engineering

The clinical need for bone grafts to sustain and help bone tissue reconstruction and, possibly, regeneration is due to the increasing geriatric population and to the growing cases of bone diseases such as injuries, fractures, tumours, traumas, etc [4]–[6]. In 2021 the global market for bone grafts and substitutes overcame US$ 2.5 billion and it is foreseen to reach US$ 4.5 billion by 2031 [7].

Bone is a self-healing tissue, but when it comes to critical defects (i.e. larger than 2 cm in diameter [4], [6]) bone is incapable to repair the damage alone, and therefore bone grafting is the only solution [5]. Hitherto, four main strategies have been pursued for bone grafting: autogenous, allogeneic, xenogeneic bone grafts and synthetic bioengineered scaffolds [5], [8]–[10]. Shortly, autografting consists in collecting fresh bone tissue from the patient himself. The fresh tissue harvesting usually occurs at the iliac crest. Autogenous bone grafting is considered the gold standard, because it is naturally osteogenic, osteoinductive and osteoconductive, it has the lowest risk of post-implantation rejection, but it implies multiple surgery operations for the patient with consequent possibility of infections, and the self-harvested tissue might be insufficient to repair large defects [1], [8], [9].

To overcome such limitations, allogeneic bone grafts were introduced. In this case, bone tissue is transplanted from human cadavers, and it eliminates the drawback of donor site morbidity and availability of new tissue even for large and complex bone injuries, but of course the risk of immunological rejection increases as well as the probability of infections and disease transmission [1], [8]. The use of animal-derived bone grafts (xenografts) has also been explored [11]–[13], especially bovine bones due to their similarity with human bones [13], [14]. However, both allografts and xenografts may also be limited by ethical and religious concerns [15]–[19]. Therefore, the development of artificial bone grafts able to mimic native tissue composition, structure, biological and mechanical properties has become a major priority in the last 40 years [1], [2], [10], [20]. In this scenario, the three cornerstone of bone tissue engineering (biomaterials, cells and factors therapy) should all be involved and combined synergistically [1]. Due to the complexity of native bone tissue and beyond the composition and the structure of biomaterial scaffolds, it is fundamental to investigate their interactions with (stem) cells, the mechanical stimuli they can trigger and support [4], [20], in order to improve the integration of the designed scaffold within the host tissue. The tremendous advances achieved in the recent years in biology, medicine, biotechnology and biomaterial science open to new frontiers and encouraging outcomes within bone tissue engineering (BTE), even if the faithfully mimicking of bone tissue complexity is still a bright challenge.

1.1.1. Bone tissue biology

In order to properly design a compelling bioengineered scaffold able to successfully reconstruct damaged bone tissue, it is essential to comprehend the main features of bone tissue biology, including composition, structure, functions and properties [9]. Bone is a hard, highly vascularized and dynamic tissue, which plays fundamental roles within the human body such as structural support, motion, protection, mineral homeostasis regulator, haematopoiesis [1], [6], [21]. Bone structure is hierarchical, highly organized from macro to nanoscale [1], as shown in Figure 1.

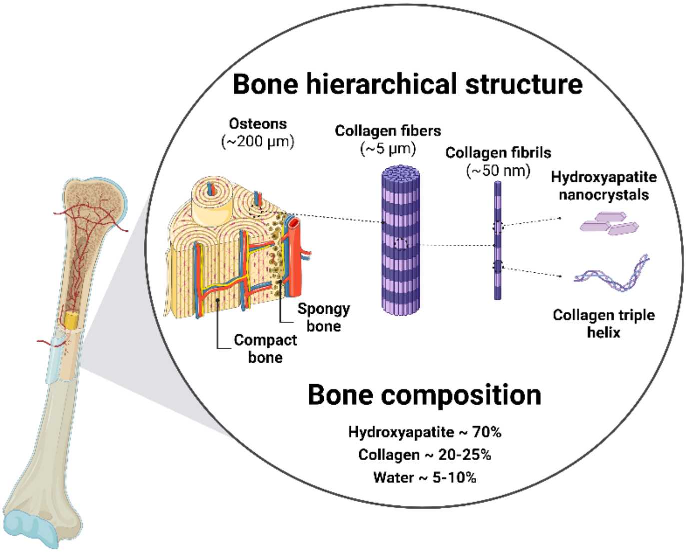

Figure 1 Bone hierarchical structure.

Bone can be classified into cancellous (or spongy) and cortical (or compact) macrostructure [22], which differ in porosity, density and mechanical properties. Cortical bone accounts for the 80% of total bone mass, it is characterized by 5-10% porosity [23], [24] and density of 1.6-2.0 g/cm^3, and it is found in the diaphysis of long bone but also in the metaphyses and epiphyses, shielding the trabecular region [23], [25]–[27]. The main anisotropic mechanical properties of compact bone are listed in Table 1 [23].

	Longitudinal	**Transverse**
Elastic modulus (GPa)	18 ± 4	10 ± 2
Tensile yield stress (MPa)	72 ± 10	-
Tensile ultimate stress (MPa)	135 ± 16	53 ± 11
Compressive yield stress (MPa)	115 ± 16	42 ± 20
Compressive ultimate stress (MPa)	205 ± 17	131 ± 21

Table 1 Mechanical properties of cortical bone.

Conversely, trabecular bone represents the 20% of total bone mass, it has a density of 0.15-0.8 g/cm^3 and its highly porous structure (75-95%)

is well-interconnected forming a network [9], [24]–[27]. The mechanical properties of spongy bone strongly depend on porosity and can differ according to the anatomical position [25], but in general the elastic modulus is 0.1-2 GPa, the tensile strength is 1-20 MPa and the compression strength is 2-20 MPa [28]–[30].

Bone is continuously remodelling itself as a response to mechanical stimuli and biological signals [22]. Remodelling is a complex process and involves a dense communication among bone cells: osteocytes are mechanosensors and can induce osteoblasts and osteoclasts response by factors expression, osteoblasts are responsible for bone formation, whereas resorption is osteoclasts duty, and finally bone lining cells seem to combine resorption with formation [5], [9], [21], [22]. Cell crosstalk occurs through surface receptors and proteins in the extracellular matrix (ECM), an acellular dynamic three-dimensional structure found in the extracellular space and composed mainly of specific proteins and polysaccharides [6], [31]. At the nanoscale, the fundamental units of bone are hydroxyapatite nanocrystals (inorganic ECM) embedded into collagen triple helix (organic ECM) [6], [31]. Overall, bone is made of a mineralized inorganic component (65-70 wt%, mostly hydroxyapatite), an organic component (20-25 wt%, mostly collagen type I) and water (5-10 wt%). The mineralized part is mainly responsible for the rigidity, the compression resistance and the hardness, while the organic part confers elasticity and resistance to torsion to the bone structure [29].In particular, bone apatite is a highly substituted hydroxyapatite, where a large variety of ions (K^+, Na^+, Ag^+, Sr^{2+}, Mg^{2+}, Zn^{2+}, F^-, Cl^-, CO_3^{2-}, HPO_4^{2-}etc.) can be accommodated within its crystal structure [32]–[34]. The chemical structure of bone apatite is shown in Eq.1.1, but it is usually addressed as in Eq.1.2 only considering substitutions above 1 wt% [34].

$$Ca_{10-a}Mg_bNa_cK_d(PO_4)_{6-e}(CO_3)_f(OH)_{2-g}Cl_hF_i \tag{1.1}$$

$$Ca_{10-a}(PO_4)_{6-b}(CO_3)_c(OH)_{2-d} \tag{1.2}$$

In particular, bone apatite is usually defined as calcium-deficient and carbonated apatite with low crystalline tenor. The decrease in crystallinity is a feature directly related to the increase in ions substitution [33], [35]. The carbonate content in bone apatite ranges between 3-8 wt% [36]–[38] and, depending on the replacement site of carbonate group (CO_3^{2-}), two types of carbonated HAp can be distinguished; CO_3^{2-} partially substitute OH groups in A-type carbonate HAp, whereas it takes PO_4^{2-} place in B-type carbonate apatite . B-type is the carbonate apatite most commonly found in the bone mineral [37]. Because of substitution, bone apatite has a Ca/P molar ratio other than 1.67, the ratio of stoichiometric hydroxyapatite (HAp). The Ca/P ratio in bone tissue ranges from 1.5 to 2, depending on body location (i.e. enamel, dentin, bones) [39]. Consequently, bone apatite properties differ from synthetic HAp ones; for example, synthetic HAp is one of the least soluble calcium phosphate [40], whereas bone apatite is soluble in acidic media and this is why it can be resorbed by osteoclasts [39] and it has higher osteogenic capability [41]. It is also a current challenge to deal with consolidation and sintering of bonelike apatite due to its instability at high temperature [34].

1.1.2. Biomaterials for bone tissue engineering

From the material perspective, synthetic bone substitutes have been made of ceramics, metals, polymers and composites over the past years [24], [30], [42]–[45]. Each class of material meets some specific requirements of bone tissue but lacks on some other fundamental characteristics. Still the ‘chosen one’, the material 100% matching bone tissue, is an open challenge. In the current thesis work, a major attention will be given to ceramics and ceramic/polymer composites, being native bone tissue fundamentally made of such materials. The main requirements for bone substitutes are listed in Table 2. The ideal bone substitute should act as temporary structure (scaffold) in the bone defect, be able to stimulate cell activities (adhesion, proliferation, migration, etc) and extracellular matrix deposition leading to bone reconstruction. Ideally, the scaffold should resorb without causing any harm to the surrounding tissue environment, possibly with the same rate as fresh bone formation [46].

Moreover, it is desirable to also address the mechanical properties of bone tissue as well as the topographical and chemical surface characteristics (roughness, porosity and pore size) [9], [47]. An important point about mechanical properties is stress shielding, which occurs when the implanted scaffold has superior mechanical performance in comparison to bone tissue and it leads to bone resorption and loosening of the implant itself [1], [48].

Biocompatibility	The scaffold should "perform with an appropriate host response in a specific application" [43], [44], [49]
Osteoinduction	Ability to stimulate primitive, undifferentiated and pluripotent cells to bone cell phenotype [42], [50]
Osteoconduction	Ability to induce bone growth on the scaffold [42], [50]
Osteointegration	Development of a direct anchorage between the implant and the surrounding tissue without the presence of fibrous tissue at their interface [42], [50]
Bioactivity	Formation of a bonelike apatite layer on the surface of the scaffold [51], [52]
Resorbability	It should occur without producing harmful or toxic by-products, and the resorption rate should match the rate of new bone formation [29]
Porosity	Possibly interconnected with macropores(100-900 μm [9]) and micropores (<20 μm). The optimal range for bone in-growth is 200-350 μm [30].

Table 2 Main requirements for bone substitutes.

Among biomaterials, bioceramics have been deeply studied as bone substitutes [46], [48], [53]–[55] and traditionally they are classified in bioinert (alumina, zirconia, pyrolytic carbon, etc.), bioactive (bioglass, calcium phosphates, HAp, etc.) and biodegradable/bioresorbable (bioglass, tricalcium phosphates, calcium silicates, etc.) depending on their interaction with the host tissue .[46], [55]. Calcium phosphates will be discussed with more emphasis in the next section, dealing the present thesis work with calcium phosphates and calcium phosphate-based composites.

1.2. Calcium Phosphates

Calcium phosphates (CaPs) are naturally bioactive, most of them are also osteoconductive and osteoinductive and because of their similarity with natural bone mineral, they have been widely used in BTE in the form of scaffolds, granules, cements, coatings and nanoparticles [47], [56]–[59]. CaPs can be discriminated according to their Ca/P ratio, as shown in Table 3, the ratio influencing their properties, in particular solubility, chemical and thermal stability [40], [55]. The phase diagram in Figure 2 shows the range of stability of the main CaP phases [55]. Other factors influencing the biological response of CaPs are crystallinity, crystal size and morphology [60].

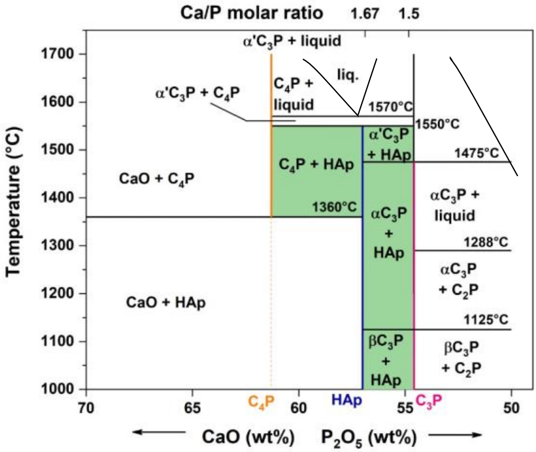

Figure 2 P_2O_5-CaO phase diagram with water partial pressure of 500 mmHg. C_2P=dicalcium phosphate; α α/β C_3P= α/β tricalcium phosphate; C_4P=tetracalcium phosphate. Adapted from Hench [55]

The main investigated CaP for skeletal tissue engineering are HAp, β-TCP, ACP and OCP [47], [58], [60], [61]. HAp is the CaP that mostly recalls bone apatite, but as previously mentioned, stoichiometric HAp has poor performances as bone substitute due to its high chemical stability, limited solubility in physiological conditions ($K_{sp} = 2.9 \cdot 10^{-58}$ in

Calcium phosphate	Chemical formula	Ca/P ratio
Monocalcium phosphate monohydrate (MCPD)	$Ca(H_2PO_4) \cdot 2H_2O$	0.5
Monocalcium phosphate (MCP)	$Ca(H_2PO_4)_2$	0.5
Dicalcium phosphate dihydrate (DCPD)	$CaHPO_4 \cdot 2H_2O$	1
Dicalcium phosphate (DCP)	$CaHPO_4$	1
Octacalcium phosphate (OCP)	$Ca_8H_2(PO_4)_6 \cdot 5H_2O$	1.33
α-Tricalcium phosphate (a-TCP)	$Ca_3(PO_4)_2$	1.5

β-Tricalcium phosphate (-TCP)	$Ca_3(PO_4)_2$	1.5
Amorphous calcium phosphate (ACP)	$Ca_3(PO_4)_2 \cdot nH_2O$	1.2-2.2
Hydroxyapatite (HAp)	$Ca_{10}(PO_4)_6(OH)2$	1.67
Oxyapatite (OXAp)	$Ca_{10}(PO_4)_6O$	1.67
Tetracalcium phosphate (TTCP)	$Ca_4O(PO_4)_2$	2

Table 3 Calcium phosphates, their chemical formula and Ca/P ratio.

a pH range of 3.5 to 9.7, at) [47], and poor osteoinduction. It is therefore an imperative to tune HAp properties to bonelike features by ions substitution [58]. Kheradmandfard et al. [62] demonstrated the improvement in bioactivity, cell proliferation and differentiation of a multiple ions substituted HAp in comparison to a reference synthetic HAp. Similarly, Ressler et al. [63] pointed out the proliferation and differentiation of human derived mesenchymal stem cells on multiple ion substituted HAp/chitosan composite.

In order to overcome the solubility issue of HAp, β-TCP was widely considered for resorbable scaffolds, being TCP more soluble than HAp ($K_{sp} = 10^{-28.9}$ at 25°C) [47], [59]. A combination of HAp and TCP (biphasic CaP, BCP) was also studied as an attempt to better control the degradation rate of scaffolds depending on the relative ratio of HAp and TCP [61], [64]. For example, Puttini et al. [65] showed promising results of BCP granules (60% HAp/40% β-TCP) inducing new bone formation in critical size defects in the calvaria of rats.

Other valuable alternatives stand in ACP and OCP, which were and still are a matter of an intense debate about being bone apatite precursors [66]–[69]. Posner et al. [70], [71] identified ACP as biological apatite transient phase, while according to Brown et al. [72], [73] bone apatite derives from OCP. OCP is more soluble at neutral pH than HAp ($K_{sp} = 10^{-96.6}$ at 25°C) but it is less stable in temperature due to dehydration, this strongly limiting the possible shaping processing routes [60]. In comparison to sintered synthetic HAp, OCP granules showed higher resorption and bone formation once implanted in a rabbit femur for 12 weeks [74].

On the other hand, ACP is more soluble at neutral pH ($K_{sp} = 10^{-25.7}$ at 25°C) [59] than OCP and bioresorbable. Due to its prompt transformation into low-crystalline apatite, ACP has been used widely as a bioactive material for coatings, cements and drug delivery [66]. The main limitation of ACP lies in its metastability which constrains possible thermal treatments as well as the material storage [66], [75].

1.2.1. Biogenic sources of calcium phosphate and biopolymers

As previously mentioned, the biological properties of CaPs are dramatically enhanced by ions substitution [62], [63]. A straightforward method to produce substituted CaPs is using biogenic precursors during synthesis [76]–[79], because such sources are naturally enriched with trace elements. Biogenic precursors are usually grouped according to their origin in marine, mammalian, shell and plant-derived [79], [80]. Figure 3 shows a scheme of biogenic sources classification.

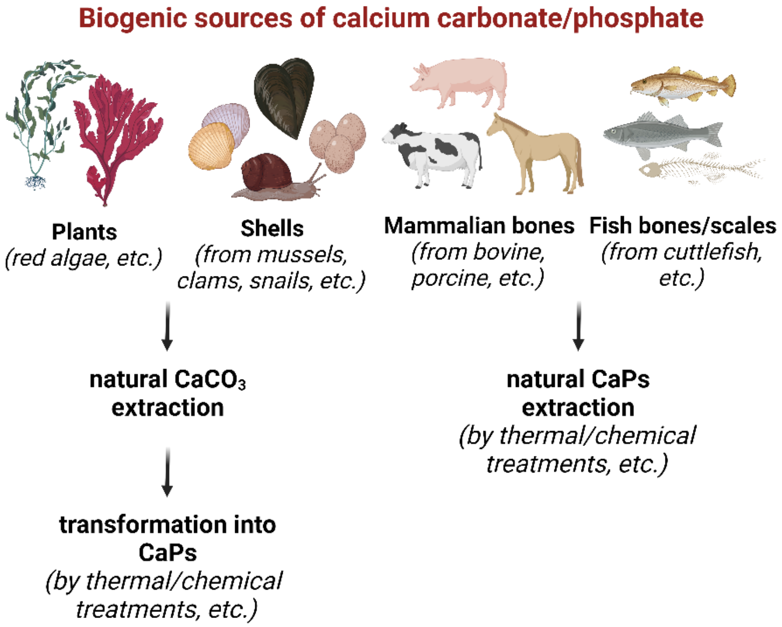

Figure 3 Example of biogenic sources of calcium carbonate and calcium phosphate.

Specifically, natural apatite can be directly found in marine by-products like fish bones and scales (i.e. cuttlefish, tuna, swordfish, etc.) [76], [81], [82], and in mammalian bones ((i.e. pigs, horses, bovines, etc.) [83],

[84], whereas shells from hens, snails, mussels, clams, shrimps, etc.) are mostly made of calcium carbonate in the form of vaterite, calcite and aragonite [85]–[87]. Such natural sources are usually considered as wastes, and discarded in landfills post-consumption causing pollution and ecosystem contamination [88]–[90]. The recovery of food industry wastes from landfills is thus beneficial from the environmental and economic point of view [88], [91]. Although the use of biowastes as raw materials within the biomedical field is still a niche [89], many literature works appeared on this topic in the past two decades [76], [79], [80], [84], [92]–[95]. Nonetheless, calcium phosphates produced from biogenic sources better mimic the natural bone tissue apatite, due to the presence of ions (K^+, Na^+, Mg^{2+}, Zn^{2+}, Sr^{2+}, Si^{4+}, F^-, CO_3^{2-}, etc.) as impurities and traces [32], [96]. Such ions are found in the calcium phosphate crystal lattice or as substitutes in the Ca, P and/or OH sites, and improve the biological properties of the bioceramic material [32], [96]–[98]. For example, Mg^{2+} enhances osteogenesis and angiogenesis, sustains bone cell adhesion, proliferation and differentiation [99]–[101]. Also Zn^{2+} positively affects adhesion and proliferation of human bone marrow mesenchymal stem cells but it also shows antibacterial properties, which are of relevant importance after implantation [99], [102]. Sr^{2+} plays an fundamental role in bone remodelling by promoting osteoblast bone formation and downregulating osteoclast bone resorption, and it stimulates mesenchymal stem cell osteogenic differentiation [103]–[105].

Moreover, biowastes can also provide organics and biomolecules [94], [106], [107]. Within the biomedical field, naturally-derived collagen, gelatin, alginate, hyaluronic acid and chitosan are of great interest because of their higher biocompatibility and biodegradability in comparison to synthetic polymers [107]–[109]. For example, alginate is extracted from brown seaweeds [110], while crustacean shells are a precious source of chitosan [111], [112]. Animal skin and bones can be exploited as collagen source [113], [114]. Also, gelatin is obtained from collagen denaturation, which can be carried out by acid (type A) or alkaline (type B) reaction. Gelatin from fish and porcine sources is type A, while bovine-derived gelatin is type B [115]. Finally, hyaluronic acid and fibrin can be extracted from fish eyeballs [107], [112]. In bone tissue engineering, biopolymers are often combined with calcium phosphates to form composite materials having superior mechanical and biological properties. Collagen has been extensively studied in the biomedical field, since it is the most abundant biopolymer in the natural bone tissue (20-25 wt%), providing toughness and playing a fundamental role in bone formation and remodelling [116], [117]. However, gelatine has been considered as an alternative due to the high costs associated with collagen [108]. Likewise collagen, gelatine supports cells adhesion and migration thank to the arginine–glycine–aspartic acid (RGD) motif [118].Hyaluronic acid, instead, plays an active role in angiogenesis, which is fundamental for bone formation, by supporting proliferation and migration of epithelial cells during vessel formation [119].

Among biogenic sources, mussel shells and chitosan are the only biowaste considered as raw materials in the present work.

1.2.1.1. Mussel shells

Mussel shells represent one of the most abundant food industry wastes, since mussels can be found worldwide in more than 12 different species. In 2020 the global marine and aquaculture production of molluscs was around 17.7 million tonnes, where mussels accounted for 1.1 million tonnes (6.2 %), according to the state of world fisheries and aquaculture report by the Food and Agriculture Organization of the United Nations (FAO) [120].

Mytili, mussels scientific name, are characterized by two shells kept together by an organic ligament, likewise all bivalve molluscs. Shells account for 75% total mussel weight, and they are mostly made of organics (≈ 1 -5 wt%) and calcium carbonate (≈ 95 -99 wt%), in the form of calcite (≈50-70 wt%) and aragonite (≈ 30-50 wt%) [121], [122]. Calcite is the stable polymorph in normal conditions, whereas aragonite is metastable and its stabilization depends on the Sr amount [123], [124]. In addition to Sr, elements like Mg, Na, K, Se and Si may be found in traces, according to the environmental condition mussels were subjected to [122], [125]–[129]. Seashells are a dynamic and evolving defensive system, since they grow as the mussel grows. The shell is formed by a series of deposited layers of mineralized material, resulting in a highly ordered structure [122], [127], [130]. There are three main layers: the periostracum, the prismatic layer and the nacre, as shown in Figure 4. The periostracum is the 40 µm thick outermost layer composed of proteins, polysaccharides and proteoglycans, and it acts as protective shield from chemical etching and abrasion [121], [131]. The intermediate layer is called prismatic, since its morphology characterized by calcite prisms growing orthogonally to the periostracum. Nacre, the innermost layer, instead consists of aragonite lamellae, responsible for the shiny appearance of the material [131].

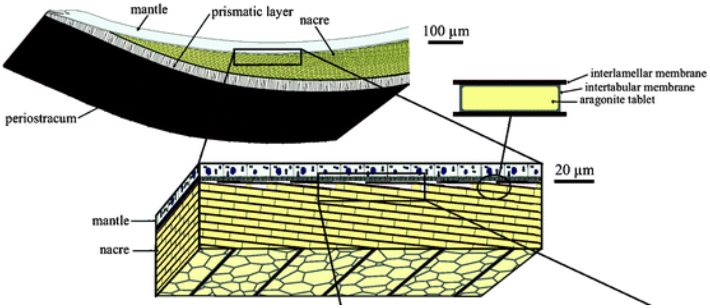

Figure 4 Mussel shell structure. Reproduced from Cartwright et al.[130].

Mussel shells was investigated as natural source of calcium carbonate for bone applications for the first time in 2010, when Jones et al. [132] transformed wasted shells from New Zealand into hydroxyapatite. In the majority of literature work, mussel shells are heat-treated at high temperature to get rid of the organics and/or to induce the carbonate calcination before proceeding with calcium phosphates synthesis [80], [96], [128], [132]–[135]. Up to date, few studies were carried out to evaluate the behaviour of mussel shell-derived calcium phosphates *in vitro*. El-Bassyouni et al. [136] reported the non-toxicity and proliferation of hydroxyapatite obtained from mussel shells to human mesenchymal stem cells and to epithelial cells. Also, the antibacterial properties of Ag-doped hydroxyapatite from mussel shells against *Escherichia coli* and *Staphylococcus aureus* were demonstrated by Agalya et al [137].

In the present work, mussel shells were directly used as raw materials without undergoing any thermal or chemical treatment before synthesis; Only the periostracum was manually grinded up to its complete removal.

1.2.1.2. Chitosan

Chitosan is a natural polysaccharide extracted from the exoskeleton of crustaceans (shrimps, lobster, crabs, etc.) and also from fungi cell walls [108]. It actually derives from deacetylation process of chitin, the most abundant polysaccharide found in nature after cellulose. Chitosan material properties strongly depend on the degree of deacetylation, which can vary from 56 to 99% [138]. Furthermore, the properties can be improved by functionalization through chemical treatments such as cross-linking, grafting, esterification, etherification, etc. Easy functionalization makes chitosan highly versatile and suitable for a wide range of applications, from the agricultural to the pharmaceutical and medical field. In particular, chitosan is bioactive, biodegradable, having not harmful by-products, biocompatible, non-toxic, hydrophilic (for a deacetylation degree above 85%), antifungal and antibacterial [139]. In addition, chitosan was found to stimulate good host response and to induce reconstruction and vascularization of damaged tissues [139], [140]. For these reasons, chitosan has been combined with calcium phosphates to improve the biological properties but also, the mechanical properties of the bioceramic. Guo et al. [141] produced a hybrid hydroxyapatite/chitosan nanostructure able to improve the poor fracture toughness of hydroxyapatite and the poor compressive and flexural strength of chitosan. The resulting porous composite showed mechanical properties similar to trabecular bone. Matinfar et al. [142] observed an increase in the compression strength and in adhesion, proliferation and mineralization of human osteosarcoma (MG63) cells, by increasing the amount of biphasic calcium phosphate fibres in a chitosan-based matrix.

Also in the present work, chitosan is combined with nano-hydroxyapatite to improve the mechanical and biological response of the material to better address the properties of natural bone tissue.

1.3. Low-temperature syntheses of hydroxyapatite

Traditionally, the synthesis routes to produce ceramic powders can be divided into mechanical and chemical methods [143]. Mechanical processes (like comminution and mechanochemistry) are simple and inexpensive methods, usually carried out at low temperatures. Their main disadvantages consist in limited purity and limited homogeneity [143], [144]. In contrast, chemical routes allow high purity of the produced powders, good control of final composition and particle size. The main limitations of chemical methods include possible agglomeration and medium/high costs [143], [144]. Some examples of chemical routes are decomposition, precipitation, sol-gel, spray drying [143].

In the next sections (1.3.1 and 1.3.2), mechanochemical and dissolution/precipitation synthesis are described in more details, since they were chosen as hydroxyapatite production routes in the present thesis work.

1.3.1. *Mechanochemical synthesis*

Mechanochemistry is a synthesis process where the energy for the chemical reaction to occur is provided by mechanical stresses (like compression, shear and friction) arising due to elastic and inelastic collisions between the reagents and the milling media [145], as schematically represented in Figure 5.

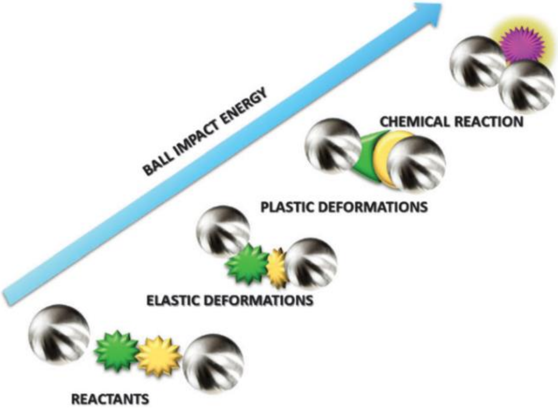

Figure 5 Schematic illustration of mechanochemical synthesis. Reproduced with permission from Xu et al. [145].

The synthesis usually takes place in a sealed container, with or without the addition of a liquid phase [146]–[150]. Dry milling often occurs discontinuously to avoid overheating due to intense friction [147], [148], [151] whereas in wet milling the liquid phase removes the generated heat and dramatically reduces the risk of overheating [152]. There are other fundamental process parameters affecting the synthesis outcome, namely rotational speed, milling time, milling ball material and diameter, ball-to-powder weight ratio and atmosphere [153], [154].

Mechanochemistry has been widely adopted for the synthesis of calcium phosphates, especially for hydroxyapatite [77], [78], [146]–[150], [155]–[157]. As for the synthesis of any other calcium phosphate, hydroxyapatite can be obtained by the reaction of a calcium source with a phosphorous source. In mechanochemistry, calcium source consists in carbonate ($CaCO_3$) [78], [147], oxide (CaO) [77], [146] or $CaOH_2$ [148], [153], while phosphorous is introduced in the form of phosphoric acid (H_3PO_4) [149], [155], anhydrous calcium hydrogen phosphate ($CaHPO_4$)

[146], [157], dicalcium phosphate dihydrous ($CaHPO_4 \cdot 2H_2O$) [147], [149], phosphorous pentoxide (P_2O_5) [153], calcium pyrophosphate ($Ca_2P_2O_7$) [150] or calcium phosphate monobasic monohydrate ($Ca(H_2PO_4)_2 \cdot H_2O$) [156].

Mechanosynthesis allows to produce nanocrystalline hydroxyapatite in a simple and straightforward way; it does not require any complex and expensive equipment, since it can be carried out in a ball mill. Also, the process can be implemented in industry by scaling-up the milling reactor/jar. Although the majority of solid-state synthesis where high temperature is required for the reaction to occur [158], mechanochemistry can be performed at room temperature [78], [152], [158]. However, some literature studies report additional high-temperature treatments carried out to produce highly pure hydroxyapatite powder [77], [149], [150], [154], [155]. The main limitations of mechanosynthesis consist in possible long processing time (>24 h [146], [154]), unreacted reagents due to uneven mixing, by-products and contaminations from jar and milling media [147], [153], and lower control over the reaction in comparison to other methods such as precipitation and hydrothermal [159].

In Chapter II, mussel shells-derived calcium carbonate is mixed with a phosphoric acid solution to produce nanocrystalline hydroxyapatite by mechanochemical synthesis at room temperature.

1.3.2. Dissolution-precipitation synthesis

Dissolution-precipitation synthesis is a chemical method to produce ceramic powders [143], [144]. As the name suggests, the process is articulated in two steps: complete dissolution of the precursors and precipitation of the desired composition. The main process parameters include pH of the solution, temperature, stirring speed and time, as shown in Figure 6.

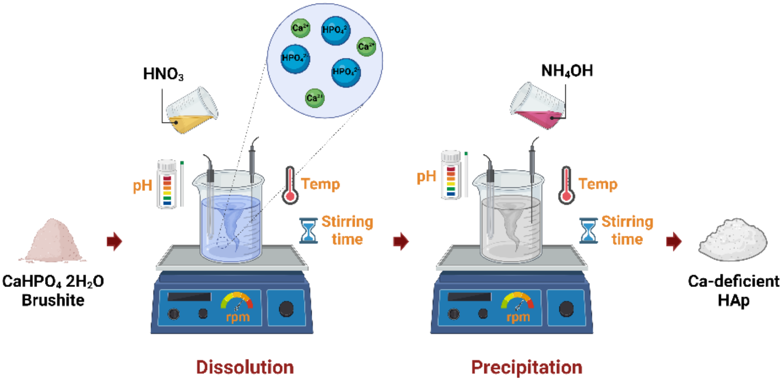

Figure 6 Dissolution-precipitation synthesis of calcium-deficient hydroxyapatite starting from brushite.

Relatively to calcium phosphates, Lakrat et al. [160] produced a calcium deficient-hydroxyapatite by dissolving brushite in a 1M nitric acid solution to obtain a crystal-clear solution, according to Eq.1.3. Precipitation was then induced by the rapid addition of ammonia solution to reach pH 8, as shown in Eq.1.4.

$$CaHPO_4 \cdot 2H_2O \xrightarrow{HNO_3} Ca^{2+} + HPO_4{}^{2-} + 2H_2O \tag{1.3}$$

$$Ca^{2+} + HPO_4{}^{2-} \xrightarrow{NH_4OH} Ca_{10-x}(PO_4)_{6-x}(HPO_4)_x(OH)_{2-x} \tag{1.4}$$

Similarly, eggshell-derived hydroxyapatite was obtained by eggshell vaterite mixed with diammonium phosphate solution under continuous stirring (300 rpm) at 160°C and controlled pH 10 for 2 h [161], while Benataya et al. [162] synthesised a B-type carbonated apatite starting from hydroxyapatite and sodium carbonate. Besides, dissolution-precipitation allows to produce an ion-substituted nanocrystalline apatite with low crystalline tenor [34] likewise bone apatite. For example, the production of Mg, Cu, Ag, and Sr-doped hydroxyapatite was easily implemented by adding the ion precursors ($MgCl_2$, $CuCl_2$, $AgNO_3$ and $SrCl_2$, respectively) during the dissolution step [160]. Such versatility during the process is a key advantage of this production route, as it can lead to new scenarios in the synthesis of advanced ceramic materials. Overall, dissolution-precipitation is a time and cost-effective synthesis method, and ensures good repeatability, high control over the reaction, and crystallinity control [163]. It is also suitable for ceramic/polymer composite production, allowing homogeneous distribution of the two phases [34].

In Chapter III, dissolution-precipitation synthesis is investigated to produce nanocrystalline hydroxyapatite and hydroxyapatite/chitosan powders by using mussel shells as calcium precursor. Finally, the synthesis route was implemented to obtain a homogeneous drug-loaded hydroxyapatite/chitosan powder in one-process.

1.4. Cold sintering

Sintering is one of the most ancient processes known to the mankind, where ceramic powders join together by atomic diffusion without reaching the melting point ($T_{sintering} \approx 0.5\text{-}0.75\ T_{melting}$) [143], [144], [164]. Sintering is driven by the reduction in the total free energy of the ceramic system through two concurrent phenomena, densification and coarsening, and it results in the evolution of mass and porosity [143], [144], [164]. A variety of sintering techniques has been developed in the past [165], where different sintering aids were introduced such as pressure (hot pressing, hot isostatic pressing, etc.), liquid-phase (liquid-phase sintering, viscous sintering, etc.) and alternative heating sources, like electric field-assisted techniques [166]–[169]. Also, innovative sintering techniques arose by a combination of aforementioned sintering aids in order to strongly reduce the firing temperature, the processing time and consequently the costs, to control the final composition and microstructure, and to trigger the required material properties [165]–[168], [170].

Part of the novelty of this thesis work lies in consolidating a ceramic material at a temperature not superior to 350°C. The dramatic reduction of temperature is counterbalanced by the simultaneous application of an external uniaxial pressure, that can reach several hundreds of megapascal. In addition, such sintering process is usually carried out after mixing the ceramic powder with a transient liquid phase having an evaporation temperature lower than the sintering temperature. A scheme of the process is reported in Figure 7.

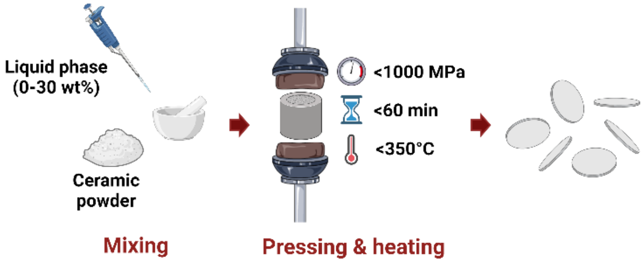

Figure 7 Cold sintering process scheme.

The so-called cold sintering process (CSP) was developed for the first time in 2016 at by Prof. Randall and his research team of the Pennsylvania State University [171]–[174] , but already in the 1980s Gutmanas et al. [175], [176] introduced the cold sintering concept, when consolidating metallic powders at room temperature under 4-10 GPa in a lubricated die. Due to the external pressure and low temperature applied and the presence of a liquid phase, the mechanism leading to densification during cold sintering is most likely a combination of plastic deformation and pressure-solution creep, articulated in dissolution, diffusion and precipitation [177]–[179]. In short time, cold sintering has become a relevant research topic, appearing in more than 350 literature works since 2016 [167], [180]–[183] according to Scopus.

The majority of such works is related to electrical and dielectric ceramic materials finding applications as piezoelectrics [184]–[187], microwave dielectrics [172], [188]–[193], semiconductors [194], [195], solid-sate batteries [196], capacitors [197], and patch antennas [198], [199]. One of the reasons of such wide interest from the scientific community is for the sake of developing environmentally-friendly processes able to reduce the energy consumption during manufacturing. Cold sintering can be considered a promising candidate as a green and sustainable process in comparison to other consolidation methods (such as pressure-less solid-state sintering, hot-isostatic pressing, liquid-phase sintering, hot pressing, etc.) [200], [201], especially in terms of energy consumption and energy saving potential [200]–[203]. CSP is also competitive in the processing time (usually from few min to 1 h) [204], as shown in Figure 8b, in the simple required equipment, and therefore, in the overall costs associated with the process itself [203]. In agreement, techno-economic assessments conducted by Ibn-Mohammed et al. [200] and by Jayasayee et al. [201] demonstrate that CSP is highly cost-effective due to the lower capital costs, best return on investment and good limitation of CO_2 footprint even in a mass production perspective.

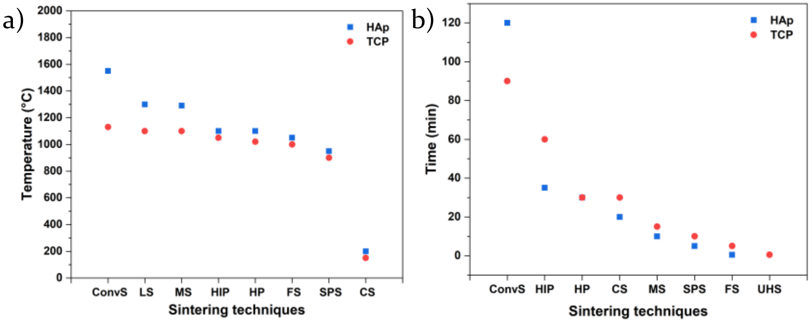

*Figure 8 Sintering temperature and time of several sintering techniques (Abbr.: **ConvS** = conventional sintering, **LS** = laser sintering, **MS** = microwave sintering, **HIP** = hot isostatic pressing, **HP** = hot pressing, **FS** = flash sintering, **SPS** = spark plasma sintering, **UHS** = ultrafast high-temperature sintering, **CS** = cold sintering. Adapted from Indurkar et al. [204].*

Besides the advantages in terms of energy and cost savings, the drastic decrease in sintering temperatures strongly limits the possibility of phase transformation and grain growth. Grain growth during CSP has been reported in few works [172], [205]–[208]. However, grain coarsening seems attributable to prolonged holding time and, mostly, to the transient liquid phase [209]. In this scenario, grain growth can be considered as a chemical effect because the added liquid phase can change the chemistry of the system at the grain boundaries, enhancing grain coarsening rather than grain boundary diffusion [210], [211]. In agreement, Bang et al. [212] believe that the sintering kinetics during CSP is controlled by a "compatible transient chemistry".

Moreover, cold sintering opens to new frontiers in the consolidation of metastable systems [213], temperature-sensitive materials [214]and ceramic/polymer composites in one-step [171], [182]. Typically, the polymer content ranges from 2 to 30 vol%, although the optimal range is 5 to 15 vol% because the organic improves the material properties without impeding densification or forming pores [186], [215], [216]. Currently, there are two pathways for the cold sintering of hybrid ceramic/polymer composites [217]: direct mixing and dissolution method, as shown in Figure 9 and Figure 10. Composite materials prepared by dissolution method show better homogeneity in comparison to direct mixing preparation [217].

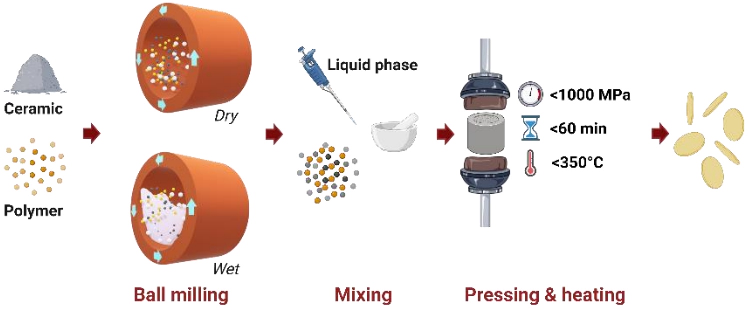

Figure 9 Cold sintering of ceramic/polymer composites by direct mixing.

Very recently, Guo et al. [218] successfully produced a hydroxyapatite/chitosan composite material by cold sintering.

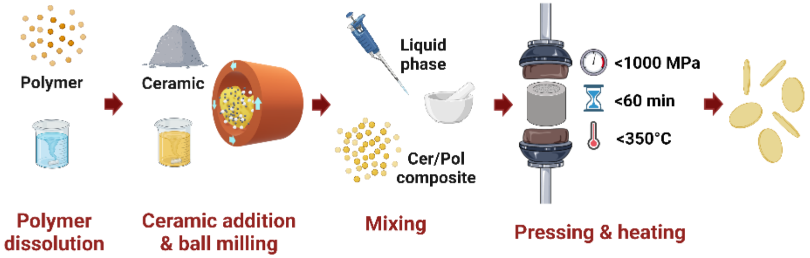

Figure 10 Cold sintering of ceramic/polymer composites by dissolution method.

According to the dissolution method, chitosan was primary dissolved in an acetic acid solution, where the co-precipitation of chitosan and hydroxyapatite was induced by the addition of $Ca(NO_3)_2 \cdot 4H_2O$ and $(NH_4)_2HPO_4$. Similarly, Hu et al. [219] prepared an hydroxyapatite/polylactic acid (HA/PLA) composite by dissolution method and cold sintering. Moreover, they add doxorubicin (DOX) drug by direct mixing prior to perform cold sintering. These two recent studies are a clear example of the new frontiers cold sintering open in the biomedical field. Bioceramics, in fact, are usually sintered at around 1000°C [204], [220], as shown in Figure 8a. Such temperatures make impossible the production of ceramic-based composite and the drug-loading in one-step. Additionally, bioceramics (i.e. calcium phosphates) can easily undergo phase transformation during heat treatment [220], whereas Hassan et al. [221]–[223] and Shen et al. [224], [225] consolidated hydroxyapatite synthesised by co-precipitation up to 90-95% relative density by cold sintering at a maximum temperature of 300°C without any phase transformation or grain growth.

In the past, Drouet et al. [226] also explored the consolidation of calcium phosphates (i.e. DCPD, OCP, amorphous TCP and nanocrystalline apatite) at low temperature (120°C-200°C) by spark plasma sintering (SPS) where the bioceramic powder was inserted into a graphite die covered with a graphite foil, and pressed and simultaneously heated up by Joule effect due to the application of a pulsed direct electrical current [227], [228]. The SPS process is carried out in a protective and controlled atmosphere, usually under vacuum or protective gas (i.e. argon) purged inside the sintering chamber [227],

[229]. Drouet et al. [226] were able to sinter stoichiometric HAp up to 80% relative density by SPS only at 950°C under 50 MPa, whereas they succeeded to consolidate non-stoichiometric nanocrystalline apatite up to 60-70% at much lower temperature (200°C) under the same applied pressure of 50 MPa and no phase transformation of non-stoichiometric apatite was found despite its metastability. In addition, the resulting spark-plasma sintered apatite components showed a tensile strength of 18-25 MPa, comparable with spongy bone rather than compact bone [28]–[30]. Similarly, Ortali et al. [230] carried out SPS on carbonated and non-carbonated biomimetic apatite and amorphous calcium phosphate at 150°C and 80 MPa and reported a maximum density of ~80 % for non-carbonated ACP and apatite, whereas carbonated apatite and ACP could not be consolidated above ~60 %. The authors hypothesised that carbonates could negatively affect the material densification, as also confirmed by Luigina et al. [231]. In light of the dramatic reduction of temperature for nanocrystalline apatite sintering, Brouillet et al. [232] carried out the one-step sintering of apatite/cellulose composites by SPS and achieved a relative density of 75% carrying out the process at 150°C and 100 MPa in 20 min. The densification mechanism behind the consolidation of non-stoichiometric apatite at a maximum temperature of 200°C are still not fully understood. Ortali et al. [230], [233] and Drouet et al. [226] proposed 'crystal fusion' as the main consolidation pathway due to the pressure and low temperature applied during the SPS process. Accordingly, crystal-crystal interactions during crystal fusion imply the migration of species when the system is subjected to an applied pressure combined with an electrical current and in the presence of hydrated amorphous solid medium, like a surface hydrated layer typically surrounding nanocrystalline bone like apatite and amorphous calcium phosphate particles [230], [231], [234]. Therefore, low temperature densification can occur only if the surface hydrated layer is preserved during the process. Moreover, the surface hydrated layer is also responsible for nano-apatite surface reactivity, fundamental for its bioactivity and biological properties in view of bone tissue engineering applications [234].

Interestingly, Egli et al. [235] and Al-Maawi et al. [236] observed a change in the surface chemical reactivity of calcium phosphates (i.e. α/β-tricalcium phosphates) heat treated above 450°C, due to the formation of a thin alkaline layer. As a consequence, the resorption activity of osteoclasts seeded on heat-treated substrates was downregulated in comparison to osteoclasts seeded on not-treated samples [235], [236]. Also, hydroxyapatite osteoconductivity was found to decrease by increasing the sintering temperature [34].

Bone cell biological response on cold-sintered calcium phosphates is still a matter of investigation, and it would be of great interest to understand how cells behaviour is affected by cold-sintered substrates.

In the current work, hydroxyapatite is consolidated by cold sintering at a maximum temperature of 200°C with and without the presence of a liquid phase. The pressure applied ranged from 300 to 1000 MPa, while the holding time varied from 10 to 30 min. Nonetheless, hydroxyapatite/chitosan and drug-loaded hydroxyapatite/chitosan composites were sintered at room temperature.

Aim of the work

The aim of the present thesis work was to transform discarded mussel shells into nanocrystalline multi-ion substituted hydroxyapatite by mechanochemical and dissolution-precipitation synthesis at a processing temperature not exceeding 45°C. To further mimic bone tissue composition, also hydroxyapatite/chitosan composite were produced. Synthesised powders were then consolidated by cold sintering at a maximum temperature of 200°C. The sintered body were further mechanically and biologically investigated as possible scaffolds or coatings for bone tissue engineering applications.

Chapter II Mechanochemical synthesis of hydroxyapatite from discarded mussel shells

2.1. Introduction

In the present chapter, mussel shells are introduced as raw materials for the low temperature synthesis of nanocrystalline hydroxyapatite by mechanochemical process, followed by a drying step at a maximum temperature of 150°C. Both mussel shells and synthesised powder underwent physicochemical characterization.

Some of the results reported in the chapter are already published in [237], [238].

2.2. Materials and methods

Discarded mussel shells, mostly of *Mytilus Galloprovincialis* species, were collected in a local restaurant in Trento (Italy) after consumption. Shells were cleaned under tap water to get rid of algae and meat residuals, manually polished to remove the dark *periostracum* layer, boiled for 10 min and then put in a Preciterm® oven at 80°C until complete drying. Once dried, shells were ball-milled for 5 min at 50 Hz rotation frequency in a porcelain jar using porcelain balls (Ø= 18 mm) in a 10:1 ball-to-shell ratio. Crushed seashells were sieved with a 300 µm mesh, and introduced in the synthesis of hydroxyapatite as a calcium source, without any calcination process.

2.2.1. Mechanochemical synthesis

The mechano-chemical synthesis was carried out by mixing shell powder with 1M phosphoric acid solution (85% pure H_3PO_4, CAS 7664-38-2, Sigma-Aldrich®). The reagents calcium and phosphorous sources were mixed in a polyethylene bottle to have a Ca/P molar ratio of 1.67, corresponding to the stoichiometry hydroxyapatite. The mechanosynthesis was performed with a high-energy 3D shaker mixer T2F TURBULA® (by WAB©) at room temperature for a mixing time of 30 min to 4 h, with the aid of zirconia balls (Ø= 6 mm) as milling media in a 5:1 ball-to-powder ratio. The resulting ceramic slurry was poured

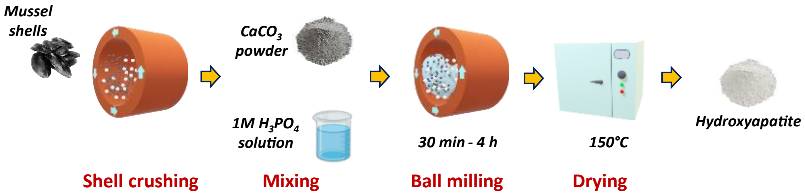

Figure 11 Mechanochemical synthesis scheme.

into a petri dish and dried overnight in a Preciterm® oven at 150°C. A scheme of the performed mechanosynthesis is shown in Figure 11.

2.2.2. Characterization of synthesised powder

The crystalline phases in the raw mussel shells and synthesised powders were determined by X-ray diffraction (XRD) using an Italstructures IPD 3000 diffractometer equipped with a Co-Kα (λ= 1.789 Å) source and a Inel CPS120 detector. The collected XRD patterns were analysed with MAUD® software, based on Rietveld refinement method, while the reference phases for the analysis were collected from Crystallography Open Database (COD) and RRUFF™ database. The Ca/P molar ratio and the elemental analysis was carried out by Inductively Coupled Plasma - Optical Emission Spectrometry (ICP-EOS) using a Spectro Ciros Vision CDD equipment by Spectro Analytical Instruments GmbH & Co. About 30 mg of crushed shells and synthesised powder were dissolved in a 100ml flask by adding 10 ml of 5% ultra-pure nitric acid water solution (70 vol% HNO_3, CAS 7697-37-2, Sigma Aldrich) and pure water obtained by reverse osmosis (conductivity< 0.1 µS). Before the analysis, 1 ml of the prepared solution is poured into a 25 ml flask where 0.25 ml of ultra-pure nitric acid is added as well as pure water to complete volume. A pure hydroxyapatite (> 99.995 % trace metal basis, CAS 12167-74-7, Sigma–Aldrich) was used as a reference standard for Ca and P, while other possible elements were determined with a multi-element standard solution (type IV, Merck KGaA). The materials were also investigated by Fourier transformed infrared spectroscopy (FTIR) to determine the molecular structure and functional groups. The spectra were collected with a Nicolet Avatar 330 FTIR spectrometer, in transmission mode (64 scans) from 4000 cm^{-1} to 400 cm^{-1} with a spectral resolution of 2 cm^{-1}. Few micrograms of powders were mixed with potassium bromide (KBr), and then pressed to produce a pellet in a cylindrical die (Ø = 13 mm, by Specac. The thermal behaviour of the materials was studied by thermogravimetric and differential thermal analyses (TGA-DTA) using a NETZSCH Geraetebau GmbH STA 409 thermobalance. The analysis was performed at 10°C/min in air and nitrogen flow (100 ml min^{-1}), up to 1400°C. Finally, the shell structure and the powder morphology were assessed by field-emission scanning electron microscopy using a SUPRA 40 FESEM microscope by Carl Zeiss Microscopy GmbH. The samples were coated with a Pt/Pd thin layer just before the analysis.

2.3. Results and discussion

Mussel shells are mainly made of calcium carbonate ($CaCO_3$), in the form of calcite and aragonite, as shown in the XRD pattern in Figure 12.

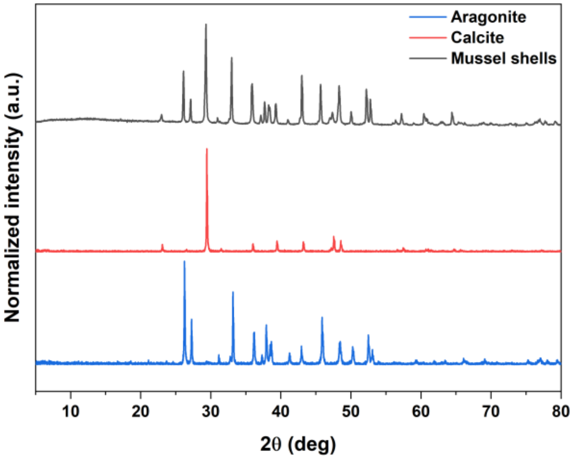

Figure 12 XRD patterns of mussel shells (grey), calcite (red) and aragonite (blue). The reference pattern of aragonite (No. R040078) and calcite (No. R050307) were collected from RRUFF™ database.

In particular, shells consist of 50 wt% aragonite and 50 wt% calcite, according to the semiquantitative analysis carried out with MAUD® software.

The presence of aragonite and calcite was further confirmed by FTIR spectroscopy, as shown in Figure 13. The signals at 1791 cm^{-1} (ν_3-CO_3),

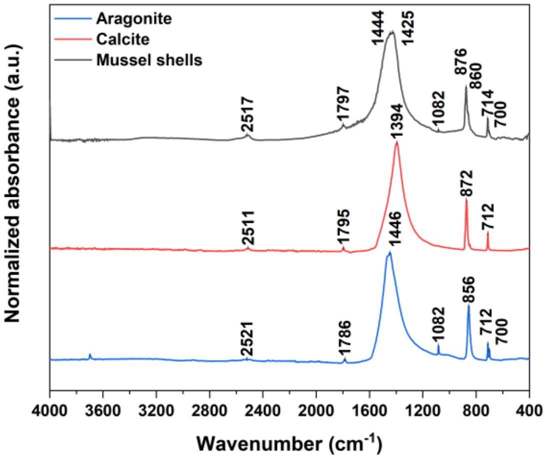

Figure 13 FTIR spectra of mussel shells(grey), calcite (red) and aragonite (blue). The reference spectra of aragonite (No. R040078) and calcite (No. R050307) were collected from RRUFF™ database.

1425 cm^{-1} (ν_3-CO_3) and 876 cm^{-1} (ν_2-CO_3) are typical of calcite, whereas the bands at 1082 cm^{-1} (ν_1-CO_3), 852 cm^{-1} (ν_2-CO_3), 1444 cm^{-1} (ν_3-CO_3) and 704 cm^{-1} (ν_4-CO_3) were attributed to aragonite. The ν_4-CO_3 peak at 714 cm^{-1} was associated to both $CaCO_3$ polymorphs, as well as the ν_1/ ν_3-

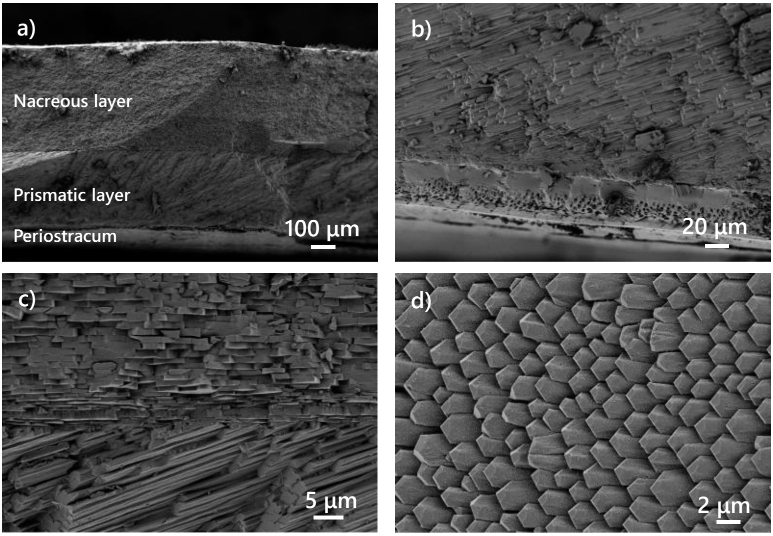

Figure 14 FESEM images of (a) mussel shell cross-section, (b) interface between periostracum and prismatic layer, (c) interface between prismatic and nacreous layer and (d) top view of aragonite platelets.

CO_3 band at 2517 cm^{-1}. In addition to calcium (40.08 ± 0.35 wt%), shells also contained traces of Na (0.30 ± 0.15 wt%), Sr (0.07 ± 0.01 wt%), Mg (0.08 ± 0.02 wt%) and K (0.03 ± 0.02 wt%).

The cross-section of the shell is characterized by a layered structure, as shown in Figure 14a. The periostracum is very thin (~30 μm) and shields the mineralized layers from chemical and mechanical attacks, such as erosion, abrasion, etching, etc. Right underneath the periostracum, calcite aligned parallel prisms form the prismatic layer (~300 μm thick), as shown in Figure 14b. Finally, the innermost part, also known as nacre, consists in rows of lamellae formed by hexagonal aragonite platelets and it results in ~400 μm of thickness (Figure 14c). The aragonite platelets are responsible for the iridescence of nacre, because their size is comparable with the light wavelength, as can be observed from the top view in Figure 14d. The thermal evolution of the biogenic $CaCO3$ in air and nitrogen flow is shown in Figure 15. The total weight loss was ~46%, independently from the flux fluid, and it was associated with organic mass degradation (5 wt% up to 600°C) and calcination (41 wt% above 600°C). In agreement, calcination phenomenon corresponds to an endothermic peak in the DTA curve [239]. The exothermic signals at 380°C and 500°C were instead attributed to organic loss and phase

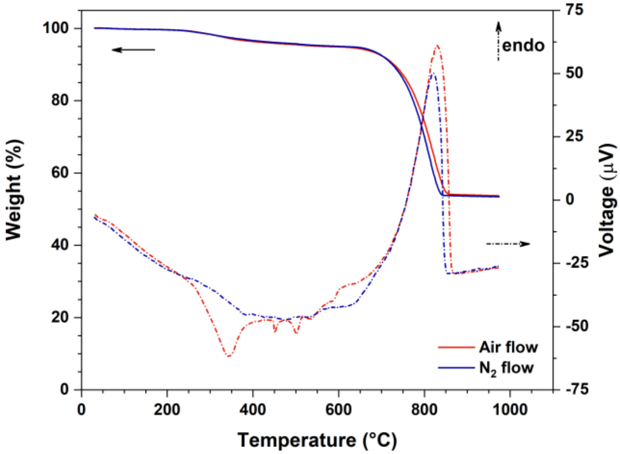

Figure 15 TGA and DTA curves of mussel shells in air (red) and N2 (blue) flow.

transformation of aragonite to calcite [239], as demonstrated by the XRD patterns in Figure 16.

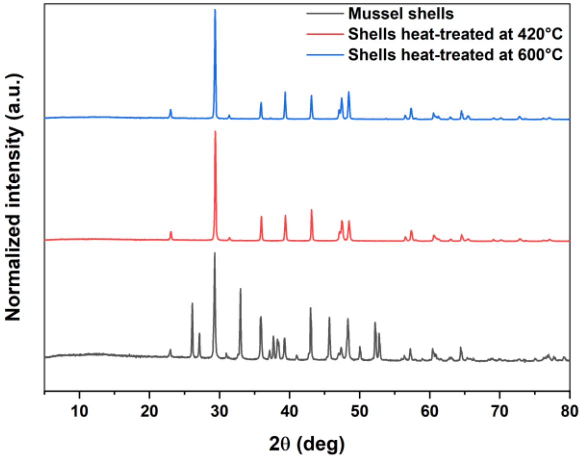

Figure 16 XRD of mussel shells before (grey) and after the heat treatment at 420°C (red) and 600°C (blue).

As previously mentioned, shells were the calcium source to produced hydroxyapatite by mechanochemical synthesis. The XRD patterns of

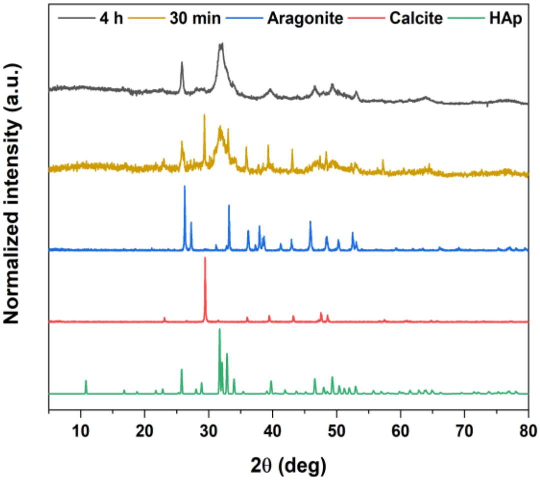

Figure 17 XRD patterns of powder produced after 4h (grey) and 30 min (yellow) of mechanosynthesis, and reference patterns of aragonite in blue (No. R040078), calcite in red (No. R050307) and HAp in green (No. R130713) collected from RRUFF™ database.

the materials obtained after 30 min and 4 h of synthesis are shown in Figure 17. The transformation into hydroxyapatite is still not complete after 30 min of mixing, since calcium carbonate is still identified in the XRD pattern. Conversely, pure hydroxyapatite was obtained with a longer mixing time. Therefore, 4 h was set a processing time for the mechanosynthesis of HAp from mussel shells. In comparison to the reference pattern, the synthesised HAp is characterized by broader diffraction peaks, which are a feature of nanocrystalline materials.

In agreement, the FESEM images in Figure 18 show the nanometric flakes of the produced hydroxyapatite. The flakes are few nm thick and about 100 nm wide; the average crystallite size determined by MAUD software is 26 nm.

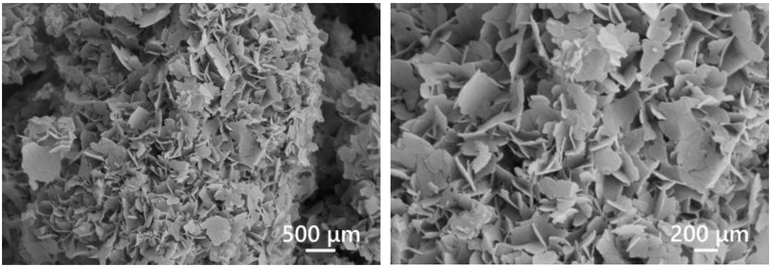

Figure 18 FESEM micrographs of as-synthesised HAp by mechanosynthesis.

The as-synthesised HAp was further analysed by FTIR (Figure 19). Typical vibrational bands of HAp were identified, like the OH signal at 3728 cm^{-1}, the water molecule bands at 3440 cm^{-1} and 1635 cm^{-1}, the antisymmetric stretching ν_3-PO_4^{3-} at 1032 cm^{-1} and 1117 cm^{-1}, the antisymmetric bending at ν_4-PO_4^{3-} at 602 cm^{-1} and 563 cm^{-1}, the symmetric stretching ν_1-PO_4^{3-} at 960 cm^{-1} and bending at ν_2-PO_4^{3-} 471 cm^{-1}. In addition, carbonate signals were found at 1547 cm^{-1}, 1454 cm^{-1}, 1417 cm^{-1} and 874 cm^{-1}, revealing that the produced HAp is carbonated as natural bone apatite. Carbonate groups (CO_3^{2-}) can partially substitute OH^- ions (A-type HAp) or PO_4^{3-} (B-type HAp). In particular, the peak 1547 cm^{-1} is a ν_3-CO_3^{2-} attributed to A-type carbonated HAp, whereas the other carbonate bands are characteristic of B-type with the exception of the signal at 1454 cm^{-1} which is common of both types [37],

[162], [240]. Finally, the band at 1385 cm^{-1} is a result of CH_3 vibration and can be associated to the organic matter of mussel shells.

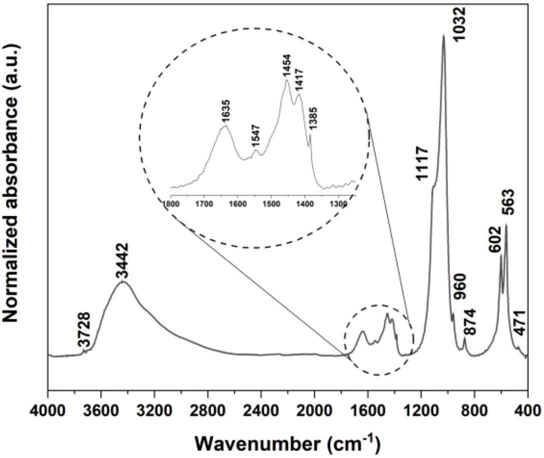

Figure 19 FTIR of HAp produced by mechanochemical synthesis.

Likewise for the raw mussel shells, the synthesised HAp is characterized by traces of Na (0.34 ± 0.03 wt%), K (0.03 ± 0.02 wt%), Sr (0.07 ± 0.01 wt%) and Mg (0.07 ± 0.02 wt%). Ionic substitution is a fundamental feature of bone apatite, and makes HAp more soluble and less thermal resistant [32]. Metallic ions (i.e Mg and Sr) found in bone apatite positively affect bone formation and remodelling [241]–[243]. Besides, the Ca/P molar ratio was found to be 1.73 ± 0.01, slightly higher than the stoichiometric value (1.67) but consistent with a ionic substituted HAp [32], [37]. The thermal behaviour of as-synthesised HAp is reported in Figure 20. The material experienced three weight losses: an initial weight loss of 2.5 wt% at 95°C, due to the evaporation of adsorbed water, another loss of 4.5 wt% between 300 and 500°C due to the evolution of residual organic matter and of carbonates [37], [162], and, finally, the OH removal (dehydroxyalation) due to the phase transformation of HAp into tricalcium phosphate (-1.5 wt%) [37]. The DTA curve also presents four exothermic events which can be addressed to the adsorbed water release (T≈95°C), the removal of organics (T≈345°C), carbonates (T≈460°C) and dihydroxylation

(T≈705°C), respectively The thermal behaviour of the produced HAp is consistent with other biogenic apatite investigated in the literature [244], [245].

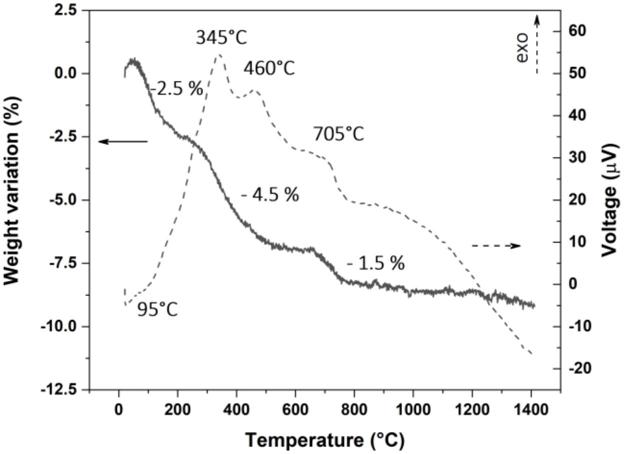

Figure 20 TGA-DTA curves of HAp produced by mechanochemical synthesis.

2.4. Conclusions

Discarded mussel shells are a precious source of calcium carbonate (95% pure), which should be valorised rather than being disposed of in landfills. In the present chapter, crushed mussel shells were transformed into pure hydroxyapatite by mechanochemical synthesis at room temperature for 4 h. The as-synthesised hydroxyapatite was proved to be nanocrystalline, non-stoichiometric and ionic substituted, all features typical of bone apatite.

Chapter III Dissolution-precipitation synthesis of hydroxyapatite/chitosan composites from food industry waste

3.1. Introduction

The dissolution-precipitation synthesis of HAp and HAp/chitosan composites is discussed in the current chapter. Also in this case, synthesis was carried out by exploiting mussel shells as natural calcium carbonate source, while chitosan was obtained by shrimp exoskeleton. Chitosan was introduced as reinforcement for the mechanical properties of HAp but also to improve the biological response of the material. Nonetheless, dissolution-precipitation was further implemented to produce a drug-loaded HAp/chitosan powder, where Sr ranelate (SrRAN) was chosen as active principle to further stimulate bone tissue reconstruction.

The work presented in this chapter was carried out during the visiting period abroad at the Baltic Biomaterial Centre of Excellence of Riga Technical University (Latvia, LV) under the supervision of Prof. Janis Locs, and at the National Polytechnic Institute of Toulouse (France, FR) in collaboration with Prof. Christele Combes.

Part of the chapter content has been published in [246].

3.1.1. Strontium Ranelate

Among other drugs, SrRAN ($C_{12}H_6N_2O_8SSr_2$) has been used to inhibit bone loss and to reduce fractures risk, especially in pathological conditions such as osteoporosis and osteoarthritis [247]–[250]. In particular, SrRAN plays duplex action on bone remodelling: it reduces the resorption activity of osteoclasts and simultaneously, it stimulates bone formation by osteoblasts. As consequences, bone mass increases, as well as bone mineral density. It was also demonstrate an improvement of mechanical strength, stiffness and hardness of cortical bone, due to the positive effect of SrRAN on bone microarchitecture [249]. However, the specific mechanisms of action of Sr at the cellular and molecular level are not discussed in this work (the review by Pilmane et al [251] reported an exhaustive and detailed description of the topic). Although SrRAN therapy has been tested *in vitro* and *in vivo*, both with animal models and humans (on male and female population), some safety concerns have been debated in the past years. The main issues involve the increment of cardiovascular diseases (i.e. coronary heart disease, cerebrovascular disease or peripheral atherosclerosis) associated with SrRAN administration and therefore, SrRAN is forbidden for patients showing hypertension, angina, cerebrovascular disease, ischemic heart disease and peripherical arterial disease [249], [251]. Moreover, SrRAN is nowadays considered as second order treatment for osteoporosis to be followed when other osteoporotic therapies are inefficient and only when contraindications are almost null [251]. New strategies in SrRAN therapy include the development of controlled local delivery systems [252]–[254], to avoid SrRAN side effects reported with systemic administration.

3.2. Materials and methods

Dissolution-precipitation synthesis was carried out by using crushed mussel shells (<350 μm), hydrochloric acid (HCl fuming 37%, for analysis, CAS 7647-01-0), sodium hydroxide (NaOH pellets for analysis, CAS 1310-73-2), phosphoric acid (H_3PO_4 75%, CAS 7664-38-2) and chitosan from shrimp shells (low-viscous, CAS 9012-76-4). All reagents and chitosan powder were purchased from Merck KGaA (Darmstadt – DE).

3.2.1. Dissolution-precipitation synthesis

10 g of crushed mussel shells were poured into 600 ml of distilled water and mixed with a Biosan MM-1000 overhead stirrer at 350 rpm. The system was constantly kept at 25°C with a Biosan MSH-300i hot plate while the pH was continuously monitored with a WTW inoLab pH 7110 digital pH-meter. When the pH of the suspension stabilized at 9.7-9.8, 12.6 ml of 4.76M H_3PO_4 solution were poured to have a Ca/P ratio of 1.67. Then, 64.5 ml of 3M HCl were also added to the suspension to completely dissolve the carbonate and obtain a fully transparent

solution. The pH after complete dissolution was ~1.5. The precipitation of CaP was induced by the fast addition of 96 ml of 2M NaOH, which resulted in a sudden increase of the pH to 11.3. The suspension was then stirred at 600 rpm and heated up to 45°C up to 6 h. The maturation of the reaction was monitored after 5 min, 30 min, 1 h, 1.5 h, 2 h, 3 h, 4 h, 5 h and 6 h, by sampling 100 ml of suspension. The collected sample was centrifugated to remove the supernatant, washed and resuspended with distilled water. The process was repeated to ensure the complete removal of NaCl residues. The slurry was then frozen in liquid nitrogen for 10 min and lyophilized for 72 h. A simplified scheme is shown in Figure 21. The synthesis up to 6 h was repeated four times.

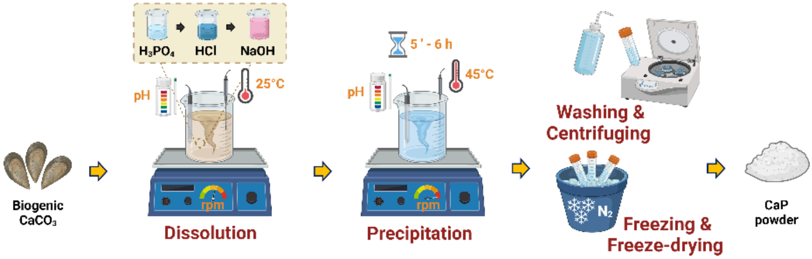

Figure 21 Dissolution-precipitation synthesis of CaPs from mussel shells.

HAp/chitosan composites were synthesised in a similar way. A relative amount of 2/5/10 wt% chitosan powder (with respect to HAp) was poured right after HCl addition (Figure 22). Once chitosan was completely dissolved, NaOH solution was added for the precipitation of CaP/chitosan composite. The suspension was heated up to 45°C for 1 h, then centrifugated, washed, resuspended and frozen in liquid N_2 for 10 min before undergoing freeze-drying for 72 h. The produced composites were labelled as HAp2Chit, HAp5Chit and HAp10Chit.

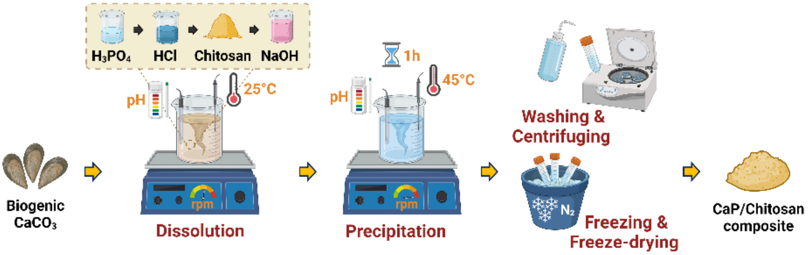

Figure 22 Dissolution-precipitation synthesis of HAp/chitosan composites from mussel shells and chitosan.

Eventually, the combination of composite synthesis and drug-loading in one step was carried out. The synthesis of HAp10Chit was repeated as previously described, but once the NaCl residues were completely removed, 0.5 g of Sr ranelate (SrRan by Zhishang Industry Co., Ltd. (CN), CAS 135459-90-4) was poured and mixed at high intensity (3500 rpm) with a Hauschild Speed Mixer® (DAC 150.1 FVZ-K) for 2 min to ensure a uniform distribution, as shown in Figure 23. The drug-loaded slurry was then frozen in liquid nitrogen for 10 min and lyophilized for 72 h.

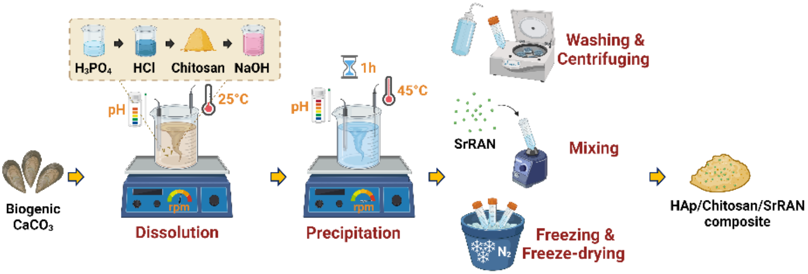

Figure 23 Dissolution-precipitation synthesis of SrRAN loaded-HAp/chitosan composites from mussel shells, chitosan and strontium ranelate.

3.2.2. Characterization of synthesised powder

Right after lyophilization, the produced powders were analysed by XRD using a PANalytical Aeris diffractometer (Malvern Panalytical Ltd) equipped with a Cu source (Kα = 8.04 keV) and operating at 40 kV and

30 mA. XRD patterns were treated by HighScore software (Malvern Panalytical Ltd), while reference patterns were collected from the International Centre for Diffraction Data (ICDD®) database. The average crystallite size ($Ø_{hkl}$) was measured by the Scherrer formula (Eq.3.1), where λ is the X-ray wavelength, β accounts for the line broadening due to size effect and θ is the diffraction angle associated to the 'hkl' plane. A stoichiometric and fully crystalline HAp by Marion Technologies was taken as a reference to determine the line broadening Eq.3.2, where Δ_S and Δ_R are the full-width at half maximum of the sample and of the reference, respectively.

$$\emptyset_{hkl} = 0.94\lambda/(\beta \cdot cos\theta_{hkl}) \qquad (3.1)$$

$$\beta = \sqrt{{\Delta_S}^2 - {\Delta_R}^2} \qquad (3.2)$$

The crystallite length was calculated considering the 002 peak, whereas the width was based on the 310 peak.

The elemental analysis was carried out by inductively coupled plasma - optical emission spectroscopy (ICP-OES) and by atomic absorption spectroscopy (AAS). ICP-EOS was performed using a Spectro Ciros Vision CDD equipment by Spectro Analytical Instruments GmbH & Co. For the analysis, about 300 µg of powder were poured into a 100 ml flask and dissolved by the addition of 10 ml of nitric acid solution (5%) and ultra-pure water (conductivity < 0.1 µS). From the 100 ml flask, 1 ml of solution was collected and poured into a 25 ml flask where additional 0.25 ml of nitric acid and ultra-pure water to complete volume were added. Such solution was finally used for the analysis. Pure hydroxyapatite (> 99.995 % trace metal basis, Sigma Aldrich, CAS 12167-74-7) was used as a standard to determine the Ca and P content in the material, while other possible elements were identified with a multi-element standard solution (type IV, Merck KGaA). AAS was carried out to determine the Ca, Mg, Sr and Na content using an iCE 3000 series AA Spectrometer (Thermo Fisher Scientific Inc.); the calibration curve for each element was obtained by standard solutions prepared from Ca, Mg, Sr and Na reference standards by SCP Science, while the blank consisted of ultrapure water enriched with 1 vol% of nitric acid (69% HNO_3, VWR-BDH Chemicals, CAS 7697-37-2), 0.5 vol% of lanthanium nitrade ($La(NO_3)_3$, SCP Science) and 0.5 vol% cesium chloride (CsCl, SCP Science). Before the AAS analysis, synthesised powders were fully dissolved in a 100 ml flask by adding 5 ml HNO_3 acid and ultrapure water. Also, carbonate content was determined by CO_2 coulometry using a UIC CM 5014 coulometer equipped with a 5130 acidification module (UIC Inc.) according to Huffman [255]. 100 mg of powder were dissolved in a closed system by adding 4 ml of 2M $HClO_4$, and the released CO_2 gas was conveyed to a photometric cell titrated through an acid-base reaction. Based on Faraday's light principle, the amount of current density is proportional to the amount of titrated CO_2. Barium carbonate ($BaCO_3$, CAS No. 513-77-9) was considered as a reference, while an empty glass bottle served as the blank. The carbonate content analysis was repeated in triplicates. Eventually, the phosphorous content was quantified by colorimetry using a UV-Vis Hitachi U-1100 spectrophotometer set on 460 nm wavelength, following the method by Gee et al. [256].The analysis permits to quantify the relative amount of HPO_4^{2-} ions in the presence of orthophosphate (PO_4^{3-}), but the presence of carbonates can interfere with the measurement, thus the powders (100 mg per sample) were initially heat-treated at 600 °C for 30 min. Calcinated powders and a reference pure HAp (Pierre InnovationHAp by Urodelia) were then poured in a 100 ml flask where 1 ml of 6M $HClO_4$ and ultrapure water were added to complete volume. Such solution was labelled as mother solution (MS). A first daughter solution was prepared to quantify the phosphate content in the hydroxyapatite (in the form of PO_4^{3-} and HPO_4^{2-}); 10 ml of MS were collected and poured in a 100 ml conical flask, where 5 ml of 6M $HClO_4$ and 5 ml of ultrapure water were added. The conical flask was hydrolysed in a water bath at 100°C for 1h. Once the solution cooled down to room temperature, 10 ml of colorimetric indicator were added as well as ultrapure water to complete volume. The colorimetric indicator consisted of a 1:1 volume of ammonium monovanadate solution (4 g/L) and ammonium heptamolybdate tetrahydrate solution (80 g/L). Conversely, the second daughter solution was prepared to quantify the amount of PO_4^{3-}; 10 ml of MS were poured in a 100 ml flask where 50 ml of ultrapure water were added. After 1h, 5 ml of 6M $HClO_4$, 10 ml of colorimetric indicator and ultrapure water to complete volume were added. A calibration curve was also prepared by four standard concentration of P and a blank solution (5 ml 6M $HClO_4$, 10 ml of colorimetric indicator and 85 ml ultrapure water). Finally, the relative amount of HPO_4^{2-} was calculated as in Eq.3.3, where the concentration of P in the daughter solutions was determined by the absorbance at 460 nm.

$$[HPO_4^{2-}] = ([PO_4^{3-}, HPO_4^{2-}] - [PO_4^{3-}])/[PO_4^{3-}, HPO_4^{2-}] \qquad (3.3)$$

The molecular structure and functional groups were determined by FTIR and Raman spectroscopy. FTIR was performed in transmittance mode using a Thermo Scientific Nicolet iS50 FT-IR spectrometer, scanning the 4000-400 cm^{-1} range with a resolution of 4 cm^{-1} (64 scans). Few μg of powder were mixed with KBr powder to produce a pellet to be analysed. Raman spectroscopy was instead carried out using a RAMAN LabRAM HR 800 confocal microscope (Horiba Jobin Yvon, Japan). The powder was placed on a slide and continuously irradiated with a diode laser at 633 nm to avoid fluorescence under an Olympus BX 41 microscope. The analysis was carried out with an objective x100, with a numerical aperture of 0.9, corresponding to a lateral and axial resolution of 0.86 μm and 3.13 μm, respectively. Spectra were acquired with a 600 lines/mm grating, with a spatial resolution of 2 cm^{-1}, and treated with LabSpec 5 software afterwards. The homogeneity of the sample was investigated with DUOScanTM imaging system for mapping. The investigated area was set 50 μm x 50 μm per each sample.

The specific surface area (SSA) was determined by Brunauer–Emmett–Teller (BET) method by using a using Quadrasorb SI surface area and pore size analyser operating with N_2 at -196°C. Before the analysis, 200 mg of powder were degassed for 24 h at 25°C in autosorb Degasser by Quantachrome Instruments to completely remove moisture, according to ISO 9277:2010. The SSA data were then used to determine the approximative powder particle size (D) under the hypothesis of spherical particle. The formula is reported in Eq.3.4, where ρ is the real density of the powder.

$$D = 6/(SSA \cdot \rho) \qquad (3.4)$$

The real density was measured in triplicates by a He Micro UltraPyc™ 1200e pycnometer (Quantachrome Instruments). The measurement was stopped only when five readings in a row had a standard deviation smaller than 0.1%. As a comparison, the theoretical density of the composites (ρ_{Comp}) was calculated according to the mixture rule in Eq.3.5, where ρ_{HAp} and ρ_{Pol} are the theoretical density, and ν_{HAp} and ν_{Pol} are the volumetric fraction of hydroxyapatite and chitosan, respectively.

$$\rho_{Comp} = \rho_{HAp}\nu_{HAp} + \rho_{Pol}\nu_{Pol} \qquad (3.5)$$

The thermal behaviour of the synthesised materials was investigated by thermogravimetric analysis (TGA) and differential scanning calorimetry (DSC), using a Mettler Toledo TGA/DSC 3+, STAR^{e} system thermobalance. About 10-15 mg of powder was heated up to 1200 °C with a 10°C/min rate under an air flow of 10 ml/min.

Eventually, the morphology of the powder was assessed by FESEM with a MIRA\LMU TESCAN and a MEB-FEG JEOL JSM 7800F Prime - EDS microscope. The samples were prepared for the analysis by Au sputtering using an EMITECH K550X sputter coater.

3.3. Results and discussions

The XRD patterns of as-synthesised powder are represented in Figure 24. The first phase forming is amorphous calcium phosphate (ACP) as shown in the 5 min pattern, characterized by two broad humps [66], [231]. ACP gradually transformed into hydroxyapatite after 1 h at 45°C, as confirmed by the HAp reference pattern (ICDD No. 00-064-0738). By comparing the repeated synthesis in Figure 24a-c, the turning point of ACP-to-HAp transformation seems to be after 30 min. Any further phase transformation of HAp could be detected up to 6 h (see Figure 24d). For this reason, 1 h was set as precipitation time for all subsequent syntheses. ACP-to-HAp transformation was further confirmed by FTIR spectra, shown in Figure 25. In particular, ACP is characterized by the water band at ~3450 cm^{-1} and ~1645 cm^{-1}, by the PO_4^{3-} signals at 1046 cm^{-1} (ν_3), 949 cm^{-1} (ν_1) and at 567 cm^{-1} (ν_4) and by carbonate peaks found at 1492 cm^{-1}, at 1426 cm^{-1} (ν_3) and at 875 cm^{-1} (ν_2), similarly to Luginina et al. [231]. The appearance of the double peak in the 600-560 cm^{-1} region in the '30 min' spectrum is a confirmation of the transformation of ACP into HAp. Such peaks are typical of apatite and correspond to the ν_4-PO_4^{3-} antisymmetric bending vibrations. Other phosphate vibration in apatite can be found at 962 cm^{-1} (ν_1), 1035 cm^{-1} and 1097 cm^{-1} (ν_3). The presence of adsorbed and structural water is evidenced by the band at 3439 cm^{-1} and 1640 cm^{-1}, whereas the signals at 1456 cm^{-1} and 1421 cm^{-1} (ν_3) and at 874 cm^{-1} (ν_2) are associated with carbonate groups, and specifically they are attributed to a B-type carbonated HAp,

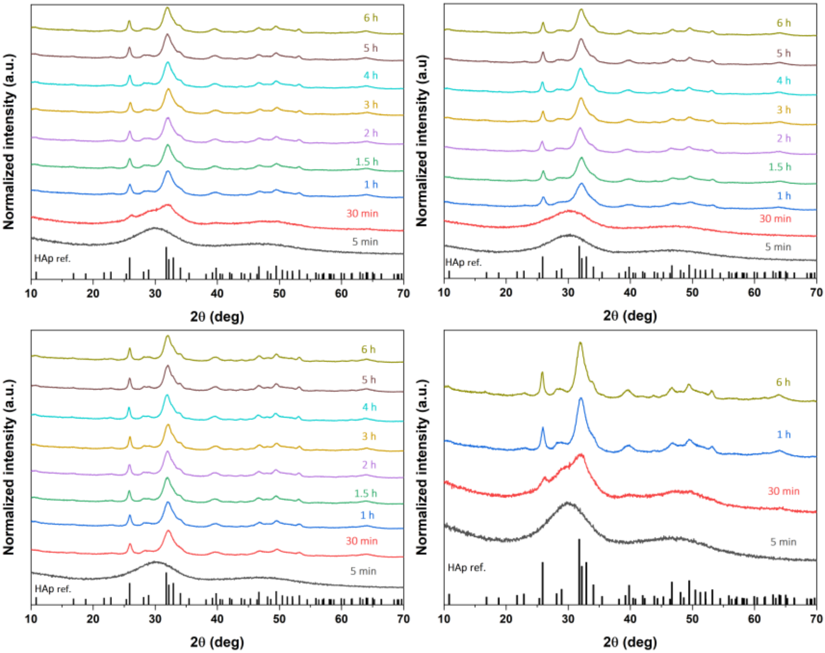

Figure 24 a-c) XRD patterns of dissolution-precipitation synthesis with a precipitation time of 5 min to 6 h in triplicates; d) XRD of the ACP-to-HAp transformation from 5 min to 6 h.

likewise bone apatite. Carbonates in the produced powder are a direct consequence of the use of mussel shells as raw materials for the synthesis.

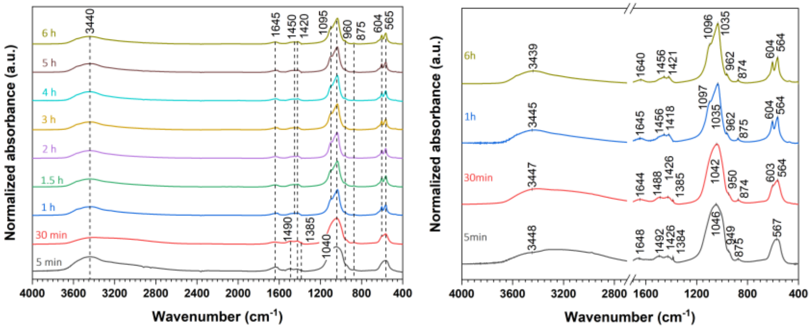

Figure 25 FTIR spectra of powder obtained by dissolution-precipitation synthesis with a precipitation time from 5 min to 6 h, (b) FTIR spectra of powder obtained after 5 min, 30 min, 1 h and 6 h of precipitation.

Furthermore, the Ca/P ratio of the synthesised HAp, determined by ICP-EOS, was found equal to 1.70 ± 0.01, in agreement with B-type carbonated HAp [37], [162]. ICP-EOS also revealed traces of Na (0.42 ± 0.06 wt%), Mg (0.08 ± 0.01 wt%) and Sr (0.06 ± 0.01 wt%). The thermal behaviour of HAp is reported in Figure 26a. The total weight loss is 11% from room temperature to 1200°C. About 8% is lost before 300°C due to the thermal evolution of adsorbed and structural water, and it is associated with a maximum rate at 90°C as shown in the derivative of TGA curve. The residual weight loss could be associated with the evolution of carbonates and to dihydroxylation because of HAp-to-TCP transformation, as shown in Figure 26b. Moreover, the true density of the powder measured by He pycnometry was found 2.68 ± 0.02 g/cm^3, lower than the theoretical density value of stoichiometric HAp (3.10-3.16 g/cm^3) reported in the literature [29], [257]. The density mismatch can be justified by the low crystallinity tenor of the powder, the ions substitution, the structural water and also to a certain level of closed porosity within the powder particles [38], [258]. In other literature works, the true density of HAp produced by dissolution precipitation was found equal to 2.94 g/cm^3 [233] and 2.83 g/cm^3 [38].

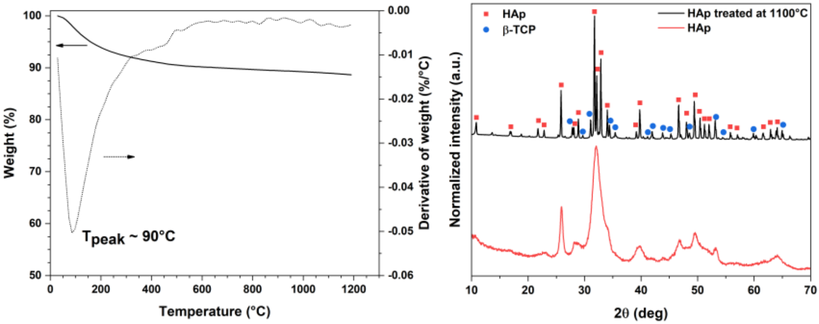

Figure 26 a) TGA-DTG curve of synthesised HAp produced by dissolution-precipitation synthesis (1 h of precipitation time); b) XRD of heat-treated HAp at 1100°C (the peaks association is based on the reference pattern of HAp (ICDD No. 00-064-0738) and β-TCP (ICDD No. 01-072-7587).

The XRD diagrams of the HAp/chitosan composites are shown in Figure 27. HAp phase is the main appreciable phase in all produced powders, according to the reference HAp pattern reported in the graph, whereas chitosan and SrRAN could not be discriminated by XRD. Due to the addition of chitosan and SrRAN, one can expect peak shifts in the diffraction pattern; however, the detected peak shifts were slight and comparable with the instrument resolution, and thus considered as not significant.

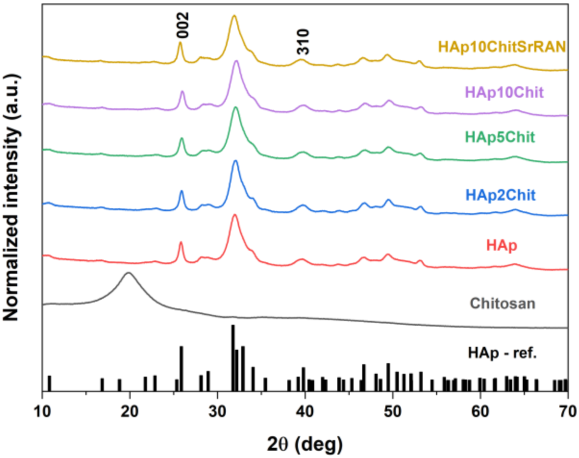

Figure 27 XRD diagrams of HAp and HAp/chitosan composites. The reference pattern of HAp (ICDD No. 00-064-0738) is also shown.

Additionally, all patterns show peak broadening which can be correlated to the presence of untransformed amorphous calcium phosphate [76], [259] but also to the nanometric size of the powder. According to the Scherrer's formula, the crystallite length of HAp, HAp10Chit and HAp10ChitSrRAN is $Ø_{002}$~12-14 nm while the crystallite width is $Ø_{310}$~6-11 nm. A similar crystallite size was reported by Benataya et al. [162] for a HAp produced by dissolution-precipitation synthesis. On the basis of SSA measurements, the average powder particle size was also estimated considering the real density measured by He pycnometry, as reported in Table 4. In addition, the measured real density agrees with the estimated theoretical density.

Sample	**SSA (m^2/g)**	**Particle size (nm)**	**Real density (g/cm^3)**	**Theoretical density (g/cm^3)**
HAp	242 ± 1	9	2.68 ± 0.02	3.10
HAp2Chit	165 ± 1	14	2.63 ± 0.01	2.63
HAp5Chit	155 ± 1	15	2.51 ± 0.01	2.57
HAp10Chit	151 ± 2	16	2.43 ± 0.01	2.47
HAp10ChitSrRAN	142 ± 2	17	2.45 ± 0.01	-*

Table 4 SSA, particle size, real and theoretical density of HAp and HAp composite powders. unavailable data of SrRAN density from the provider.*

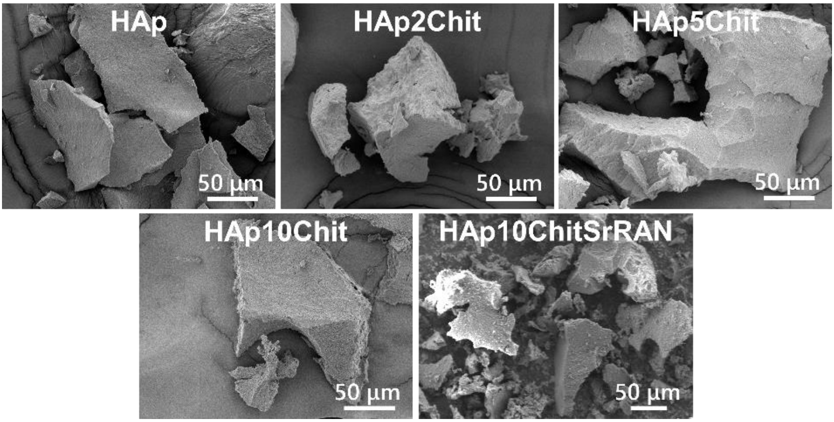

Figure 28 FESEM of HAp and HAp/chitosan composites.

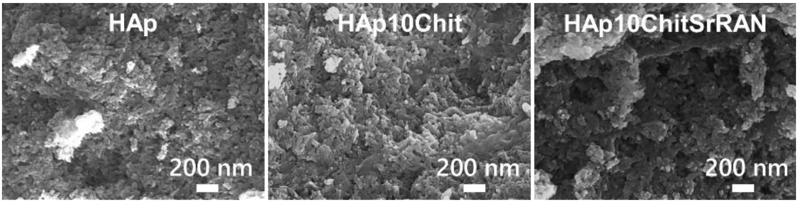

Figure 29 FESEM of HAp. HAp10Chit and HAp10ChitSrRAN powders at higher magnification.

Further investigation involved the homogeneity and the morphological aspect of the produced powders, as shown in Figure 28 and Figure 29. All powders appear agglomerated because of their nanometric size; the composite powders appeared homogeneous with the polymer uniformly distributed since any cluster of chitosan could be spotted.

To prove the presence of chitosan and SrRAN, the materials were analysed by TGA-DSC. As shown in Figure 30, the DSC curves have an exothermic peak between 250°C and 400°C associated with a weight loss in the same temperature range. The additional weight loss of the composites in comparison to HAp consisted of ~2 wt% for HAp2Chit, ~5 wt% for HAp5Chit, ~10 wt% for HAp10Chit and ~ 8 wt% for HAp10Chit5SrRAN.

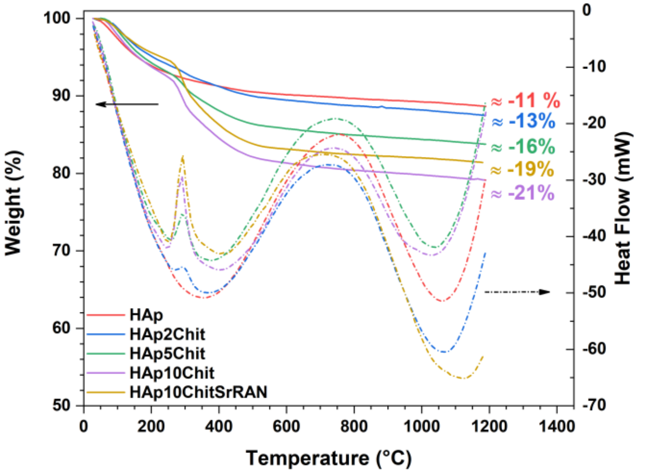

Figure 30 TGA-DSC curves of HAp and HAp/chitosan composites.

The presence of the polymer and the drug in the composite was further investigated by FTIR and Raman spectroscopy, as shown in Figure 31 and Figure 32a.

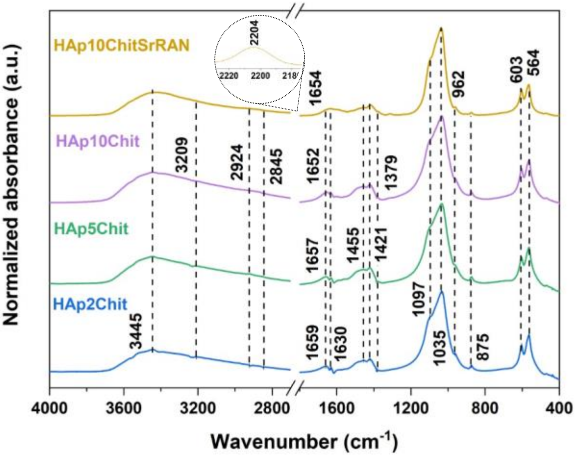

Figure 31 FTIR spectra of HAp/chitosan composites.

The IR vibrational signals of chitosan correspond to the N-H stretching at 3300-3200 cm^{-1}, the C-H asymmetric stretching at 2920 cm^{-1}, the C-H symmetric stretching at 2850 cm^{-1} and the CH_3 bending at 1380 cm^{-1}. Conversely, SrRAN was identified by the characteristic C≡N signal of ranelate at 2204 cm^{-1}, appearing both in the FTIR and in the Raman spectra. Other Raman signals of ranelate appeared at 1550 and 1518 cm^{-1} due to amide-II, at 1316 cm^{-1} due to CH_2 wagging, at 1166 cm^{-1} and 1128 cm^{-1} due C-O asymmetric vibration, at 1014 cm^{-1} C-C symmetric stretching, at 631 cm^{-1} due to C-S signal. Characteristic bands of chitosan in Raman spectra (Figure 32a) can be further identified at 3330 cm^{-1}, 3280 cm^{-1} due to the OH stretching of hydrogen bonds, at 2929 cm^{-1} and 2885 cm^{-1} due to the stretching of CH_3 and CH_2 respectively, at 1400 cm^{-1} and 1365 cm^{-1} due to CH in-plane bending vibration, at 1185 cm^{-1} related to the C-O-C stretching signal and the pyranoid ring stretching of CH_2 peak at 901 cm^{-1} [260], [261]. Eventually, typical HAp bands were the OH band at 3568 cm^{-1}, the B-type carbonate signals at 1070 cm^{-1} (ν_1), the phosphate vibrations at 1045 cm^{-1} (ν_3), at 962 cm^{-1} (ν_1), at 608 cm^{-1} and 590 cm^{-1} (ν_4) and at 430 cm^{-1}(ν_2) [262]–[264]. Signals in the 1770-1650

cm^{-1} range can be assigned to C=O, C=C, while the peak at 1385 cm^{-1} can be arise due to N-H vibration; such signal are most likely due to the organic matter of shells (proteoglycans, glycoproteins, etc.). In previous literature works, hydrogen bonds, ionic and/or polar interactions were indicated as possible HAp/chitosan chemical interactions [63], [265]–[267]. The slight blue shift of the C=O signal of amine type I in the composites (~1659 -1652 cm^{-1}) with respect to the C=O peak in pure chitosan (~1660 cm^{-1}) can be ascribed to hydrogen bonds between OH groups of HAp and NH_2 groups of chitosan, as previously reported by Ressler et al. [63] and Ansari et al. [265].

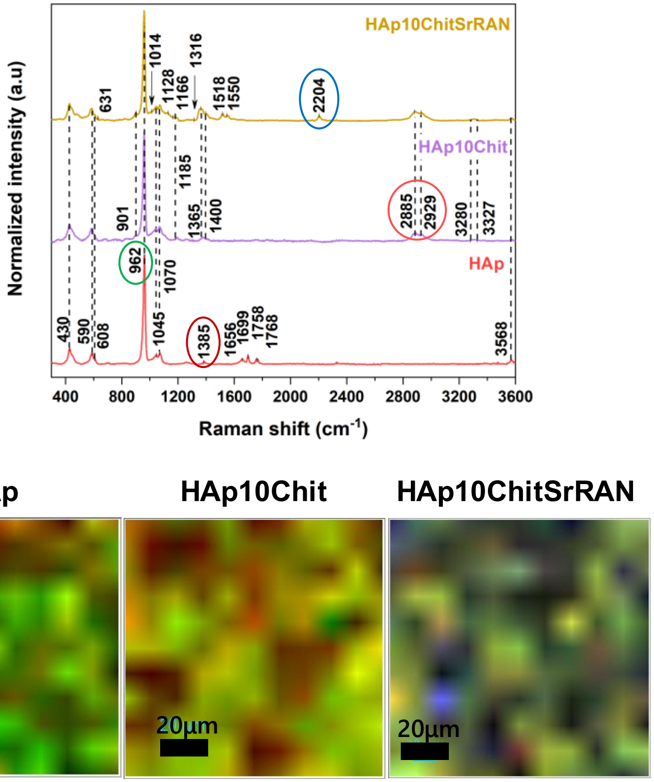

Figure 32 a) Raman spectra of HAp, HAp10Chit and HAp10ChitSrRAN powders. The circles represent the considered peaks for Raman mapping. b) Raman maps showing the distribution of apatite (green), shell organics (cayenne), chitosan (red) and SrRAN (blue).

On the contrary, the bending vibration of water at ~1640 cm^{-1} for HAp is red-shifted to ~1630 cm^{-1} in the composites. Such infrared shifts can be consistent with HAp/chitosan interactions. The homogeneity of HAp and HAp/chitosan composites was also pointed out by Raman maps (Figure 32b). Chitosan and SrRAN seems quite homogeneously distributed even if some clusters could be present, whereas the shell residual organics are not present in all the considered area, but organized in some noticeable clusters.

Likewise HAp, the elemental analysis revealed the presence of substitutions in the HAp/chitosan composites as shown in Table 5. Substitutional ions like Na^+, Mg^{2+} and Sr^{2+} were found in all the samples and the higher amount of Sr in the HAp10ChitSrRAN is a further confirmation of the presence of the drug. As previously demonstrated, HAp is carbonated with an average carbonate content of ~3 wt%, which is the range (2-8 wt%) of bone apatite [37], [268]. As mentioned, ion substitution is a fundamental feature of bone apatite, which represent a reservoir of metallic ions important for many biological activities [32], [269]. In particular, Sang Cho et al. [270] observed that Na-substituted HAp is more osteoconductive than stoichiometric HAp. Analogously, Landi et al. studied the effect of Mg-substituted HAp and demonstrated the beneficial effect of Mg on mesenchymal stem cells and osteoblastic like cells in terms of adhesion and proliferation. Eventually, Sr is a well-know agent affecting mineralization and bone remodelling as proved by Frasnelli et al. [241] and Stipniece et al. [242].

According to the collected data, the Ca/P ratio was calculated, and it resulted in 1.67 ± 0.02 for HAp, 1.62 ± 0.02 for HAp10Chit and 1.71 ± 0.02 for HAp10ChitSrRAN, in line with other natural source-derived hydroxyapatite [80], [93], [155], [271]. Finally, considering the anionic and cationic substitutions, the $(Ca+Mg+Sr+Na)/(P+CO_3)$ ratio decreased to 1.43 ± 0.02 for HAp, 1.41 ± 0.02 for HAp10Chit and 1.57 ± 0.02 for HAp10ChitSrRAN, similarly to previous studies [242], [272]–[274].

Substitutional ions	**HAp (wt%)**	**HAp10Chit (wt%)**	**HAp10ChitSrRAN (wt%)**

Ca^{2+}	30.19	29.55	30.17
PO_4^{3-}	18.13	18.25	17.70
HPO_4^{2-}	0.15	0.26	0.26
Na^{+}	0.34	0.32	0.29
Mg^{2+}	0.05	0.04	0.05
Sr^{2+}	0.09	0.08	1.36
CO_3^{2-}	3.3 ± 0.2	3.1 ± 0.2	2.6 ± 0.2

Table 5 Elemental composition of HAp, HAp10Chit and HAp10ChitSrRAN, obtained by AAS, carbonate coulometry and phosphate colorimetry.

3.4. Conclusions

Dissolution-precipitation synthesis is a versatile synthesis method, which allows the robust production of nanocrystalline HAp but also of HAp/chitosan composites in a single step. Furthermore, the synthesis process was successfully implemented for the production of a drug loaded-HAp/chitosan composite with the idea of improving the HAp mechanical and biological responses by adding chitosan and SrRAN, respectively. The produced powders resulted nanometric but agglomerated, and homogeneous with an uniform distribution of the biopolymer and the drug in the bioceramic.

Chapter IV Conventional and Non-conventional sintering of mussel shells-derived hydroxyapatite

4.1. Introduction

The present chapter is focused on the cold sintering of mussel shell-derived hydroxyapatite and on the comparison between solid-state sintering and cold sintering of HAp powders to produce dense body, having mechanical and biological properties suitable for bone tissue reconstruction. Cold sintering was carried out at a maximum temperature of 200°C, whereas conventional sintering took place above 1000°C. In addition to physico-chemical characterization, the pellets were subjected to piston-on-three-ball flexural bending test, and to a preliminary in-vitro investigation by evaluating cytotoxicity, adhesion and spreading of human bone marrow mesenchymal stem cells.

The majority of this chapter content can be found in [237].

4.2. Materials and methods

Mussel shell-derived HAp was produced by mechanochemical synthesis at room temperature, as described in Chapter II. A commercial hydroxyapatite powder nanoXIM HAp 202 (particle size 5 µm by Fluidinova, S.A., CAS 12167-74-7) was also used as a comparison.

In an agate mortar, a ceramic paste was produced by manually mixing 0.4 g of shell-derived HAp with a 0.1 M acetic acid (CH_3COOH, CAS 64-19-7, J. T. Baker), 0.1 M phosphoric acid (H_3PO_4 85 wt% in H_2O, CAS 7664-38-2, Sigma-Aldrich) or 0.1 M ethylenediaminotetraacetic acid (EDTA, $C_{10}H_{14}N_2Na_2O_8 \cdot 2H_2O$, CAS 6381-92-6, Sigma-Aldrich) solution. The pH of the solution was estimated with a litmus kit. The solution was added in a variable amount between 0 to 30 wt%. The obtained ceramic paste was poured into a cylindrical hardened 440C stainless steel die (Ø =13 mm, Specac model No.GS03000) and then pressed with a servo-hydraulic Material Testing System (MTS 810) machine. An external heating system was coupled with the mechanical testing machine, and it consisted of a heating ring wrapped around the die and connected to a Gefran 1101 controller. The temperature was controlled with a S-type thermocouple connected to a DMM6500 1/2 digit multimeter by Keithley and inserted in a hole of the die without being in direct contact with the ceramic paste. The temperature applied during cold sintering varied from room temperature to 200°C. Cold sintering was performed in two steps to promote the intimate contact between the ceramic powder and the liquid phase. In the first step, the paste was pressed at 50 MPa at room temperature for 5 min, then the pressure was increased to 300 MPa to 600 MPa and held for 15 to 30 min. The displacement data of each test were corrected by subtracting the contribution of the die and the machine. Such contributions were determined by a calibration curve, recorded by running a test with an empty die, under the same processing conditions (pressure, temperature and holding time). Cold sintered samples were labelled as CS-300, CS-500 and CS-600, according to the maximum applied pressure. A scheme of the process is shown in Figure 33.

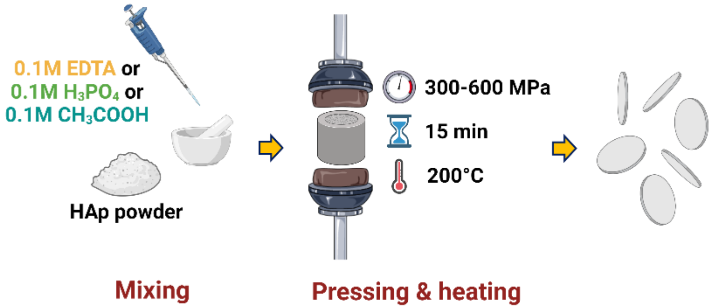

Figure 33 Scheme of HAp cold sintering.

As a comparison, 0.4 g of commercial HAp were dry-pressed at room temperature at 115 MPa and then conventionally sintered at 1050°C and 1200°C for 2 h in a Nabertherm P330 muffle furnace (heating rate, 5 °C/min). Conventionally sintered HAp was labelled as s-HAp1050 and s-HAp1200 according to the sintering temperature.

Cold sintered pellets were investigated by XRD using a Italstructures IPD3000 diffractometer, equipped with a Co-Kα (λ= 1.789 Å) source and a Inel CPS120 detector. The XRD data were then manipulated with MAUD software based on Rietveld method. The reference patterns were collected from Crystallographic Open Database (COD). Also, the FTIR spectroscopy was carried out on the sintered bodies, by using a Nicolet Avatar 330 FTIR spectrometer. After being incorporated in a KBr pellet, the material was analysed in transmittance mode (64 scans) from 4000 to 400 cm^{-1} wavenumber with 2 cm^{-1} spectral resolution.

The bulk density of the sintered pellet was determined according to the ASTM C373 standard. The samples were dried, placed in vacuum for 15 min and weighted prior to be immersed in distilled water. The suspended mass was determined after 10 min of immersion, while the saturated mass was weighted after gently blotting the surface of the sample to remove the visible superficial water. The relative density was calculated taking 3.1 g/cm^3 as the theoretical density for HAp.

The flexural strength was measured with the piston-on-three ball flexural bending test REF. The sample surface in contact with the piston was coated with a tape in order to have a uniform distribution of the load. Based on the mean pellet thickness, the loading rate was set at 15 N/s. The flexural strength was calculated as reported in Eq.4.1, where P is the rupture load, t is the thickness of the pellet, a is the radius of the supporting circle, b is the radius of the ram tip, R is the radius of the pellet and is the Poisson's ratio (0.27 for HAp, according to [29]).

$$\sigma_f = -0.2387\,(P(X-Y)/t^2) \qquad (4.1)$$

$$X = (1+\nu)\ln(b/R)^2 + [(1-\nu)/2]\,(b/R)^2 \qquad (4.2)$$

$$Y = (1+\nu)\,[1+\ln(a/R)^2] + (1-\nu)(a/R)^2 \qquad (4.3)$$

The test was carried out on 10 replicates for each condition. The failure probability (P_f) was calculated based on the collected mechanical data (Eq.4.4), where j is the rank in the ascending ordered strength distribution and N is the total number of tested samples. The failure probability can be correlated with the flexural strength by the Weibull distribution (Eq.4.5), where σ_θ is the scale parameter (or Weibull characteristic strength) and m is the shape parameter (or Weibull modulus), respectively.

$$P_f = (j - 0.5)/N \qquad (4.4)$$

$$P_f = 1 - \exp[-(\sigma/\sigma_\theta)^m] \qquad (4.5)$$

Finally, Eq.4.5 can be further manipulated to have a linear relationship (Eq.4.6), where m represents the slope of the linear curve and indicates the scattering of the mechanical data.

$$\ln(-\ln(1 - P_f) = m\,(\ln \sigma/\sigma_\theta) \qquad (4.6)$$

The fracture surfaces after mechanical test were observed by scanning electron microscopy using a JEOL JSM-5500 microscope. The samples were coated with a Pt/Pd thin layer prior to be analysed.

In view of the biomedical applications, a preliminary in vitro investigation was carried out. The specimens were sterilized in autoclave at 121°C for 45 min. Cytotoxicity was evaluated by lactate dehydrogenase (LDH) assay by Thermo Fisher Scientific according to the EN ISO 10993-12:2004 and 10993-5:2009 standards. Human lung fibroblasts (MRC5) were cultured up to 70% confluence in the standard medium composed of MEM (21090-022, Gibco), fetal bovine serum (ECS0180L, Euroclone), L-glutamine (ECB3000D, Euroclone), sodium pyruvate (11360-039, Gibco), nonessential aminoacids (M7145, Sigma Aldrich) and antibiotic/antimycotic (ECM0010D, Euroclone). Both cold sintered and conventionally sintered HAp pellets were placed in a 96-well plate and immersed in the standard medium for 72 h. After that, such (conditioned) medium was collected and used as the culture medium for cells for 24 h and 48 h. The positive and negative control for the experiment consisted of fully lysate cells and cells in the standard medium, respectively. LDH is an enzyme released by cells during their apoptosis, and it was determined with a Tecan Infinite 200 plate reader by measuring the absorbance at 490 nm and the background at 680 nm. According to the standard a material is cytotoxic if its LDH value overcomes 70% in comparison to the positive control (LDH=100%). The measurement was repeated on five replicates per condition. Finally, the adhesion of human bone marrow mesenchymal stem cells (hBM-MSC) was evaluated by confocal microscopy, using an A1 Laser Microscope (Nikon Instruments Europe BV). The culture medium for hBM-MSC cells was prepared by mixing MEM Alpha Medium (ECM0849L, Euroclone), 15% fetal calf serum (ECS0190L, Euroclone) and 1 % antibiotic/antimycotic (ECM0010D, Euroclone). Early adhesion was evaluated at day 1 and day 5 after seeding, considering three cell densities (15 000, 20 000 and 25 000 cells/well). Prior to undergo confocal imaging, seeded cells were fixed with 4% formaldehyde. Finally, cell membranes were permeabilized with Triton X-100 at 0.2 % in phosphate-buffered saline (PBS) solution, to allow the staining of the nuclei and cytoskeleton with 4,6 diamidino 2 phenylindole, dilactate (DAPI, Sigma Aldrich) and rhodamine phalloidin (Thermo Fisher Scientific), respectively.

The mechanical and biological data are reported as mean value standard deviation. Ordinary one-way ANOVA statistical treatment and Tukey’s multiple comparison test were also carried out by using GraphPad Prism 9 software (by Dotmatics),

4.3. Results and discussion

The optimal amount of liquid phase to be used during cold sintering was investigated with some preliminary experiments, where the amount of 0.1 EDTA solution was varied from 0 to 30 wt%, as reported in Figure 34. In this scenario, cold sintering occurred at 200°C under 300 MPa for 15 min. The relative density increased from (66±1)% to (76±1)% by increasing the amount of added liquid phase from 0 to 30 wt%. However, no further densification was observed with a liquid phase amount above 20 wt% (i.e. 30 wt%). Therefore, 20 wt% was set as solution amount for all the subsequent tests. Densification during cold sintering seems to be driven by plastic deformation and pressure-solution creep, where dissolution, diffusion and precipitation are the main phenomena [177]–[179]. Since HAp is one of the least soluble calcium phosphates [40], cold sintering was carried out with three acid solutions to possibly trigger densification by enhancing the dissolution of HAp. However, the relative density did not change significantly by using EDTA (pH≈4), CH_3COOH (pH≈3) or H_3PO_4 (pH≈1) solution, as shown in Figure 34. Thus, EDTA solution was preferred to the others, these causing corrosion of the die and being potentially harmful for the *in-vitro* assessment.

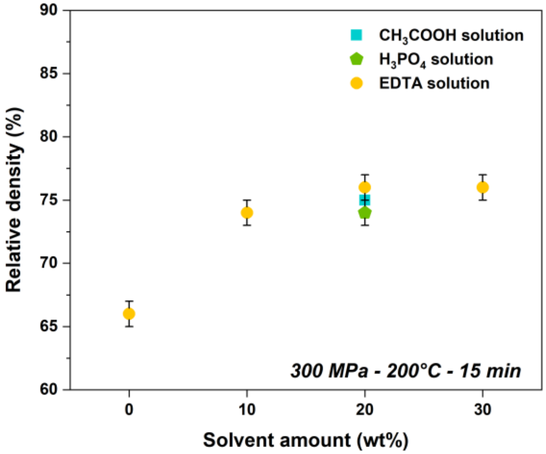

Figure 34 Relative density of HAp pellets as function of the solvent type and amount.

The role of pressure and temperature on densification during cold sintering was investigated by running the process under 300 to 600 MPa, at room temperature and at 200°C, with the same holding time of 15 min. Temperature triggers consolidation, independently from the presence of the liquid phase, as shown in Figure 35. A net increase of about 10-15% in relative density was obtained when the system was heated-up at 200°C in comparison to room temperature treatment. The relative bulk density moved from (63±0)% to (76±1)% in the presence of the solvent, while it increased from (56±1)% to (65±1)% in dry condition. Besides, pressure has a positive role on consolidation: the relative density increased from (76±1)% to (80±1)% and (80±2)% for an applied pressure of 300 MPa, 500 MPa and 600 MPa, respectively. The synergistic effect of temperature, pressure and liquid-phase supports the idea of plastic deformation and pressure-solution creep as fundamental densification pathways during cold sintering. To have a further insight on consolidation during the process, the densification curves as function of dwell time were also studied, as reported in Figure 36 and Figure 37. In particular, the curve HAp dry-pressed at room temperature is almost constant, it slightly increases from ~54 to ~56 % relative density and thus it leads to a green body. In contrast, density evolves when the dry-pressing is carried out at 200°C with an increment

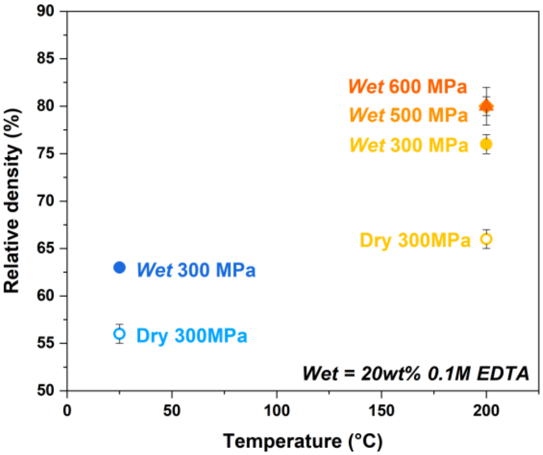

Figure 35 Relative density of HAp pellets as a function of temperature and pressure during cold sintering.

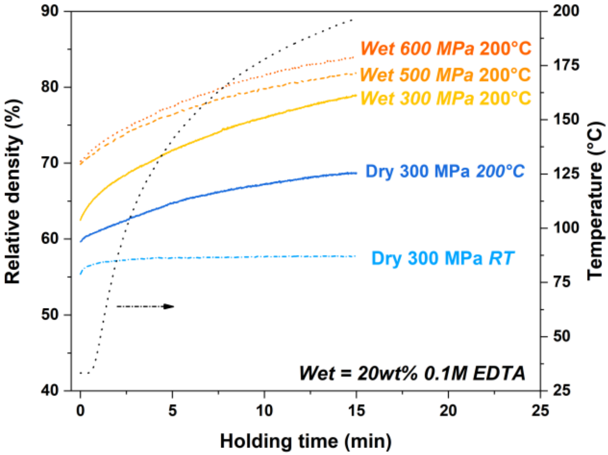

Figure 36 Densification curve of cold-sintered HAp.

to ~65%. Most likely, such density evolution is due to the removal of the adsorbed water of HAp, according to the TGA curve (Figure 20), and possibly to the activation of diffusion mechanism, although mass transport is limited at 200°C in absence of a liquid phase. When EDTA solution is mixed with HAp powder, cold sintered pellets achieve a density level above ~75%. The solvent acts a lubricant in the first stage of the process, improving the rearrangement of powder particles. In addition, it forms a thin liquid bridge among the particles, this enhancing the mass transport. It is reasonable to assume that there is a release of hydrogen and phosphate ions in the liquid phase since EDTA is a chelating agent for calcium and it forms octahedral complexes with Ca^{2+}[275]–[277]. Above 100°C when evaporation starts, the densification curve gets flatter as a consequence of the reduction in mass transport and of the slower densification rate. Once the solvent fully evaporates, the densification stops. Consequently, a dwell time longer than 15 min did not provide any improvement to densification, as shown in Figure 37.

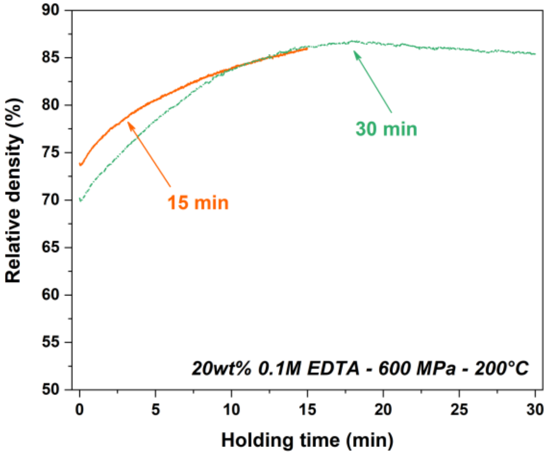

Figure 37 Relative density evolution with a holding time of 15 and 30 min.

It is remarkable that the material did not face any phase transformation during cold sintering, as demonstrated by the XRD patterns and FTIR spectra in Figure 38 and Figure 39. CS-600 pellet is characterized by the same diffraction peaks as as-synthesised HAp, whereas after solid-state sintering at 800°C the material partially transformed into β-TCP, and undergo grain growth as suggested by the sharper peaks in the XRD

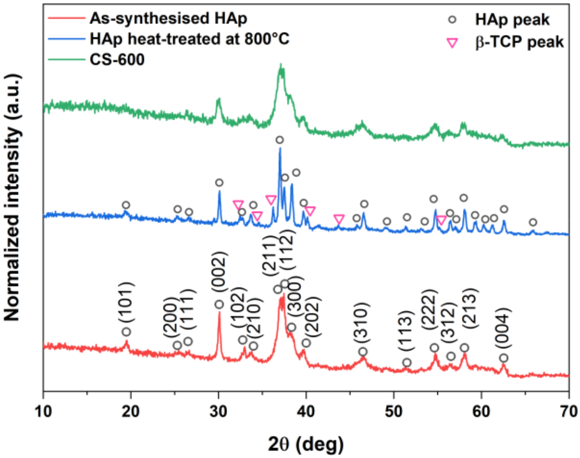

Figure 38 XRD patterns of as-synthesised HAp (red), heat-treated HAp at 800°C (blue) and cold sintered HAp at 600 MPa and 200°C (green).

pattern. Moreover, the FTIR spectra (Figure 39) of HAp and CS-600 are practically the same and show phosphate signals at 1090 cm^{-1} and 1032 cm^{-1} (ν_3), 960 cm^{-1} (ν_1), 602 cm^{-1} and 563 cm^{-1} (ν_4) and 471 cm^{-1} (ν_2), carbonates peaks at 1556 cm^{-1} (A-type), 1456 cm^{-1} (A/B-type), 1417 cm^{-1} (B-type) and 874 cm^{-1} (B-type), H_2O band at 3430 cm^{-1} and 1630 cm^{-1} , and OH peak at 3570 cm^{-1}. Additional signals were found at 3644 cm^{-1} and 632 cm^{-1} in the spectrum of heat-treated HAp at 800°C. The latter is a OH peak due to the increase in HAp crystalline tenor after high temperature treatment [278]–[280], while the former is a typical peak of CaO [281]. CaO was not detected by XRD probably because its relative amount is below the detection threshold (<1 wt%).

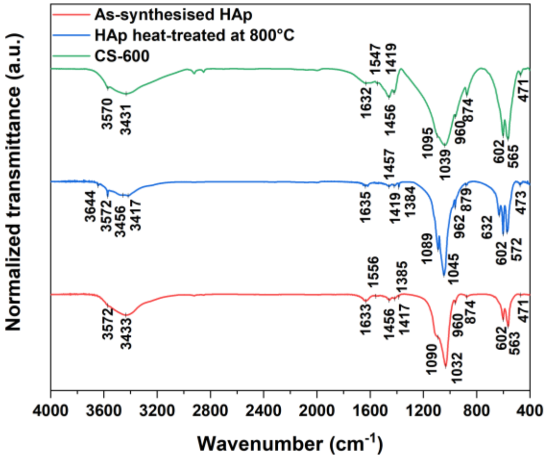

Figure 39 FTIR spectra of as-synthesised HAp (red), heat-treated HAp at 800°C (blue) and cold sintered HAp at 600 MPa and 200°C (green).

With an eye on the possible biomedical applications, cold sintered HAp pellets were mechanically tested according to the piston-on-three-ball flexural bending test. As shown in Figure 40, the mean flexural strength of sintered samples is (12±4) MPa for CS-300, (15±4) MPa for CS-500, (23±7) MPa for CS-600, (16±3) MPa for s-HAp1050 and (21±8) MPa for s-HAp1200. It is interesting to highlight that the bending strength of cold sintered HAp at 600 MPa and 200°C is similar to a HAp conventionally sintered at 1200°C; besides, the samples resulted no significant statistical different according to one way ANOVA analysis. Also, the HAp heat-treated at 1050°C shows a mechanical resistance comparable to CS-500 and in fact no statistical difference was pointed out. Such results are a practical demonstration of cold sintering great potential in strongly reduce processing energy consumption. The bending strength of CS-600 is consisted with the mechanical data reported by other studies such as spark-plasma sintered HAp [233], cold pressed and sintered HAp [282], flash sintered HAp-based composites [283] and conventionally sintered HAp/TCP composites [284].

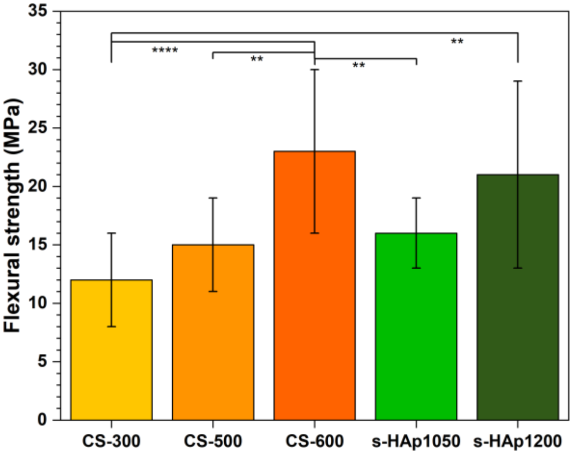

*Figure 40 Flexural bending strength of cold and conventionally sintered HAp. The values represent the mean value and the standard deviation. The statistical analysis was performed by one way ANOVA (** p<0.006, **** p<0.0001)*

The Weibull distribution of flexural bending strength is reported in Figure 41, where the slope of the linear curves corresponds to the Weibull modulus and indicates the data scattering. In particular, the modulus is equal to 3.7 for CS-300, 6.7 for CS-500, 4.0 for CS-600, 8.0 for s-HAp1050 and 2.9 for s-HAp1200.

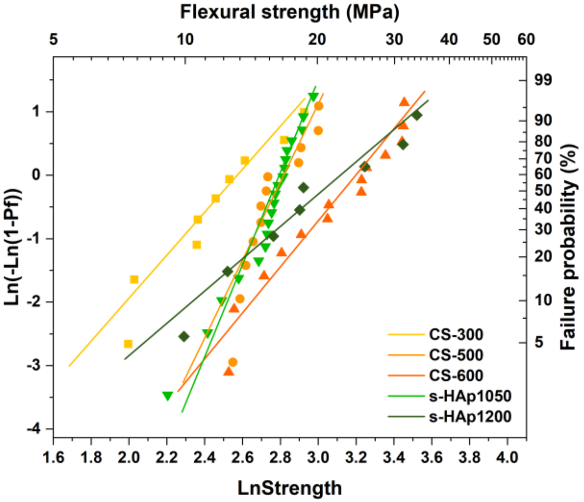

Figure 41 Weibull distribution of failure probability as function of flexural strength.

The data scattering can be correlated with the presence of lamination defects in the cross-section of cold sintered pellets, as shown in Figure 42. Delamination defects may arise due to the confinement of the

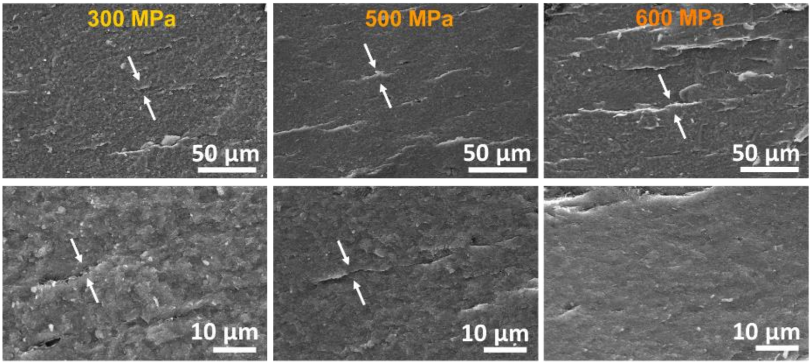

Figure 42 SEM images of cross-section of CS-300, CS-500 and CS-600.

material inside a die and in particular they are caused by the friction of the material against the die wall during compaction at high pressure [143]. The higher the applied pressure, they higher probability of delamination.

The preliminary in vitro investigation started with the cytotoxicity assessment. As reported in Figure 43, both CS-600 and s-HAp1050 are not cytotoxic for human lung fibroblasts (MRC5) after 24 h and 48 h, being their LDH value well below the toxicity threshold (30%) defined in the EN ISO 10993-12:2004 and 10993-5:2009 standards.

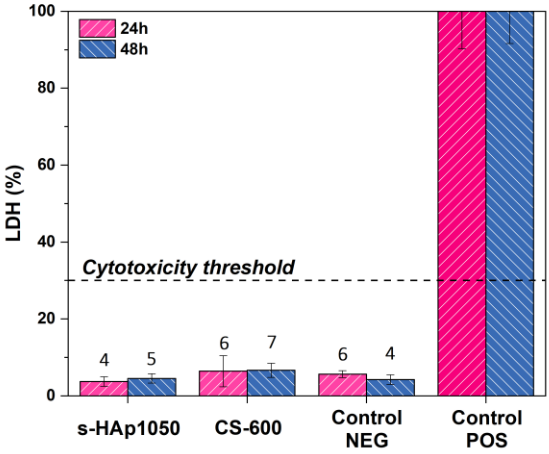

Figure 43 Cytotoxicity assessment of s-HAp1050 and CS-600 sintered body.

Finally, the early adhesion of human bone marrow mesenchymal stem cells was evaluated at day 1 and day 5 after seeding. At day 1, cells seeded on CS-600 are not homogeneously distributed around the substrate but form clusters, as shown in Figure 44. The concentration of cells in clusters is most likely due to a surface pattern and to different surface potential associated to the substitutional ions in the cold sintered HAp produced from mussel shells [32], [41], [63]. Such hypotheses can be supported by the evidence that cells organize in clusters independently from the seeded cell density. However, clusters are not isolated from each other but interconnected through some bridges as shown in Figure 44. Because cells activated, their shape start to change from round to elongated already after day 1. In contrast, cells distributed quite homogeneously on the s-HAp1050 substrate, without forming agglomerates, but their activation is slower, and their shape is still mostly round.

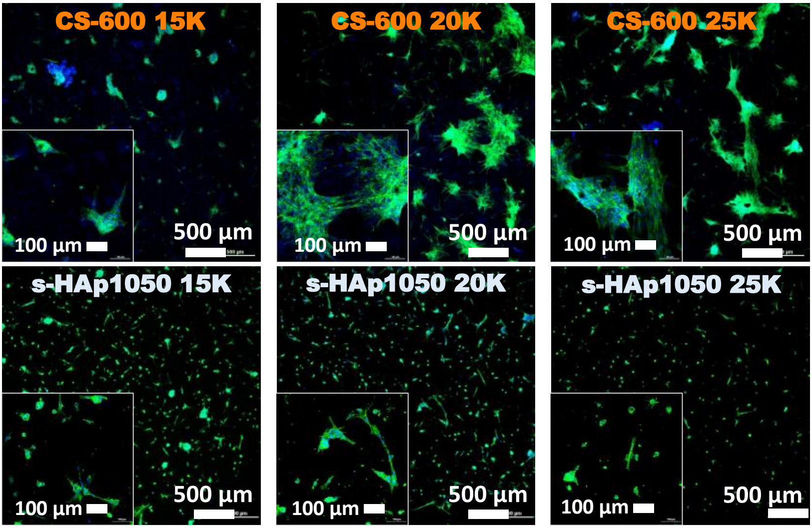

Figure 44 Confocal images at day 1 after seeding of CS-600 and s-HAp1050, with 15000, 20000 and 25000 cells/well density. In the down-left corner, images at higher magnification are reported.

At day 5 mesenchymal stem cells spread all around both substrates but proliferation seems more intense on mussel shell-derived HAp in

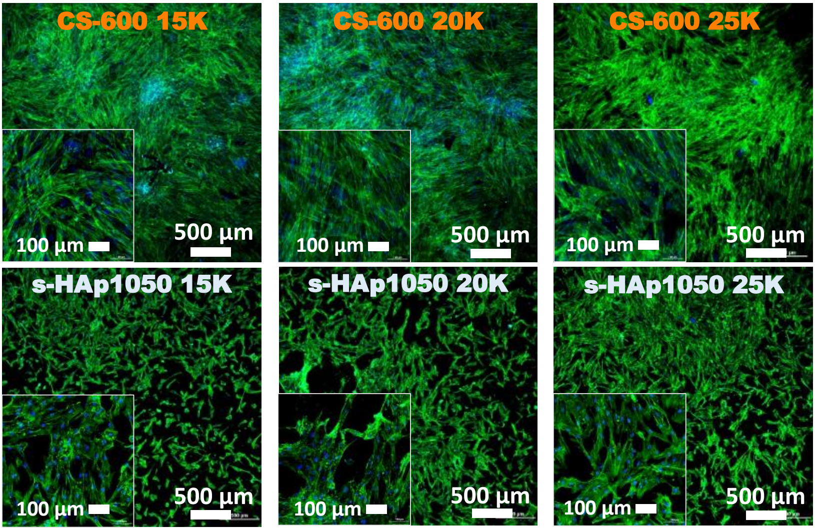

Figure 45 Confocal images at day 5 after seeding of CS-600 and s-HAp1050, with 15000, 20000 and 25000 cells/well density. In the down-left corner, images at higher magnification are reported.

comparison to synthetic HAp (Figure 45). Also, dense interconnected network of elongated cells can be found on CS-600 sample. Once again, the reason behind such different cell behaviour can be found in the presence of trace elements in biogenic source-derived HAp.

4.4. Conclusions

In the present chapter, the potential and the benefits of cold sintering were demonstrated, especially in comparison with solid-state sintering at high temperature. Cold sintered mussel shell-derived HAp showed a relative density up to 82% when heated up to maximum 200°C for 15 min under hundreds of megapascals pressure. The major role in densification is played by the external uniaxial pressure, but temperature and liquid phase also drive concurrently to consolidation. Cold sintered HAp showed comparable flexural bending strength to sintered HAp heat-treated at 1200°C. In light of bone tissue engineering applications, cold sintered hydroxyapatite resulted a promising scaffold for bone reconstruction. Mussel shell-derived HAp induced an early and fast adhesion and spreading of mesenchymal stem cells in comparison to synthetic HAp sintered at 1050°C. Stem cells activated and elongated already 24 h after seeding, while they widely proliferated forming a dense interconnected network at day 5 post seeding.

Chapter V Room temperature sintering of hydroxyapatite and hydroxyapatite/chitosan composites

5.1. Introduction

The present chapter is focused on the room temperature sintering of HAp and HAp/chitosan composites, with a particular attention to investigate if the external applied pressure could induce structural modification of the material. The mechanical properties of the sintered bodies were also investigated to evaluate the role of the polymer in improving the mechanical resistance of the composite. Nonetheless, drug-loaded hydroxyapatite/chitosan composites were also cold-sintered and tested in phosphate buffer solution (PBS) and Dulbecco's modified eagle's medium (DMEM) for their drug release. Eventually, a preliminary in-vitro assessment was carried out in light of the bone tissue engineering applications.

The work presented in this chapter was carried out during the visiting period abroad at the Baltic Biomaterial Centre of Excellence of Riga Technical University (Latvia, LV) under the supervision of Prof. Janis Locs, and at the (France, FR) in collaboration with Prof. Christele Combes.

5.2. Materials and methods

Cold sintering of HAp and HAp/chitosan composites was carried out with a PW 100 ES two-column electrohydraulic lab press (Paul-Otto Weber GmbH). About 0.4 g of powder produced by dissolution-precipitation synthesis (see Chapter III) were poured into a cylindrical die (Ø=13 mm) and pressed at room temperature from 250 MPa to 1500 MPa, with 10 min holding time. Smaller pellets were cold sintered for drug release evaluation and cellular studies by pouring 80 mg in a cylindrical die (Ø=6 mm).

Sintered pellets were analysed by XRD to identify possible phase transformation caused by the external applied pressure. XRD was carried out by a PANalytical Aeris diffractometer (Malvern Panalytical Ltd). The machine is equipped with a Cu source (Kα = 8.04 keV). The acquired patterns were analysed with HighScore software (Malvern Panalytical Ltd), where the reference crystalline phases were collected from the International Centre for Diffraction Data (ICDD®) database. Also, the molecular structure of cold sintered pellets was investigated by FTIR and Raman spectroscopy. FTIR was performed in transmittance mode by a Thermo Scientific Nicolet iS50 FT-IR spectrometer. Each spectrum was acquired from 4000 cm^{-1} to 400 cm^{-1} with a 4 cm^{-1} resolution (64 scans). Before the analysis, a fragment of pellet was crushed, mixed with KBr powder and pressed in a pellet. Raman spectroscopy was carried out with a Raman LabRAM HR 800 confocal microscope (Horiba Jobin Yvon, Japan). Cold sintered pellets were directly placed on a slide and irradiated with a diode laser at 633 nm to avoid fluorescence under an Olympus BX 41 microscope. The analysis was performed with an objective x100, with a numerical aperture of 0.9, corresponding to a lateral and axial resolution of 0.86 µm and 3.13 µm, respectively. The spectra were collected with a 600 lines/mm grating, with a spatial resolution of 2 cm^{-1}, and manipulated with LabSpec 5 software to correct the background.

The thermal evolution of sintered bodies was investigated by TGA-DSC, using a Mettler Toledo TGA/DSC 3+, STARe System thermobalance. The analysis was performed in air (10 ml/min flow) from room temperature to 1200°C with a 10°C/min rate. Before the analysis, pellets were crushed, and about 10-15 mg of each sample were placed in alumina crucibles.

The bulk density of produced pellets was determined based on the ASTM C373-18 standard, using distilled water as medium. Pellets were dried overnight at 40°C.

The flexural strength of HAp and HAp/chitosan composites was determined by biaxial flexural strength following the piston-on-three-ball test [285], [286]. A Tinius Olsen MODEL 25ST mechanical testing machine was used for the test, with the crosshead speed set at 0.33

mm/min. The pellets were dried overnight at 40°C before the mechanical test, and they were coated with a thin tape to ensure the uniform distribution of the load exerted by the piston tip. The mechanical test was performed on 10 replicates per each sample. Starting from the measured load of rupture (*F*), the flexural strength (σ_f) was calculated as in Eq.5.1., where *t* is the thickness of the sample at the fracture origin. *X* and *Y* were calculated as in Eq.5.2 and Eq.5.3., being *a* the radius of the support circle, *b* the radium of the piston tip, *R* the pellet radius and ν the Poisson's ratio (0.27 for HAp [29]).

$$\sigma_f = -0.2387[F(X - Y)/t^2] \tag{5.1}$$

$$X = (1 + \nu)\ln(b/R)^2 + [(1 - \nu)/2](b/R)^2 \tag{5.2}$$

$$Y = (1 + \nu)[1 + \ln(a/R)^2] + (1 - \nu)(a/R)^2 \tag{5.3}$$

To have a clear interpretation of the mechanical results, the data were further ranked in ascending order (i) and the probability of failure (P_f) was calculated as shown in Eq.5.4, where *N* is the total number of tested specimens.

$$P_f = (i - 0.5)/N \tag{5.4}$$

The failure probability can be related to the flexural strength by the Weibull distribution in Eq.5.5 and Eq.5.6, where *m* is the Weibull modulus (or shape parameter) and σ_θ is the Weibull characteristic strength (or scale parameter).

$$P_f = 1 - exp\left[-\left(\frac{\sigma}{\sigma_\theta}\right)^m\right], \sigma > 0 \tag{5.5}$$

$$P_f = 0, \sigma \leq 0 \tag{5.6}$$

Weibull distribution can also be transformed into a linear relationship where *m* becomes the slope of the linear curve.

$$\ln(-\ln(1 - P_f) = m\,(\ln \sigma/\sigma_\theta) \tag{5.7}$$

After flexural bending test, the cross-section of the pellet was observed by FESEM, using a MIRA\LMU TESCAN microscope. The samples sputtered with gold before the microscope observation.

Besides flexural strength, microhardness was also determined with a Mitutoyo Micro Vickers hardness testing machine (HM-200 Series). Samples were polished to a mirror finish with Buehler METADI® II diamond paste (6 and 1 µm). Vickers microhardness was calculated according to the formula in Eq.5.8, where L is the applied load (0.5 N) and d is the mean diagonal length of the imprint. Six imprints were performed on each pellet and three replicates per samples were considered.

$$H_{Vickers} = 1.854\ L/d^2 \qquad (5.8)$$

Eventually, sintered HAp/chitosan composites were immersed in 13 ml of simulated body fluid (SBF) [51], and placed in an incubator at 37°C for 7 days under continuous shaking. The swelling of the polymer was calculated as in Eq.5.9, where w_{dry} is the sample dry mass before immersion and w_{sat} is the saturated mass. Saturate mass was measured at each time point by removing the sample from SBF and gently blotting the surface to remove the superficial fluid with a microfiber cloth [287], [288].

$$Swelling\ ratio\ = (w_{sat} - w_{dry})/w_{dry} \qquad (5.9)$$

After 24 h of immersion in SBF samples were observed by FESEM to investigate the formation of a fresh apatite layer on the surface of the pellet, as a proof of material bioactivity. Furthermore, flexural bending test was carried out on cold sintered samples after 7 days of SBF immersion.

The SrRAN release kinetics of drug-loaded pellets was evaluated by Ultraviolet-visible light spectroscopy after immerging the samples in 5 ml of phosphate buffered saline (PBS 7.4 pH, Sigma Aldrich) and high glucose Dulbecco's modified eagle medium (DMEM, Sigma Aldrich). The samples were incubated at 37°C under continuous shaking (80 rpm); at each time point 2 ml of solution were collected for the analysis and replaced with fresh PBS and DMEM. The extract was poured into pure silica cuvettes and scanned at 318 nm wavelength in a two-beam UV/VIS, Evolution 300 spectrophotometer by Themo Scientific (Waltham, MA, United States). The quantitative analysis was based on a five-point calibration curve with a SrRAN concentration range from 0.8 μg/ml to 80 μg/ml. The standards were prepared by dissolving SrRAN in PBS and DMEM in an ultrasonic bath for 10 min and then 40 min with a magnetic stirrer at 600 rpm. The release was evaluated considering 5 replicates.

The preliminary biological in vitro tests consist of cytocompatibility, extracellular matrix mineralization and osteogenic differentiation. Before proceeding with the tests, the samples were sterilized in an Tuttnauer Elara 11 autoclave set at 121°C for 20 min.

The cytotoxicity of cold sintered samples was evaluated by indirect method according to the ISO 10993-5 standard, using the Cell Counting Kit-8 (CCK-8, Sigma Aldrich). Three pellets per condition were placed in a 15 ml falcon tube, where 2.4 ml of culture medium (DMEM + 10 vol% of fetal bovine serum (FBS, Gibco, USA) + 1 vol% penicillin/streptomycin (Gibco, USA) were added. The falcon tube was stored at 37°C in an incubator. 1 ml extract was collected after 24 h, 48 h and 72 h and it was replaced by 1 ml of fresh medium. The collected extract was sterilized with a 0.22 μm filter, and used as culture medium in three different concentrations (100%, 10% and 1%). Human osteosarcoma MG63 cells were seeded in a 96-well plate (10 000 cells/well) and, after 24 h of culture to ensure cell attachment to the well plate, cells were cultured for additional 24 h in the extracted medium in an incubator at 37°C with 5% CO_2. The negative control consisted of cells in the culture medium, while in the positive control 5% dimethylsulfoxide DMSO was added to cells. Finally, the absorbance at 450 nm was measured by a Tecan Infinite 200 PRO microplate reader.

For the osteogenic differentiation and the matrix mineralization, mouse-derived pre-osteoblasts (MC3T3-E1) were cultured in α-minimal essential medium (α-MEM, Gibco, USA), where 10% FBS and 1% penicillin/streptomycin were added, and stored in an incubator at 37°C and 5% CO_2. The culture medium was changed every two days. MC3T3-E1 cell at passage 9 were used for the experiment.

The osteogenic differentiation of the pre-osteoblasts was investigated by alkaline phosphatase activity (ALP). In particular, ALP activity was determined by measing the coloured complex formed as consequence of p-nitrophenyl phosphate (p-NPP, Sigma Aldrich) hydrolysis. Briefly, 100 μl of the supernatant from cell lysates was collected and mixed with 100 μL of ALP test solution (Tris (0.1 M), MgCl2 (2 mM), and p-NPP (9 mM)) at pH adjusted to 9.8. The resulting solution was incubated at 37°C for 30 min in the absence of light. Then, the reaction was stopped by adding sodium hydroxide (1M NaOH). The absorbance at 405 nm was then collected with a Tecan Infinite 200 PRO microplate reader. The resulting ALP activity was calculated starting from the measured absorbance, applying suitable correction factors from a standard calibration curve.

The matrix mineralization was estimated by Alizarin Red S assay at day 7 and day 14 after seeding. The cells were washed with PBS for 3 times to completely remove the culture medium, and fixed with 4% paraformaldehyde for 15 min at room temperature. Cells were then washed with deionized water, and 1 ml of 40 mM Alizarin Red dye was added per each well. The well plate was gently shaken for 30 min at room temperature to allow the dye to permeate the extracellular matrix. The dye was then collected, and cells were repeatedly washed with deionized water to completely remove dye residuals. A first qualitative mineralization assessment was carried out by observing the samples with a Fluo Optika fluorescence microscope set in optical mode. Conversely, the well plates were stored at -20°C prior to dye extraction for the quantitative analysis of matrix mineralization. After that, 800 μl of 10% acetic acid were added to each well, and incubate at room temperature for 30 min under gentle shaking. Cells in 10% acetic acid were then collected, transferred to 1.5 ml falcon tubes to undergo vortex for 30 s. The samples were then heated up to 85°C for 10 min, and placed on ice to incubate for 5 min. Once completely cooled down, the tubes were centrifuged at 20 000 g for 15 min; 500 µl of the resulting supernatant were collected and aliquoted in a 96-well plate (100 µl per well). The well plate was then placed in a Tecan Infinite 200 PRO microplate reader set at 405 nm wavelength to record the absorbance. A calibration curve was built starting from standards of 40 mM Alizarin Red S solution (from 0.0313 mM to 2 mM).

Mechanical and biological data are reported as mean standard deviation. Ordinary one-way ANOVA was carried out as a statistical analysis by using GraphPad Prism 9 software (Dotmatics).

5.3. Results and discussion

HAp and HAp/chitosan composites were cold sintered at room temperature under several pressure values, as shown in Figure 46 and Figure 47. The pressure was varied both to identify the most suitable load to trigger the material consolidation and to verify if there is a maximum pressure above which the material undergoes structural modification. In general, one can observe an increase in densification by increasing the applied pressure. In particular, the relative density of cold sintered HAp moved from (60 ± 1)% at 250 MPa to (96 ± 1)% at 1500 MPa, while HAp10Chit and HAp10ChitSrRAN density ranged from (65 ± 0)% to (98 ± 0)% and from (66± 0)% to (98± 1)%, respectively. No significant difference in terms of density was found between the three samples (HAp, HAp10Chit and HAp10ChitSrRAN). Although the highest density was achieved when 1500 MPa pressure was applied, pellets were proner to crack and develop surface defects, most likely because of the intense spring-back. Conversely, a relative density of ~90% was achieved with 1000 MPa without recording surface defects, and, therefore, 1000 MPa was set as maximum suitable pressure for all the mechanical and biological evaluations.

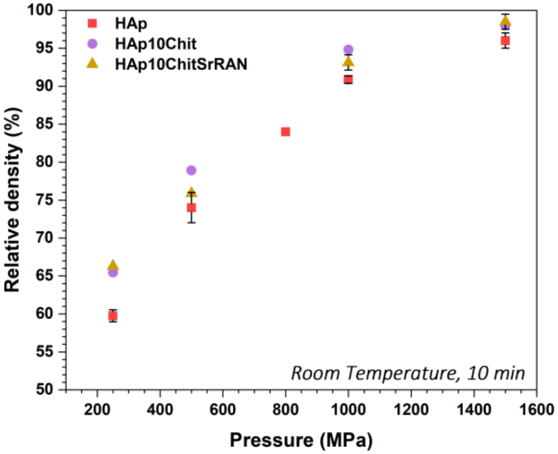

Figure 46 Relative (apparent) density of cold sintered HAp and HAp composites, under different pressure values.

In light of the used processing conditions, the densification is mostly triggered by the exerted pressure, as well as by the nanometric particle size. Interestingly, the material consolidation achieved at room temperature is comparable with cold sintered HAp processed at 200°C and 500 MPa [223], [289], and at 150°C under 600 MPa [218]. Moreover, the achieved relative density is higher with respect to sintered HAp by solid-state sintering at 1100°C for 2h (~88%) [81], and by spark plasma sintering at 150°C (~50%) [233]. Conversely, similar densification (in terms of relative density) was reported by Piccirillo et al. [81] and Reis Lavagnini et al. [290] when HAp was conventionally sintered at 1200°C for 2h holding time (~94%), or flash sintered at 1160°C (~91%) for 10 s with a current density of 3 mA/mm^2 [290].

As shown in Figure 47, under 1000 MPa HAp and HAp/chitosan composites have a relative density of ~90% and ~3-5% of open porosity by comparing the apparent with the bulk density measured though Archimedes' method. In fact, no pores were found in the cross-section of the pellets as reported in Figure 48. Both HAp and HAp composite show uniform densification with no grain orientation despite the intense uniaxial pressure applied. Some lamination defects could instead be spotted in the cross section of pellets pressed at 1500 MPa.

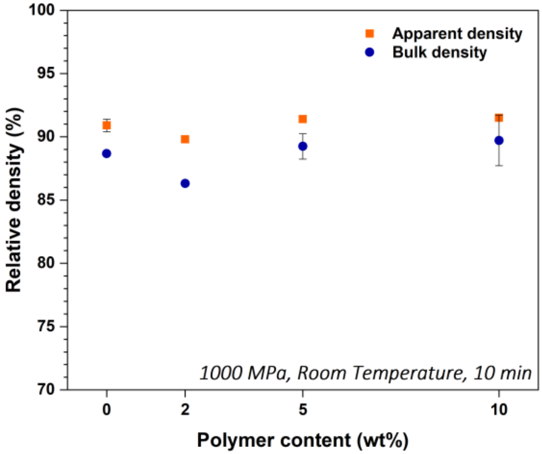

Figure 47 Relative density of HAp/Chitosan pellets sintered at room temperature under 1000 MPa.

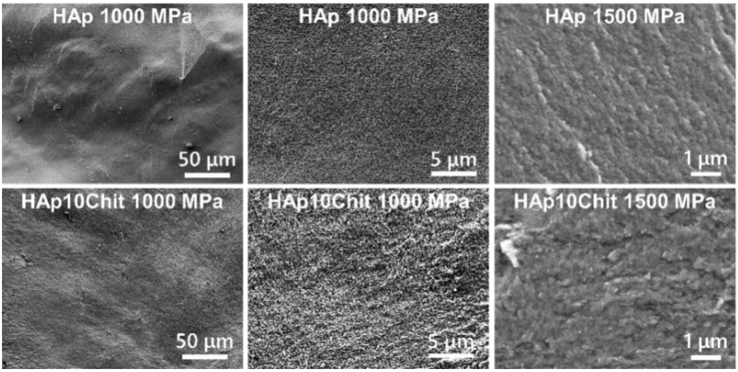

Figure 48 FESEM of the cross-section of cold sintered pellets.

It is remarkable that both HAp and HAp-based composites did not undergo any phase transformation after cold sintering, independently from the applied pressure, as Figure 49a demonstrates. However, peak

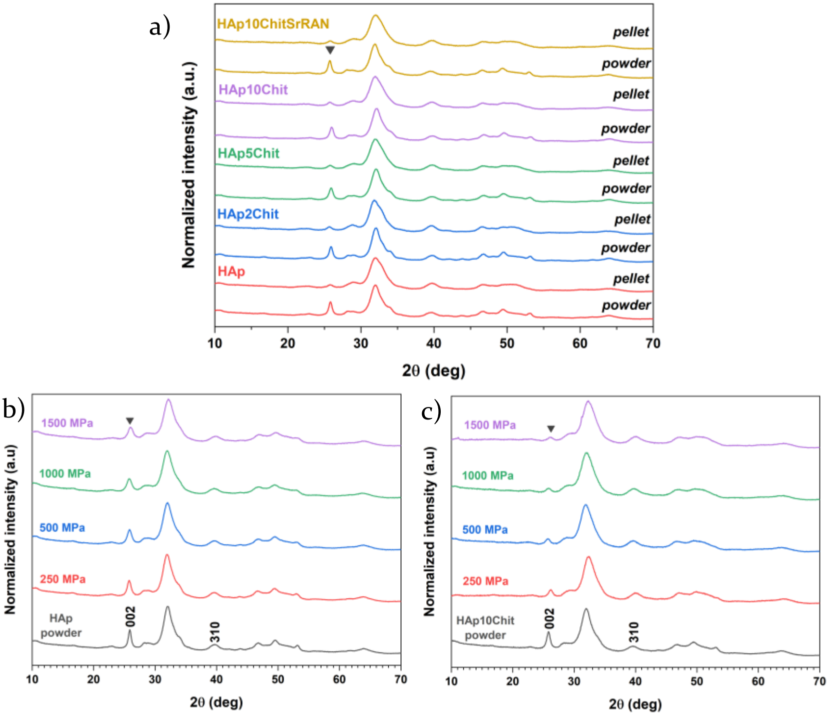

Figure 49 a) XRD patterns of HAp and HAp/chitosan composites as powder and as cold sintered pellet at 1000 MPa, and of HAp (b) and HAp10Chit (c) pellets pressed under several pressure values.

broadening was enhanced by increasing the exerted pressure, as can be observed in Figure 49b and c (especially looking at 002 peak), possibly due to material orientation, grain refinement and deformation-induced strain [291]. Even vibrational spectroscopies did not point out fundamental differences in the molecular structure of the material, by comparing the raw powder with cold sintered bodies as in Figure 50 and Figure 51. In fact, the cold sintered bodies were characterized by the same infrared and Raman signals of the as-synthesised powder discussed in Chapter III, and summarized in Table 6. However, it is interesting to highlight that the Raman bands between 1770-1700 cm-1 associated to the organic residuals of mussel shells could not be spotted in the pellet, as a further proof of their uneven distribution within the produced powder.

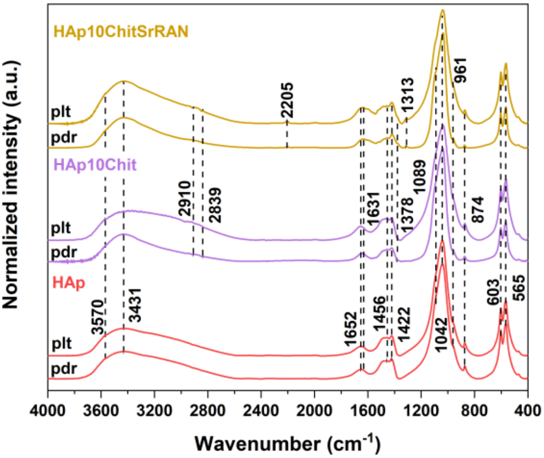

Figure 50 FTIR of HAp and HAp/chitosan composites as a powder (pdr) and as a cold sintered pellet (plt) at 1000 MPa.

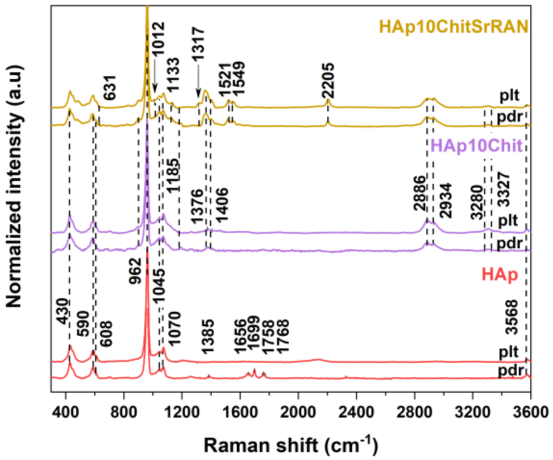

Figure 51 Raman of HAp and HAp/chitosan composites as a powder (pdr) and as a cold sintered pellet (plt) at 1000 MPa.

FTIR signal (cm^{-1})			Raman signal (cm^{-1})		
HAp	**Chit**	**SrRAN**	**HAp**	**Chit**	**SrRAN**
3570 ν_1-OH	2910 ν_3-CH	2205 ν_1-C≡N	3568 ν-OH	3327 ν-OH	2204 ν C≡N
3431 ν_3-OH	2839 ν_1-CH	1313 ν-CN	1768ν-C=C*	3280 ν-NH	1550 ν C-N
1652 ν-C=C *	1378 ν_2-CH$_3$		1758 ν-C=C*	2929 ν-CH$_3$	1518 ν C-N
1631 ν_4-OH			1699 NH	2885 ν-CH$_2$	1317 ν-CH$_2$
1456 ν_3-CO$_3$			1656 ν_1-CO$_3$	1400 CH	1166 ν_3- CO
1422 ν_3-CO$_3$			1385 ν_2-CH$_3$	1365 CH	1128 ν_3- CO
1089 ν_3-PO$_4$			1070 ν_3-PO$_4$ and ν_1-CO$_3$	1185CO	1014 ν_1- CC
1042 ν_3-PO$_4$			1045 ν_3-PO$_4$		631 ν-C-S
961 ν_1-PO$_4$			962 ν_1-PO$_4$		
874 ν_2-CO$_3$			608 ν_4-PO$_4$		
603 ν_4-PO$_4$			590 ν_4-PO$_4$		
565 ν_4-PO$_4$			430 ν_2-PO$_4$		

*Table 6 FTIR and Raman bands of HAp and HAp10Chit (Chit) and HAp10ChitSrRAN (SrRAN) composites. * peak very likely due to the organic residues of shells.*

Additionally, the thermal behaviour of the material did not change after cold sintering; the weight loss of cold sintered pellets is comparable to the powder for HAp (12±1 %), HAp10Chit (20±1 %) and HAp10ChitSrRAN (21±1 %), as shown in Figure 52.

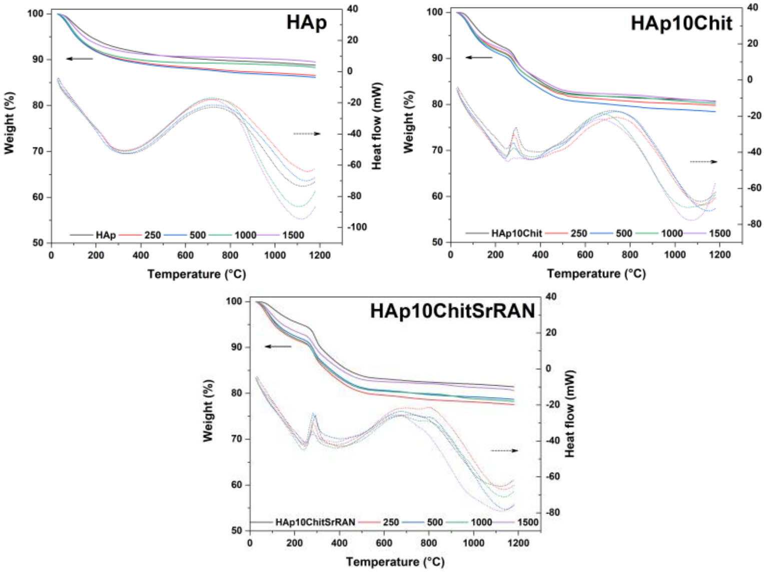

Figure 52 TGA-DSC of HAp and HAp/chitosan composites powder and cold sintered bodies.

The mechanical properties of cold sintered HAp and HAp/chitosan composites were determined by flexural bending and microhardness tests. The Weibull distribution of failure probability as function of the flexural strength is reported in Figure 53a, while the mean value of flexural strength is shown in Figure 53b. In general, the larger the polymer content, the higher the mechanical resistance of the material. The average flexural strength increases from (45±7) MPa for HAp to (44±4) MPa for HAp2Chit, to (49±8) MPa for HAp5Chit and finally to (57±6) MPa for HAp10Chit. However, according to ordinary one-way ANOVA test, HAp10Chit pellets are the only statistically different samples in comparison to HAp, whereas HAp2Chit and HAp5Chit specimens show a similar mechanical response to HAp under bending load. Thus, despite the larger mean flexural strength value, adding 2 wt% or 5 wt% of chitosan does not improve the mechanical resistance compellingly. Indeed, the Weibull plot shows a partial data overlapping of HAp, HAp2Chit and HAp5Chit. Moreover, the Weibull modulus, indicating the scatter in the data and corresponding to the slope of the linear curves, is equal to ~9 for HAp, ~12 for HAp2Chit, ~8 for HAp5Chit and ~10 for HAp10Chit. Consistently, all pellet cross-sections after bending test in Figure 54 are characterized by cracks. However, higher fragmentation can be spotted in the composites with larger polymer content, as a consequence of the larger strength exerted by the material. In comparison to other works found in the literature, the flexural strength reported in the current study is larger than HAp bodies sintered by spark plasma sintering (~18±5 MPa) by Ortali et al. [233], and sintered by conventional sintering at 900°C (~30 MPa) and at 1000°C (~40 MPa) [292]. Conversely, Pramanik et al. [282] reported a flexural bending strength of HAp sintered at 1250°C (~55 MPa). Therefore, cold sintering is a remarkable consolidation technique not only because of the dramatic reduction in processing temperature and time but also because cold-sintered HAp bodies have a mechanical resistance even superior dense HAp processed by other sintering techniques. Furthermore, Heidari et al. [293] found a flexural strength of 28±3 MPa for HAp/chitosan composites and pointed out the influence of the adhesion between the two phases on the mechanical performance of the composite. In this scenario, the larger flexural strength found in the current study could be related to a good interaction between HAp and chitosan and possibly due to an even and homogeneous dispersion of the polymer in the HAp powder. The microhardness of HAp and HAp/chitosan composites was also investigated. The mean hardness value in Figure 53c decreases by increasing the chitosan content from 1.14±0.04 GPa for HAp, to 0.97±0.07 GPa for HAp2Chit, 0.97±0.09 for HAp5Chit and 0.77±0.02

GPa for HAp10Chit, being chitosan a softer material than HAp. The microhardness results are consistent with the cortical bone apatite values found in porcine, bovine and deer [294]–[297], and also slightly higher than the hardness of human bones reported in the literature [298], [299]. For example, bone hardness ranges from 0.2 GPa to 0.8 GPa depending on the mineralization degree [298], and also on the anatomical location (proximal metaphysis 0.33±0.06 GPa, diaphysis 0.42±0.05 GPa and distal metaphysis 0.35±0.05 GPa) according to Wu et al. [299].

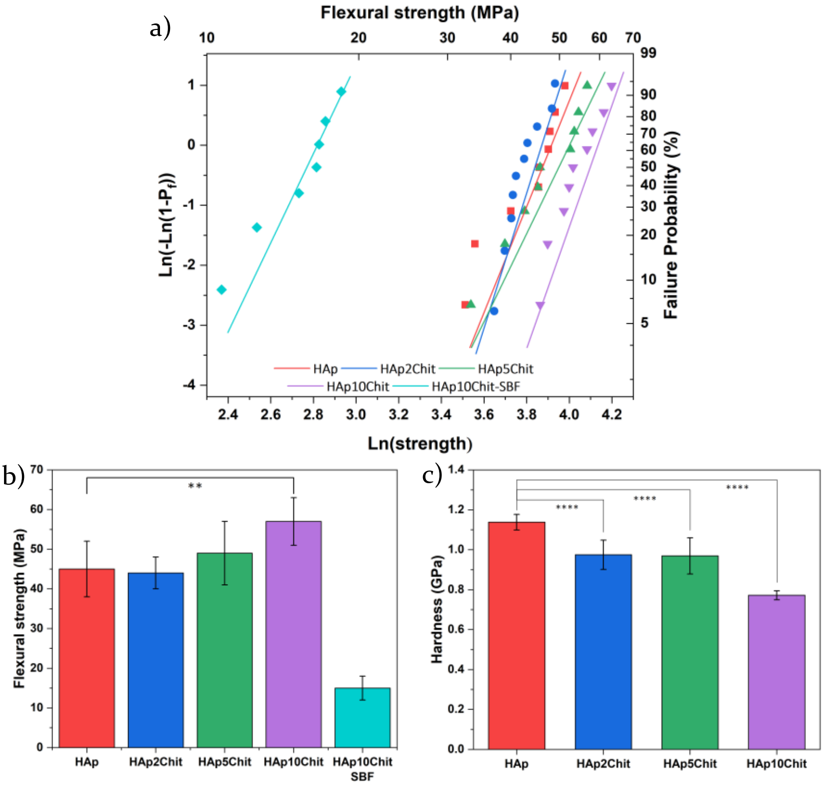

*Figure 53 a) Weibull distribution plot showing the failure probability as function of flexural strength of HAp/Chit sintered pellets (HAp10Chit pellets were tested in dry condition and after 7 days immersion in SBF solution), Flexural strength of HAp/Chit sintered pellets (HAp10Chit pellets were tested in dry condition and after 7 days immersion in SBF solution), c) Microhardness of HAp/chitosan composites (**: p-value<0.005, ****: p-value<0.0001).*

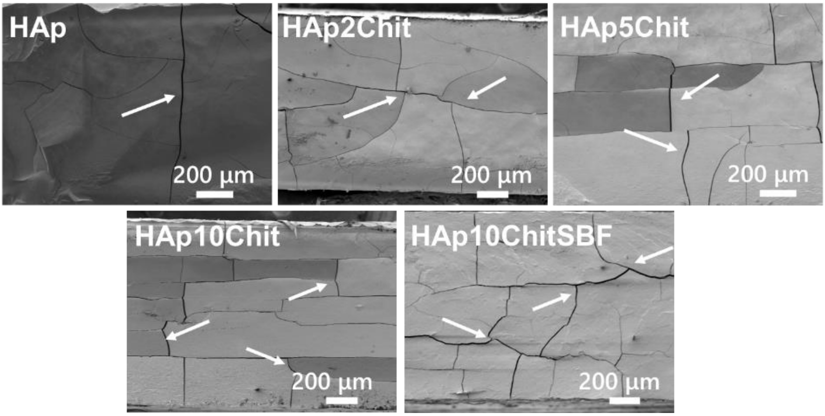

Figure 54 FESEM of HAp and HAp/chitosan composite cross-section after bending test.

The preliminary acellular in vitro assessment evaluated the bioactivity of cold sintered HAp and HAp10Chit. According to the literature [52], a material can be addressed as bioactive if fresh apatite crystals develops on the surface of the material post immersion in simulated body fluid. Consequently, both HAp and HAp10Chit were proved to be bioactive because of the presence of apatite flakes on the pellets surface after 24 h immersion in SBF, as shown in Figure 55. In addition, the polymer swelling of HAp10Chit composite consisted in ~10% after 3.5 h of immersion without any further variation after 7 days, as shown in Figure 56a and b.

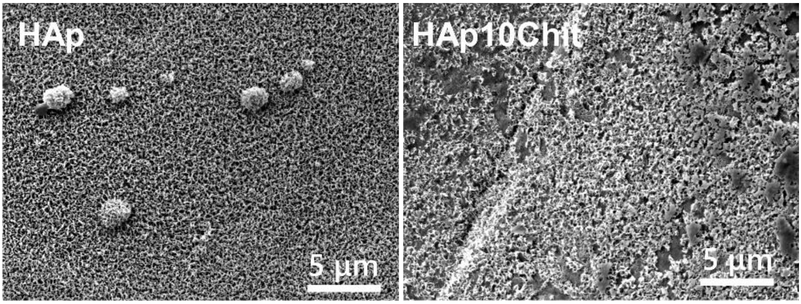

Figure 55 FESEM of HAp and HAp10Chit pellet surface post SBF immersion for 24 h at 37°C.

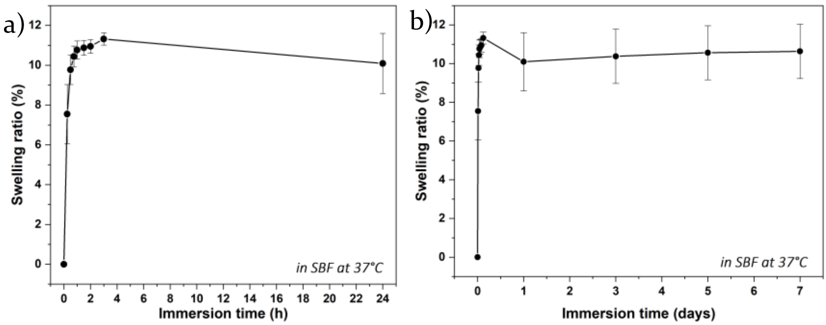

Figure 57 Swelling ratio of HAp10Chit from 30 min to 1 day (a) and to 7 days (b).

Nonetheless, HAp10Chit pellets were mechanically tested after 7 days of SBF soaking, revealing a bending strength of 15±3 MPa. The net reduction in the mechanical resistance after SBF immersion could be justified by swelling, capillary forces arising due to the presence of liquid in open pores, additional pores forming due to ions diffusion from the pellet to the SBF solution [300]–[302]. In fact, Gu et al. [300] also observed a decrease in the mechanical response of HAp composite and addressed it to porosity and surface reaction after SBF soaking. Likewise pellets tested in dry conditions, HAp10Chit pellet shows microcracks in the cross-section (Figure 54), which can be also arise due to the SBF immersion, as previously reported in the literature [300].

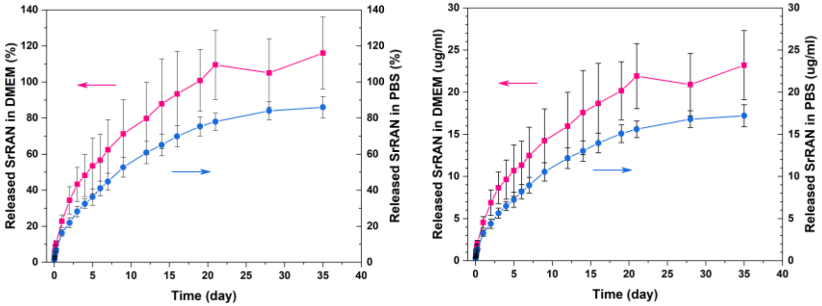

Figure 56 SrRAN release in PBS and DMEM.

The biological properties of cold sintered HAp and HAp/chitosan composites were also investigated. At first, the drug release of HAp10ChitSrRAN was monitored for 35 days in PBS and DMEM solution. SrRAN is gradually freed for 15 days in DMEM and for more than 35 days in PBS as shown in Figure 57. The dissimilar behaviour of SrRAN release in DMEM and PBS could be associated with a different material solubility and ions diffusion [303], [304]. Moreover, the microstructure and the swelling of the composite pellet can affect the diffusion mechanisms governing the release. In fact, the limited porosity (3-5% according to the Archimedes' method previously discussed) and small pores slow down the release kinetics [303]. Conversely, swelling should enhance the release because it increases the material/solution exchange regions and thus promotes diffusion [303], [304]. However, the swelling of HAp/chitosan composite was limited (~10%) and stable in time without any further evolution after the first three hours post liquid immersion. Such sustained profile allows a prolonged SrRAN release (15 days at least), necessary for the drug to play an effective action on bone remodelling, even if longer-term SrRAN therapy are preferable [251], [252].

The materials were proved to cytocompatible after 24 h, 48 h and 72 h, as Figure 58 demonstrated. In fact, all samples had a survival rate larger than 70%, the viability threshold according to the ISO 10993-5:2009 standard. Therefore, the ions released by the cold sintered pellets once immersed in the cultured medium were not cytotoxic.

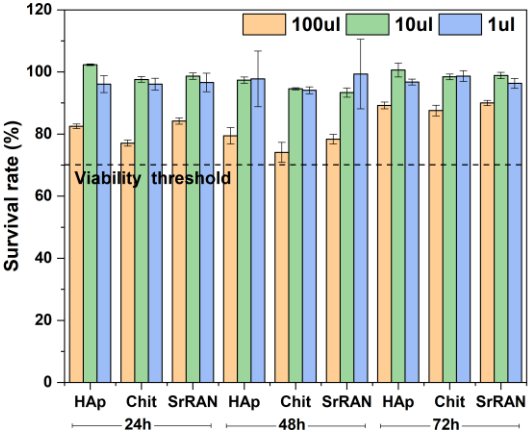

Figure 58 Cytotoxicity of HAp, HAp10Chit (Chit) and HAp10ChitSrRAN (SrRAN) extracts (in 1, 10 and 100% of concentration) after 24 h, 48 h and 72 h,

The alkaline phosphatase (ALP) activity of pre-osteoblasts at day 7 and day 14 is reported in Figure 59. Ordinary one-way ANOVA was performed as statistical data treatment followed by Tukey's multiple comparison test to find significant differences between the groups (HAp, HAp10Chit and HAp10ChitSrRAN), whereas Welch's test was used to compare the effect of the culture medium on the cell activity. All samples placed in the osteogenic medium showed a similar ALP activity both at day 7 and at day 14, comparable with the control, consisting in cells cultured directly on the tissue culture plate without any material substrate. Therefore, all cold sintered substrates induced potentially the cell osteogenic differentiation into osteoblasts. Interestingly, the cells activity on the HAp and HAp-based composites at day 7 was comparable to the control independently from the type of culture medium (osteogenic and non-osteogenic). At day 14 the ALP activity of cells in the non-osteogenic medium on HAp was statistically higher with respect to the composites, and comparable with the activity on the same substrate in the osteogenic medium.

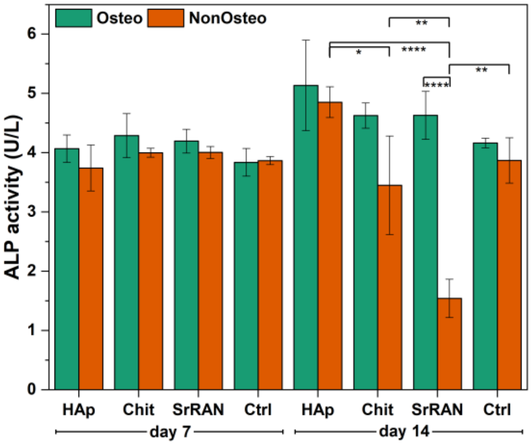

*Figure 59 ALP activity of MC3T3-E1 cells on HAp, HAp10Chit (Chit), and HAp10ChitSrRAN (SrRAN) at day 7 and day 14. Statistical difference for * $p<0.05$, ** $p<0.007$, **** $p<0.0001$.*

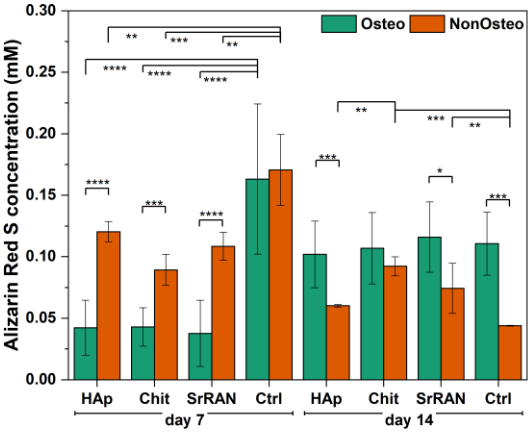

*Figure 60 Alizarin Red S staining results of MC3T3-E1 cells on cold sintered HAp and HAp10Chit (Chit), and HAp10ChitSrRAN (SrRAN) at day 7 and day 14. Statistical difference is * $p<0.05$, ** $p<0.01$, *** $p<0.001$ and **** $p<0.0001$.*

The differentiation potential of the substrates was further investigated by Alizarin Red S staining, as reported in Figure 60 and Figure 61, respectively. The amount of calcium deposition after 14 days was significantly higher in the cold sintered substrates immersed in the osteogenic medium with respect to the non-osteogenic one. Moreover, all groups in the osteogenic medium showed a level of mineralization at day 14 comparable with the control. Such findings were further confirmed by the optical micrographs in Figure 61, where some mineralization clusters can be observed. In all optical images, cells appeared elongated and spread already at day 7, while at day 14 cells organized in a dense network. After 14 days of culture, cells in contact with HAp10ChitSrRAN substrate did not show any adverse response to the drug, even considering the possible burst release. In light of such preliminary in vitro results, further in vitro investigation could be carried out in the future to evaluate how cold sintered substrate interact with mesenchymal stem cells and to optimize the SrRAN content to effectively enhance bone cell activities.

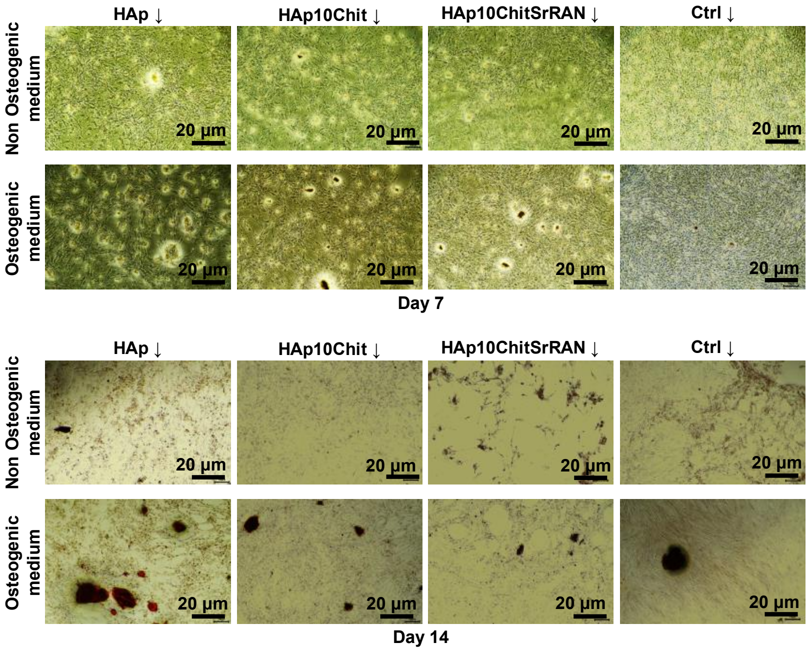

Figure 61 Optical micrographs of Alizarin Red S staining at day 7 and day 14.

5.4. Conclusions

The remarkable potential of cold sintering was further demonstrated in the present chapter. Indeed, cold sintered HAp and HAp/chitosan composite did not show any stress-induced transformation during the process even under as high pressure as 1.5 GPa, and the investigated mechanical properties were comparable and even superior to HAp and HAp-based composites processed by other sintering routes (solid state sintering, spark plasma sintering, etc). Nonetheless, drug-loaded cold sintered pellets did not report any modification to the active principle and a sustained and controlled release was ensured for at least 15 days. Although the limited porosity inhibits bone cell ingrowth and migration, the preliminary cellular studies revealed that cold sintered HAp and HAp/chitosan composite are potentially able to sustain osteogenic differentiation and induce extracellular mineralization after 14 days of culture in the osteogenic medium.

General conclusions and future perspectives

In the present thesis work, low temperature synthesis routes (i.e. mechanochemistry, dissolution-precipitation) and cold sintering processes were described and discussed for the transformation of biogenic calcium carbonate from mussel shells to a multi-ion substituted hydroxyapatite, resembling the chemical composition of bone apatite. Although cold sintering still faces some limitations in terms of produced shape and geometries able to mimic bone structure, cold sintered HAp and HAp-based composites consolidated up to 85-90 % relative density showed mechanical properties comparable to bone apatite as well as to HAp processed by other synthesis/sintering techniques. The peculiar features of cold sintering (i.e. low temperature) was crucial to preserve the nano-crystallinity, non-stoichiometry and surface reactivity which resulted in bone like apatite and are believed to be the responsible for the bioactivity and biological properties of the material. Nonetheless, the preliminary biological evaluation revealed that cold sintered HAp derived from mussel shells was cytocompatible, enhanced cell adhesion and spreading on the substrate in comparison to conventionally sintered stoichiometric HAp. The potential osteogenic differentiation and mineralization capability of HAp/chitosan composites were also pointed out.

Of course, this is not the end of the story.

With an eye on future works, both mechanochemistry and dissolution-precipitation synthesis should be further studied and optimized. Mechanochemistry is a simple and straightforward process, but it might lack of robustness and reproducibility due to uneven reagents mixing issues. On the contrary, high control over the reaction is ensured by dissolution-precipitation synthesis but further studies are required to broaden the opportunities such synthesis method offers, especially for the one-pot production of ceramic-based composites.

Cold sintering deserves further studies to fully understand the mechanisms leading to material densification. In the manuscript, we proposed pressure-solution creep and plastic deformation as main driving force for cold sintering, due to the peculiar processing conditions (i.e. low temperature, applied pressure, transient liquid-phase). In agreement, we played with the processing parameters to better understand how densification could occur and thus support our hypotheses. As described in Chapter IV, the highest density of nano-HAp produced by mechanochemistry could be obtained only with the synergistic contribution of liquid-phase, pressure and temperature. However, in Chapter V high densification of nano-HAp by dissolution-precipitation was achieved in absence of a liquid-phase and at room temperature. A possible explanation could be found in the different nano-HAp powders used in those studies, specifically in the different particle size and surface reactivity of the powder due to the surface hydrated layer. Both powders were nanocrystalline even if HAp by dissolution-precipitation was even finer than HAp by mechanosynthesis. The finer the particles, the higher the surface energy and reactivity. In addition, HAp by mechanochemistry was obtained after a drying step at 150°C overnight, whereas HAp by dissolution-precipitation was exposed to a maximum temperature of 45°C and freeze-dried. One could therefore expect a larger hydrated layer in HAp by dissolution-precipitation rather than in HAp by mechanochemistry. A larger hydrated layer could promote the formation of interparticles bridges leading to densification. As aforementioned in the manuscript, understanding the chemistry at the grain boundary could be the key to understand cold sintering mechanisms, and dedicated studies in this scenario should be carried out soon.

Cold sintering is still a new technique especially in the biomedical field. Up to date, cold sintered bodies are not suitable as scaffolds for bone tissue regeneration because the limited non-interconnected porosity negatively affects the possibility of cell migration and ingrowth. However, future studies are a demand to further explore the realization of coatings by cold sintering (possibly directly on metallic substrates) and/or to be able to produce a scaffold with a suitable interconnected porosity (possibly by using pore-forming agents without affecting the mechanical integrity of the scaffold itself).

Scientific activities and abroad experiences

Conferences

- EUROMAT2021 (Online, Sept. 13th-17th, 2021) – Oral presentation
- ScSB2022 (Jurmala, June 13th-15th , 2022) – Oral presentation
- Ceramics in Europe (Krakow, July 10th-14th 2022) – Oral presentation
- Bioceramics32 (Mestre, Sept. 20th-23rd 2022) – Oral presentation
- INSTM (Bressanone, Jan. 23rd-25th 2023) – Oral presentation

Workshops

- ACerS Winter Workshop 2022 (Online, Feb. 17th-18rd 2022)
- ACerS Winter Workshop 2023 (Daytona Beach, Jan. 20th-22nd 2023)

Schools

- Summer School Electric and Magnetic Field Processing of Inorganic Materials (Online, Sept. 14th-16th 2020)
- RISEUs2 Summer School (Toulouse, Mar. 21st-25th 2022)
- RISEUs2 Winter School (Jurmala, Aug. 23rd-25th 2022)
- RISEUs2 Summer School (Davos, Nov. 21st-25th 2022)

Abroad experiences

- Visiting PhD student at Baltic Biomaterial Centre of Excellence of Riga Technical University (Riga, Feb. 1st 2022-March 29th 2023)
- Visiting PhD student at National Polytechnic Institute of Toulouse (Toulouse, March 5th-25th 2023)

Publications

1. Cestari et al., Low-temperature synthesis of nanometric apatite from biogenic sources, Ceram. Int., **2020**
2. Cestari et al., Nano-Hydroxyapatite Derived from Biogenic and Bioinspired Calcium Carbonates: Synthesis and In Vitro Bioactivity, Nanomat., **2021**
3. Galotta A. et al., Cold sintering of diatomaceous earth, J. Am. Ceram. Soc., **2021**
4. Biesuz M. and Galotta A. et al., Speedy bioceramics: Rapid densification of tricalcium phosphate by ultrafast high-temperature sintering, Mat. Sci. Eng. C, **2021**
5. Galotta A. et al., The cold sintering process: A review on processing features, densification mechanisms and perspectives, J. Eur. Cer. Soc., **2021**
6. Santosh B. et al., Cold sintering of colloidal silica particles using different alkali solutions, Ceram. Int., **2022**
7. Galotta A. et al., Mechanochemical synthesis and cold sintering of mussel shell-derived hydroxyapatite nano-powders for bone tissue regeneration, J. Eur. Cer. Soc., **2022**
8. Galotta A. et al., Dissolution-precipitation synthesis and cold sintering of mussel shells-derived hydroxyapatite and hydroxyapatite/chitosan composites for bone tissue engineering, Open Ceramics, **2023**

References

[1] A. R. Amini, C. T. Laurencin, and S. P. Nukavarapu, "Bone Tissue Engineering: Recent Advances and Challenges," *Crit. Rev. Biomed. Eng.*, vol. 40, no. 5, pp. 363–408, 2012, doi: 10.1615/CritRevBiomedEng.v40.i5.10.

[2] C. A. Vacanti, "The history of tissue engineering," *J. Cell. Mol. Med.*, vol. 10, no. 3, pp. 569–576, Jul. 2006, doi: 10.1111/j.1582-4934.2006.tb00421.x.

[3] R. Langer and J. P. Vacanti, "Tissue Engineering," *Science (80-.).*, vol. 260, no. 5110, pp. 920–926, May 1993, doi: 10.1126/science.8493529.

[4] J. R. Perez, D. Kouroupis, D. J. Li, T. M. Best, L. Kaplan, and D. Correa, "Tissue Engineering and Cell-Based Therapies for Fractures and Bone Defects," *Front. Bioeng. Biotechnol.*, vol. 6, no. July, pp. 1–23, 2018, doi: 10.3389/fbioe.2018.00105.

[5] B. M. Manzini, L. M. R. Machado, P. Y. Noritomi, and J. V. L. da Silva, "Advances in Bone tissue engineering: A fundamental review," *J. Biosci.*, vol. 46, no. 1, p. 17, Dec. 2021, doi: 10.1007/s12038-020-00122-6.

[6] D. Lopes, C. Martins-Cruz, M. B. Oliveira, and J. F. Mano, "Bone physiology as inspiration for tissue regenerative therapies," *Biomaterials*, vol. 185, no. September, pp. 240–275, 2018, doi: 10.1016/j.biomaterials.2018.09.028.

[7] Allied Analytics LLP, "Bone Grafts and Substitutes Market by Type, Application, End-user: Global Opportunity Analysis and Industry Forecast, 2021-2031," 2023. doi: 5394240.

[8] P. Baldwin, D. J. Li, D. A. Auston, H. S. Mir, R. S. Yoon, and K. J. Koval, "Autograft, Allograft, and Bone Graft Substitutes: Clinical Evidence and Indications for Use in the Setting of Orthopaedic Trauma Surgery," *J. Orthop. Trauma*, vol. 33, no. 4, pp. 203–213, 2019, doi: 10.1097/BOT.0000000000001420.

[9] A. J. Salgado, O. P. Coutinho, and R. L. Reis, "Bone tissue engineering: State of the art and future trends," *Macromol. Biosci.*, vol. 4, no. 8, pp. 743–765, 2004, doi: 10.1002/mabi.200400026.

[10] S. T. Kao and D. D. Scott, "A Review of Bone Substitutes," *Oral Maxillofac. Surg. Clin. North Am.*, vol. 19, no. 4, pp. 513–521, 2007, doi: 10.1016/j.coms.2007.06.002.

[11] Y. Sawada *et al.*, “A novel hydroxyapatite ceramic bone substitute transformed by ostrich cancellous bone: Characterization and evaluations of bone regeneration activity,” *J. Biomed. Mater. Res. - Part B Appl. Biomater.*, vol. 98 B, no. 2, pp. 217–222, 2011, doi: 10.1002/jbm.b.31783.

[12] F. Mahyudin, D. N. Utomo, H. Suroto, T. W. Martanto, M. Edward, and I. L. Gaol, “Comparative Effectiveness of Bone Grafting Using Xenograft Freeze-Dried Cortical Bovine, Allograft Freeze-Dried Cortical New Zealand White Rabbit, Xenograft Hydroxyapatite Bovine, and Xenograft Demineralized Bone Matrix Bovine in Bone Defect of Femoral Di,” *Int. J. Biomater.*, vol. 2017, 2017, doi: 10.1155/2017/7571523.

[13] R. Amid, A. Kheiri, L. Kheiri, M. Kadkhodazadeh, and M. Ekhlasmandkermani, “Structural and chemical features of xenograft bone substitutes: A systematic review of in vitro studies,” *Biotechnol. Appl. Biochem.*, vol. 68, no. 6, pp. 1432–1452, 2021, doi: 10.1002/bab.2065.

[14] A. Mordenfeld, T. Albrektsson, and M. Hallman, “A 10-Year Clinical and Radiographic Study of Implants Placed after Maxillary Sinus Floor Augmentation with an 80:20 Mixture of Deproteinized Bovine Bone and Autogenous Bone,” *Clin. Implant Dent. Relat. Res.*, vol. 16, no. 3, pp. 435–446, 2014, doi: 10.1111/cid.12008.

[15] J. Hughes, “Xenografting: ethical issues,” *J. Med. Ethics*, vol. 24, no. 1, pp. 18–24, Feb. 1998, doi: 10.1136/jme.24.1.18.

[16] B. E. Rollin, “Ethical and societal issues occasioned by xenotransplantation,” *Animals*, vol. 10, no. 9, pp. 1–10, 2020, doi: 10.3390/ani10091695.

[17] M. Kaiser, “Xenotransplantation – Ethical Considerations based on Human and Societal Perspectives,” *Acta Vet. Scand.*, vol. 45, no. S65, pp. 65–73, 2004, doi: https://doi.org/10.1186/1751-0147-45-S1-S65.

[18] D. Offner *et al.*, “Bone Grafts, Bone Substitutes and Regenerative Medicine Acceptance for the Management of Bone Defects Among French Population: Issues about Ethics, Religion or Fear?,” *Cell Med.*, vol. 11, p. 215517901985766, 2019, doi: 10.1177/2155179019857661.

[19] A. Assari, M. Hani, H. Qaid, B. Omar, and L. Aleid, “Effect of religious beliefs on bone graft selection for oral and maxillofacial surgery in Saudi Arabia,” *J. Stomatol. Oral Maxillofac. Surg.*, vol. 123, no. 5, pp. e563–e568, 2022, doi: 10.1016/j.jormas.2022.01.014.

[20] R. Quarto and P. Giannoni, “Bone tissue engineering: Past-present-

future," *Methods Mol. Biol.*, vol. 1416, pp. 21–33, 2016, doi: 10.1007/978-1-4939-3584-0_2.

[21] R. Florencio-Silva, G. R. da S. Sasso, E. Sasso-Cerri, M. J. Simões, and P. S. Cerri, "Biology of Bone Tissue: Structure, Function, and Factors That Influence Bone Cells," *Biomed Res. Int.*, vol. 2015, no. 6, pp. 1–17, 2015, doi: 10.1155/2015/421746.

[22] J. A. Buckwalter, M. J. Glimcher, R. R. Cooper, and R. Recker, "Bone biology," *J. Bone Jt. Surg.*, vol. 77, no. 8, pp. 1256–1275, 1995.

[23] E. F. Morgan, G. U. Unnikrisnan, and A. I. Hussein, "Bone Mechanical Properties in Healthy and Diseased States," *Annu. Rev. Biomed. Eng.*, vol. 20, no. 1, pp. 119–143, Jun. 2018, doi: 10.1146/annurev-bioeng-062117-121139.

[24] H. Qu, H. Fu, Z. Han, and Y. Sun, "Biomaterials for bone tissue engineering scaffolds: A review," *RSC Adv.*, vol. 9, no. 45, pp. 26252–26262, 2019, doi: 10.1039/c9ra05214c.

[25] L. M. McNamara, "2.10 Bone as a Material," in *Comprehensive Biomaterials II*, vol. 2, no. August 2016, Elsevier, 2017, pp. 202–227.

[26] M. Meyers and P. Chen, "Calcium-phosphate-based composites," in *Biological Materials Science*, Cambridge University Press, 2014, pp. 223–291.

[27] A. Feldmann, P. Wili, G. Maquer, and P. Zysset, "The thermal conductivity of cortical and cancellous bone," *Eur. Cells Mater.*, vol. 35, no. 2000, pp. 25–33, Jan. 2018, doi: 10.22203/eCM.v035a03.

[28] W. Bonfield, M. Wang, and K. E. Tanner, "Interfaces in analogue biomaterials," *Acta Mater.*, vol. 46, no. 7, pp. 2509–2518, 1998, doi: 10.1016/S1359-6454(98)80035-9.

[29] N. Eliaz and N. Metoki, "Calcium Phosphate Bioceramics: A Review of Their History, Structure, Properties, Coating Technologies and Biomedical Applications," *Materials (Basel).*, vol. 10, pp. 1–104, 2017, doi: 10.3390/ma10040334.

[30] S. Bose, M. Roy, and A. Bandyopadhyay, "Recent advances in bone tissue engineering scaffolds," *Trends Biotechnol.*, vol. 30, no. 10, pp. 546–554, Oct. 2012, doi: 10.1016/j.tibtech.2012.07.005.

[31] X. Lin, S. Patil, Y.-G. Gao, and A. Qian, "The Bone Extracellular Matrix in Bone Formation and Regeneration," *Front. Pharmacol.*, vol. 11, no.

May, pp. 1–15, May 2020, doi: 10.3389/fphar.2020.00757.

[32] A. Ressler, A. Žužić, I. Ivanišević, N. Kamboj, and H. Ivanković, “Ionic substituted hydroxyapatite for bone regeneration applications: A review,” *Open Ceram.*, vol. 6, no. May, 2021, doi: 10.1016/j.oceram.2021.100122.

[33] E. Boanini, M. Gazzano, and A. Bigi, “Ionic substitutions in calcium phosphates synthesized at low temperature,” *Acta Biomater.*, vol. 6, no. 6, pp. 1882–1894, 2010, doi: 10.1016/j.actbio.2009.12.041.

[34] K. Ishikawa, “Bone substitute fabrication based on dissolution-precipitation reactions,” *Materials (Basel).*, vol. 3, no. 2, pp. 1138–1155, 2010, doi: 10.3390/ma3021138.

[35] A. A. Baig *et al.*, “Relationships among carbonated apatite solubility, crystallite size, and microstrain parameters,” *Calcif. Tissue Int.*, vol. 64, no. 5, pp. 437–449, 1999, doi: 10.1007/PL00005826.

[36] A. Rupani, L. A. Hidalgo-Bastida, F. Rutten, A. Dent, I. Turner, and S. Cartmell, “Osteoblast activity on carbonated hydroxyapatite,” *J. Biomed. Mater. Res. - Part A*, vol. 100 A, no. 4, pp. 1089–1096, 2012, doi: 10.1002/jbm.a.34037.

[37] E. Landi, G. Celotti, G. Logroscino, and A. Tampieri, “Carbonated hydroxyapatite as bone substitute,” *J. Eur. Ceram. Soc.*, vol. 23, no. 15, pp. 2931–2937, 2003, doi: 10.1016/S0955-2219(03)00304-2.

[38] J. P. Lafon, E. Champion, and D. Bernache-Assollant, “Processing of AB-type carbonated hydroxyapatite Ca10−x(PO4)6−x(CO3)x(OH)2−x−2y(CO3)y ceramics with controlled composition,” *J. Eur. Ceram. Soc.*, vol. 28, no. 1, pp. 139–147, Jan. 2008, doi: 10.1016/j.jeurceramsoc.2007.06.009.

[39] K. Ishikawa, “Carbonate Apatite Bone Replacement,” in *Handbook of Bioceramics and Biocomposites*, springer international publishing switzerland, 2016, pp. 1–1386.

[40] L. C. Chow and E. D. Eanes, “Solubility of Calcium Phosphates,” in *Octacalcium Phosphate (Monographs in Oral Science)*, vol. 18, 2001, pp. 94–111.

[41] M.-M. Germaini *et al.*, “Osteoblast and osteoclast responses to A/B type carbonate-substituted hydroxyapatite ceramics for bone regeneration,” *Biomed. Mater.*, vol. 12, no. 3, 2017, doi: 10.1088/1748-605X/aa69c3.

[42] T. A. Mahmood, K. De Groot, C. A. Van Blitterswijk, and F. Barre, "Advanced biomaterials for skeletal tissue regeneration : Instructive and smart functions," *Mater. Sci. Eng. R*, vol. 59, pp. 38–71, 2008, doi: 10.1016/j.mser.2007.12.001.

[43] D. F. Williams, "Tissue-biomaterial interactions," *J. Mater. Sci.*, vol. 22, pp. 3421–3445, 1987, doi: https://doi.org/10.1007/BF01161439.

[44] D. F. Williams, "On the nature of biomaterials," *Biomaterials*, vol. 30, no. 30, pp. 5897–5909, Oct. 2009, doi: 10.1016/j.biomaterials.2009.07.027.

[45] G. L. Koons, M. Diba, and A. G. Mikos, "Materials design for bone-tissue engineering," *Nat. Rev. Mater.*, vol. 5, no. 8, pp. 584–603, 2020, doi: 10.1038/s41578-020-0204-2.

[46] G. C. Wang, Z. F. Lu, and H. Zreiqat, "Bioceramics for skeletal bone regeneration," in *Bone Substitute Biomaterials*, Elsevier, 2014, pp. 180–216.

[47] S. Samavedi, A. R. Whittington, and A. S. Goldstein, "Calcium phosphate ceramics in bone tissue engineering: A review of properties and their influence on cell behavior," *Acta Biomater.*, vol. 9, no. 9, pp. 8037–8045, 2013, doi: 10.1016/j.actbio.2013.06.014.

[48] S. V Dorozhkin, "Current State of Bioceramics," *J. Ceram. Sci. Technol.*, vol. 09, no. December 2018, pp. 353–370, 2018, doi: 10.4416/JCST2018-00026.

[49] D. F. Williams, "On the mechanisms of biocompatibility," *Biomaterials*, vol. 29, pp. 2941–2953, 2008, doi: 10.1016/j.biomaterials.2008.04.023.

[50] T. Albrektsson and C. Johansson, "Osteoinduction, osteoconduction and osseointegration," *Eur. Spine J.*, vol. 10, pp. 96–101, 2001, doi: 10.1007/s005860100282.

[51] T. Kokubo and H. Takadama, "How useful is SBF in predicting in vivo bone bioactivity?," *Biomaterials*, vol. 27, no. 15, pp. 2907–2915, 2006, doi: 10.1016/j.biomaterials.2006.01.017.

[52] F. Baino and S. Yamaguchi, "The Use of Simulated Body Fluid (SBF) for Assessing Materials Bioactivity in the Context of Tissue Engineering: Review and Challenges," *Biomimetics*, vol. 5, pp. 1–19, Oct. 2020, doi: 10.3390/biomimetics5040057.

[53] T. Yamamuro, "Bioceramics," in *Biomechanics and Biomaterials in*

Orthopedics, London: Springer London, 2004, pp. 22–33.

[54] H. Gul, M. Khan, and A. S. Khan, “Bioceramics: types and clinical applications,” in *Handbook of Ionic Substituted Hydroxyapatites*, Elsevier, 2020, pp. 53–83.

[55] L. L. Hench, “Bioceramics: From Concept to Clinic,” *J. Am. Ceram. Soc.*, vol. 74, no. 7, pp. 1487–1510, Jul. 1991, doi: 10.1111/j.1151-2916.1991.tb07132.x.

[56] S. Bose and S. Tarafder, “Calcium phosphate ceramic systems in growth factor and drug delivery for bone tissue engineering: A review,” *Acta Biomater.*, vol. 8, no. 4, pp. 1401–1421, 2012, doi: 10.1016/j.actbio.2011.11.017.

[57] I. Denry and L. T. Kuhn, “Design and characterization of calcium phosphate ceramic scaffolds for bone tissue engineering,” *Dent. Mater.*, vol. 32, no. 1, pp. 43–53, 2016, doi: 10.1016/j.dental.2015.09.008.

[58] J. Jeong, J. H. Kim, J. H. Shim, N. S. Hwang, and C. Y. Heo, “Bioactive calcium phosphate materials and applications in bone regeneration,” *Biomater. Res.*, vol. 23, no. 1, p. 4, Dec. 2019, doi: 10.1186/s40824-018-0149-3.

[59] S. V Dorozhkin, “Calcium orthophosphates (CaPO4): occurrence and properties,” *Prog. Biomater.*, vol. 5, no. 1, pp. 9–70, Mar. 2016, doi: 10.1007/s40204-015-0045-z.

[60] O. Suzuki, “Octacalcium phosphate (OCP)-based bone substitute materials,” *Jpn. Dent. Sci. Rev.*, vol. 49, no. 2, pp. 58–71, May 2013, doi: 10.1016/j.jdsr.2013.01.001.

[61] S. E. Kim and K. Park, “Recent Advances of Biphasic Calcium Phosphate Bioceramics for Bone Tissue Regeneration,” in *Biomimicked Biomaterials Advances in Tissue Engineering and Regenerative Medicine*, vol. 1250, 2020, pp. 177–188.

[62] M. Kheradmandfard, K. Mahdavi, A. Zargar Kharazi, S. F. Kashani-Bozorg, and D.-E. Kim, “In vitro study of a novel multi-substituted hydroxyapatite nanopowder synthesized by an ultra-fast, efficient and green microwave-assisted method,” *Mater. Sci. Eng. C*, vol. 117, no. February, p. 111310, Dec. 2020, doi: 10.1016/j.msec.2020.111310.

[63] A. Ressler *et al.*, “Osteogenic differentiation of human mesenchymal stem cells on substituted calcium phosphate/chitosan composite scaffold,” *Carbohydr. Polym.*, vol. 277, no. August 2021, 2022, doi:

10.1016/j.carbpol.2021.118883.

[64] H. R. R. Ramay and M. Zhang, “Biphasic calcium phosphate nanocomposite porous scaffolds for load-bearing bone tissue engineering,” *Biomaterials*, vol. 25, no. 21, pp. 5171–5180, Sep. 2004, doi: 10.1016/j.biomaterials.2003.12.023.

[65] I. Puttini *et al.*, “Evaluation of Osteoconduction of Biphasic Calcium Phosphate Ceramic in the Calvaria of Rats: Microscopic and Histometric Analysis,” *J. Funct. Biomater.*, vol. 10, no. 1, p. 7, Jan. 2019, doi: 10.3390/jfb10010007.

[66] C. Combes and C. Rey, “Amorphous calcium phosphates: Synthesis, properties and uses in biomaterials,” *Acta Biomater.*, vol. 6, no. 9, pp. 3362–3378, 2010, doi: 10.1016/j.actbio.2010.02.017.

[67] A. L. Boskey, “Amorphous Calcium Phosphate: The Contention of Bone,” *J. Dent. Res.*, vol. 76, no. 8, pp. 1433–1436, Aug. 1997, doi: 10.1177/00220345970760080501.

[68] M. Edén, “Structure and formation of amorphous calcium phosphate and its role as surface layer of nanocrystalline apatite: Implications for bone mineralization,” *Materialia*, vol. 17, no. January, p. 101107, Jun. 2021, doi: 10.1016/j.mtla.2021.101107.

[69] A. Lotsari, A. K. Rajasekharan, M. Halvarsson, and M. Andersson, “Transformation of amorphous calcium phosphate to bone-like apatite,” *Nat. Commun.*, vol. 9, no. 1, p. 4170, Oct. 2018, doi: 10.1038/s41467-018-06570-x.

[70] E. D. Eanes, I. H. Gillessen, and A. S. Posner, “Intermediate States in the Precipitation of Hydroxyapatite,” *Nature*, vol. 208, no. 5008, pp. 365–367, Oct. 1965, doi: 10.1038/208365a0.

[71] E. D. Eanes, J. D. Termine, and A. S. Posner, “Amorphous Calcium Phosphate in Skeletal Tissues,” *Clin. Orthop. Relat. Res.*, vol. 53, no. 7, pp. 223–236, 1967.

[72] W. E. Brown, J. P. Smith, J. R. Lehr, and A. W. Frazier, “Octacalcium Phosphate and Hydroxyapatite: Crystallographic and Chemical Relations between Octacalcium Phosphate and Hydroxyapatite,” *Nature*, vol. 196, no. 4859, pp. 1050–1055, Dec. 1962, doi: 10.1038/1961050a0.

[73] W. E. Brown, “Crystal Growth of Bone Mineral,” *Clin. Orthop. Relat. Res.*, vol. 44, no. 1, pp. 205–220, Jan. 1966, doi: 10.1097/00003086-

196600440-00021.

[74] H. Imaizumi, M. Sakurai, O. Kashimoto, T. Kikawa, and O. Suzuki, “Comparative study on osteoconductivity by synthetic octacalcium phosphate and sintered hydroxyapatite in rabbit bone marrow,” *Calcif. Tissue Int.*, vol. 78, no. 1, pp. 45–54, 2006, doi: 10.1007/s00223-005-0170-0.

[75] J. Vecstaudza and J. Locs, “Novel preparation route of stable amorphous calcium phosphate nanoparticles with high specific surface area,” *J. Alloys Compd.*, vol. 700, pp. 215–222, 2017, doi: 10.1016/j.jallcom.2017.01.038.

[76] A. Ressler *et al.*, “From Bio-waste to Bone Substitute: Synthesis of Biomimetic Hydroxyapatite and Its Use in Chitosan-based Composite Scaffold Preparation,” *Chem. Biochem. Eng. Q.*, vol. 34, no. 2, pp. 59–71, 2020, doi: 10.15255/CABEQ.2020.1783.

[77] G. Gergely *et al.*, “Nano-hydroxyapatite preparation from biogenic raw materials,” *Cent. Eur. J. Chem.*, vol. 8, no. 2, pp. 375–381, 2010, doi: 10.2478/s11532-010-0004-4.

[78] A. C. Ferro and M. Guedes, “Mechanochemical synthesis of hydroxyapatite using cuttlefish bone and chicken eggshell as calcium precursors,” *Mater. Sci. Eng. C*, vol. 97, no. December 2018, pp. 124–140, 2019, doi: 10.1016/j.msec.2018.11.083.

[79] T. Laonapakul, “Synthesis of hydroxyapatite from biogenic wastes,” *KKU Eng. J.*, vol. 42, no. September, pp. 269–275, 2015, doi: 10.14456/kkuenj.2015.30.

[80] N. A. S. Mohd Pu’ad, P. Koshy, H. Z. Abdullah, M. I. Idris, and T. C. Lee, “Syntheses of hydroxyapatite from natural sources,” *Heliyon*, vol. 5, no. 5, p. e01588, 2019, doi: 10.1016/j.heliyon.2019.e01588.

[81] C. Piccirillo, R. C. Pullar, E. Costa, A. Santos-Silva, M. M. E. Pintado, and P. M. L. Castro, “Hydroxyapatite-based materials of marine origin: A bioactivity and sintering study,” *Mater. Sci. Eng. C*, vol. 51, pp. 309–315, 2015, doi: 10.1016/j.msec.2015.03.020.

[82] M. Boutinguiza, J. Pou, R. Comesaña, F. Lusquiños, A. De Carlos, and B. León, “Biological hydroxyapatite obtained from fish bones,” *Mater. Sci. Eng. C*, vol. 32, no. 3, pp. 478–486, 2012, doi: 10.1016/j.msec.2011.11.021.

[83] J. K. Odusote, Y. Danyuo, A. D. Baruwa, and A. A. Azeez, “Synthesis and

characterization of hydroxyapatite from bovine bone for production of dental implants," *J. Appl. Biomater. Funct. Mater.*, vol. 17, no. 2, 2019, doi: 10.1177/2280800019836829.

[84] E. A. Ofudje, A. Rajendran, A. I. Adeogun, M. A. Idowu, S. O. Kareem, and D. K. Pattanayak, "Synthesis of organic derived hydroxyapatite scaffold from pig bone waste for tissue engineering applications," *Adv. Powder Technol.*, vol. 29, no. 1, pp. 1–8, 2018, doi: 10.1016/j.apt.2017.09.008.

[85] A. Singh, "Hydroxyapatite, a biomaterial: Its chemical synthesis, characterization and study of biocompatibility prepared from shell of garden snail, Helix aspersa," *Bull. Mater. Sci.*, vol. 35, no. 6, pp. 1031–1038, 2012, doi: 10.1007/s12034-012-0384-5.

[86] T. Laonapakul, R. Sutthi, P. Chaikool, S. Talangkun, A. Boonma, and P. Chindaprasirt, "Calcium phosphate powders synthesized from CaCO3 and CaO of natural origin using mechanical activation in different media combined with solid-state interaction," *Mater. Sci. Eng. C*, vol. 118, no. January 2018, p. 111333, 2021, doi: 10.1016/j.msec.2020.111333.

[87] K. S. Vecchio, X. Zhang, J. B. Massie, M. Wang, and C. W. Kim, "Conversion of bulk seashells to biocompatible hydroxyapatite for bone implants," *Acta Biomater.*, vol. 3, no. 6, pp. 910–918, 2007, doi: 10.1016/j.actbio.2007.06.003.

[88] J. P. Morris, T. Backeljau, and G. Chapelle, "Shells from aquaculture: a valuable biomaterial, not a nuisance waste product," *Rev. Aquac.*, vol. 11, no. 1, pp. 42–57, 2019, doi: 10.1111/raq.12225.

[89] A. Hart, "Mini-review of waste shell-derived materials' applications," *Waste Manag. Res.*, vol. 38, no. 5, pp. 514–527, 2020, doi: 10.1177/0734242X19897812.

[90] M. Jović, M. Mandić, M. Š. Ivanović, and I. Smičiklas, "Recent trends in application of shell waste from mariculture," *Stud. Mar.*, vol. 32, no. 1, pp. 47–62, 2019, doi: 10.5281/zenodo.3274471.

[91] Yan Ning and Chen Xi, "Sustainability: Don't waste seafood waste," *Nature*, vol. 524, pp. 155–157, 2015, doi: https://doi.org/10.1038/524155a.

[92] D. Qin *et al.*, "Development and application of fish scale wastes as versatile natural biomaterials," *Chem. Eng. J.*, vol. 428, no. April 2021, p. 131102, 2022, doi: 10.1016/j.cej.2021.131102.

[93] W. Pon-On, P. Suntornsaratoon, N. Charoenphandhu, J.

Thongbunchoo, N. Krishnamra, and I. M. Tang, “Hydroxyapatite from fish scale for potential use as bone scaffold or regenerative material,” *Mater. Sci. Eng. C*, vol. 62, pp. 183–189, 2016, doi: 10.1016/j.msec.2016.01.051.

[94] K. Gautam *et al.*, “Production of biopolymers from food waste: Constrains and perspectives,” *Bioresour. Technol.*, vol. 361, no. June, p. 127650, 2022, doi: 10.1016/j.biortech.2022.127650.

[95] N. Nuamsrinuan, W. Kaewwiset, P. Limsuwan, and K. Naemchanthara, “Hydroxyapatite Synthesized from Waste Eggshell via Ball Milling,” *Appl. Mech. Mater.*, vol. 866, no. June, pp. 12–16, 2017, doi: 10.4028/www.scientific.net/amm.866.12.

[96] M. Akram, R. Ahmed, I. Shakir, W. A. W. Ibrahim, and R. Hussain, “Extracting hydroxyapatite and its precursors from natural resources,” *J. Mater. Sci.*, vol. 49, no. 4, pp. 1461–1475, 2014, doi: 10.1007/s10853-013-7864-x.

[97] W. Linhart *et al.*, “Biologically and chemically optimized composites of carbonated apatite and polyglycolide as bone substitution materials,” *J. Biomed. Mater. Res.*, vol. 54, no. 2, pp. 162–171, 2001, doi: 10.1002/1097-4636(200102)54:2<162::AID-JBM2>3.0.CO;2-3.

[98] K. Lin *et al.*, “Biomimetic hydroxyapatite porous microspheres with co-substituted essential trace elements: Surfactant-free hydrothermal synthesis, enhanced degradation and drug release,” *J. Mater. Chem.*, vol. 21, no. 41, pp. 16558–16565, 2011, doi: 10.1039/c1jm12514a.

[99] Z. Chen, W. Zhang, M. Wang, L. J. Backman, and J. Chen, “Effects of Zinc, Magnesium, and Iron Ions on Bone Tissue Engineering,” *ACS Biomater. Sci. Eng.*, vol. 8, no. 6, pp. 2321–2335, 2022, doi: 10.1021/acsbiomaterials.2c00368.

[100] Ż. Ciosek, K. Kot, D. Kosik-Bogacka, N. Łanocha-Arendarczyk, and I. Rotter, “The effects of calcium, magnesium, phosphorus, fluoride, and lead on bone tissue,” *Biomolecules*, vol. 11, no. 4, 2021, doi: 10.3390/biom11040506.

[101] S. Bose, S. Tarafder, and A. Bandyopadhyay, “Effect of Chemistry on Osteogenesis and Angiogenesis Towards Bone Tissue Engineering Using 3D Printed Scaffolds,” *Ann. Biomed. Eng.*, vol. 45, no. 1, pp. 261–272, 2017, doi: 10.1007/s10439-016-1646-y.

[102] M. Yamaguchi, H. Oishi, and Y. Suketa, “Stimulatory effect of zinc on bone formation in tissue culture,” *Biochem. Pharmacol.*, vol. 36, no. 22,

pp. 4007–4012, 1987, doi: 10.1016/0006-2952(87)90471-0.

[103] K. Lin *et al.*, "Strontium substituted hydroxyapatite porous microspheres: Surfactant-free hydrothermal synthesis, enhanced biological response and sustained drug release," *Chem. Eng. J.*, vol. 222, pp. 49–59, 2013, doi: 10.1016/j.cej.2013.02.037.

[104] F. Yang, D. Yang, J. Tu, Q. Zheng, L. Cai, and L. Wang, "Strontium enhances osteogenic differentiation of mesenchymal stem cells and in vivo bone formation by activating Wnt/catenin signaling," *Stem Cells*, vol. 29, no. 6, pp. 981–991, 2011, doi: 10.1002/stem.646.

[105] Z. Saidak and P. J. Marie, "Strontium signaling: Molecular mechanisms and therapeutic implications in osteoporosis," *Pharmacol. Ther.*, vol. 136, no. 2, pp. 216–226, 2012, doi: 10.1016/j.pharmthera.2012.07.009.

[106] S. Ranganathan, S. Dutta, J. A. Moses, and C. Anandharamakrishnan, "Utilization of food waste streams for the production of biopolymers," *Heliyon*, vol. 6, no. 9, p. e04891, 2020, doi: 10.1016/j.heliyon.2020.e04891.

[107] E. Lizundia, F. Luzi, and D. Puglia, "Organic waste valorisation towards circular and sustainable biocomposites," *Green Chem.*, vol. 24, no. 14, pp. 5429–5459, 2022, doi: 10.1039/d2gc01668k.

[108] S. Sathiyavimal, S. Vasantharaj, F. LewisOscar, R. Selvaraj, K. Brindhadevi, and A. Pugazhendhi, "Natural organic and inorganic–hydroxyapatite biopolymer composite for biomedical applications," *Prog. Org. Coatings*, vol. 147, no. July, p. 105858, 2020, doi: 10.1016/j.porgcoat.2020.105858.

[109] S. Pramanik, S. Kharche, N. More, and D. Ranglani, "Natural Biopolymers for Bone Tissue Engineering : A Brief Review," *Eng. Regen.*, vol. 4, no. 2, pp. 193–204, 2023, doi: 10.1016/j.engreg.2022.12.002.

[110] N. Flòrez-Fernàndez, H. Domínguez, and M. D. Torres, "A green approach for alginate extraction from Sargassum muticum brown seaweed using ultrasound-assisted technique," *Int. J. Biol. Macromol.*, vol. 124, pp. 451–459, 2019, doi: 10.1016/j.ijbiomac.2018.11.232.

[111] M. Jang, B. Kong, Y. Jeong, C. H. Lee, and J. Nah, "Physicochemical Characterization of α-Chitin, β-Chitin, and γ-Chitin Separated from Natural Resources," *J. Polym. Sci. Part A Polym. Chem.*, vol. 42, no. 14, pp. 3423–3432, 2004, doi: 10.1002/pola.20176.

[112] J. A. Vázquez, I. Rodríguez-Amado, M. I. Montemayor, J. Fraguas, M. P.

Del González, and M. A. Murado, "Chondroitin sulfate, hyaluronic acid and chitin/chitosan production using marine waste sources: Characteristics, applications and eco-friendly processes: A review," *Mar. Drugs*, vol. 11, no. 3, pp. 747–774, 2013, doi: 10.3390/md11030747.

[113] T. H. Silva, J. Moreira-Silva, A. L. P. Marques, A. Domingues, Y. Bayon, and R. L. Reis, "Marine Origin Collagens and Its Potential Applications," *Mar. Drugs*, vol. 12, pp. 5881–5901, 2014, doi: 10.3390/md12125881.

[114] A. M. E. Matinong, Y. Chisti, K. L. Pickering, and R. G. Haverkamp, "Collagen Extraction from Animal Skin," *Biology (Basel).*, vol. 11, no. 905, pp. 1–15, 2022, doi: https:// doi.org/10.3390/biology11060905.

[115] L. C. Lv, Q. Y. Huang, W. Ding, X. H. Xiao, H. Y. Zhang, and L. X. Xiong, "Fish gelatin: The novel potential applications," *J. Funct. Foods*, vol. 63, no. January, 2019, doi: 10.1016/j.jff.2019.103581.

[116] D. Zhang, X. Wu, J. Chen, and K. Lin, "Bioactive Materials The development of collagen based composite scaffolds for bone regeneration," *Bioact. Mater.*, vol. 3, no. 1, pp. 129–138, 2018, doi: 10.1016/j.bioactmat.2017.08.004.

[117] Z. Li, T. Du, C. Ruan, and X. Niu, "Bioinspired mineralized collagen scaffolds for bone tissue engineering," *Bioact. Mater.*, vol. 6, no. 5, pp. 1491–1511, 2021, doi: 10.1016/j.bioactmat.2020.11.004.

[118] N. Davidenko *et al.*, "Evaluation of cell binding to collagen and gelatin: a study of the effect of 2D and 3D architecture and surface chemistry," *J. Mater. Sci. Mater. Med.*, vol. 27, no. 10, 2016, doi: 10.1007/s10856-016-5763-9.

[119] F. Xing *et al.*, "Hyaluronic acid as a bioactive component for bone tissue regeneration: Fabrication, modification, properties, and biological functions," *Nanotechnol. Rev.*, vol. 9, no. 1, pp. 1059–1079, 2020, doi: 10.1515/ntrev-2020-0084.

[120] FAO, "The State of World Fisheries and Aquaculture 2022. Towardsa Blue Transformation," FAO, Rome, Jun. 2022. doi: 10.4060/cc0463en.

[121] J. Engel, "Formation of Mollusk Shells," in *SpringerBriefs in Applied Sciences and Technology*, no. 9783319477107, 2017, pp. 29–40.

[122] D. E. Jacob, A. L. Soldati, R. Wirth, J. Huth, U. Wehrmeister, and W. Hofmeister, "Nanostructure, composition and mechanisms of bivalve shell growth," *Geochim. Cosmochim. Acta*, vol. 72, no. 22, pp. 5401–5415,

2008, doi: 10.1016/j.gca.2008.08.019.

[123] J. D. Birchall and N. L. Thomas, “On the architecture and function of cuttlefish bone,” *J. Mater. Sci.*, vol. 18, no. 7, pp. 2081–2086, 1983, doi: 10.1007/BF00555001.

[124] R. A. Hewitt, “Analysis of aragonite from the cuttlebone of Sepia officinalis L.,” *Mar. Geol.*, vol. 18, no. 1, pp. 1–5, 1975, doi: 10.1016/0025-3227(75)90033-X.

[125] V. Santás-Miguel, C. Campillo-Cora, A. Núñez-Delgado, D. Fernández-Calviño, and M. Arias-Estévez, “Utilization of mussel shell to remediate soils polluted with heavy metals,” *Biomass-Derived Mater. Environ. Appl.*, pp. 221–242, Jan. 2022, doi: 10.1016/B978-0-323-91914-2.00017-9.

[126] C. C. Vaughn and T. J. Hoellein, “Bivalve impacts in freshwater and marine ecosystems,” *Annu. Rev. Ecol. Evol. Syst.*, vol. 49, no. July, pp. 183–208, 2018, doi: 10.1146/annurev-ecolsys-110617-062703.

[127] V. R. Bellotto and N. Miekeley, “Improvements in calibration procedures for the quantitative determination of trace elements in carbonate material (mussel shells) by laser ablation ICP-MS,” *Fresenius. J. Anal. Chem.*, vol. 367, no. 7, pp. 635–640, 2000, doi: 10.1007/s002160000421.

[128] S. Scialla *et al.*, “Mussel Shell-Derived Macroporous 3D Sca ff old : Characterization and Optimization Study of a Bioceramic from the Circular Economy,” *Mar. Drugs*, vol. 18, no. 309, pp. 1–15, 2020.

[129] J. H. Shariffuddin, M. I. Jones, and D. A. Patterson, “Greener photocatalysts: Hydroxyapatite derived from waste mussel shells for the photocatalytic degradation of a model azo dye wastewater,” *Chem. Eng. Res. Des.*, vol. 91, no. 9, pp. 1693–1704, 2013, doi: 10.1016/j.cherd.2013.04.018.

[130] J. H. E. Cartwright, A. G. Checa, B. Escribano, and C. I. Sainz-Díaz, “Spiral and target patterns in bivalve nacre manifest a natural excitable medium from layer growth of a biological liquid crystal,” *Proc. Natl. Acad. Sci.*, vol. 106, no. 26, pp. 10499–10504, Jun. 2009, doi: 10.1073/pnas.0900867106.

[131] J. Sun and B. Bhushan, “Hierarchical structure and mechanical properties of nacre: a review,” *RSC Adv.*, vol. 2, pp. 7617–7632, 2012, doi: 10.1039/c2ra20218b.

[132] M. I. Jones, H. Barakat, and D. A. Patterson, “Production of

hydroxyapatite from waste mussel shells," *IOP Conf. Ser. Mater. Sci. Eng.*, vol. 18, no. SYMPOSIUM 13, pp. 17–21, 2011, doi: 10.1088/1757-899X/18/19/192002.

[133] M. Sari, P. Hening, Chotimah, I. D. Ana, and Y. Yusuf, "Bioceramic hydroxyapatite-based scaffold with a porous structure using honeycomb as a natural polymeric Porogen for bone tissue engineering," *Biomater. Res.*, vol. 25, no. 2, pp. 1–13, 2021, doi: 10.1186/s40824-021-00203-z.

[134] I. J. Macha, L. S. Ozyegin, J. Chou, R. Samur, F. N. Oktar, and B. Ben-Nissan, "An alternative synthesis method for di calcium phosphate (monetite) powders from mediterranean mussel (mytilus galloprovincialis) shells," *J. Aust. Ceram. Soc.*, vol. 49, no. 2, pp. 122–128, 2013.

[135] A. Shavandi, A. E. D. A. Bekhit, A. Ali, and Z. Sun, "Synthesis of nano-hydroxyapatite (nHA) from waste mussel shells using a rapid microwave method," *Mater. Chem. Phys.*, vol. 149–150, pp. 607–616, 2015, doi: 10.1016/j.matchemphys.2014.11.016.

[136] G. T. El-Bassyouni, S. S. Eldera, S. H. Kenawy, and E. M. A. Hamzawy, "Hydroxyapatite nanoparticles derived from mussel shells for in vitro cytotoxicity test and cell viability," *Heliyon*, vol. 6, no. 6, p. e04085, 2020, doi: 10.1016/j.heliyon.2020.e04085.

[137] P. Agalya *et al.*, "Hydroxyapatite-based antibacterial bio-nanomaterials: an insight into the synthesis using mussel shell as a calcium source, physicochemical properties, and nanoindentation characteristics," *Appl. Phys. A Mater. Sci. Process.*, vol. 127, no. 8, 2021, doi: 10.1007/s00339-021-04739-8.

[138] C. P. Jiménez-Gómez and J. A. Cecilia, "Chitosan: A Natural Biopolymer with a Wide and Varied Range of Applications," *Molecules*, vol. 25, no. 17, 2020, doi: 10.3390/molecules25173981.

[139] M. Minhajul Islam, M. Shahruzzaman, S. Biswas, M. Nurus Sakib, and T. Ur Rashid, "Chitosan based bioactive materials in tissue engineering applications-A review," *Bioact. Mater.*, vol. 5, no. October 2019, pp. 164–183, 2020, doi: 10.1016/j.bioactmat.2020.01.012.

[140] L. Pighinelli and M. Kucharska, "Chitosan – hydroxyapatite composites," *Carbohydr. Polym.*, vol. 93, no. 1, pp. 256–262, 2013, doi: 10.1016/j.carbpol.2012.06.004.

[141] Y. P. Guo, J. J. Guan, J. Yang, Y. Wang, C. Q. Zhang, and Q. F. Ke,

"Hybrid nanostructured hydroxyapatite-chitosan composite scaffold: Bioinspired fabrication, mechanical properties and biological properties," *J. Mater. Chem. B*, vol. 3, no. 23, pp. 4679–4689, 2015, doi: 10.1039/c5tb00175g.

[142] M. Matinfar, A. S. Mesgar, and Z. Mohammadi, "Evaluation of physicochemical, mechanical and biological properties of chitosan/carboxymethyl cellulose reinforced with multiphasic calcium phosphate whisker-like fibers for bone tissue engineering," *Mater. Sci. Eng. C*, vol. 100, no. February, pp. 341–353, 2019, doi: 10.1016/j.msec.2019.03.015.

[143] M. N. Rahaman, *Ceramic processing and sintering*, II edition. Marcel Dekker, Inc., 2016.

[144] C. Barry Carter and M. Grant Norton, *Ceramic Materials- Science and Engineering*, II edition. Springer, 2013.

[145] C. Xu, S. De, A. M. Balu, M. Ojeda, and R. Luque, "Mechanochemical synthesis of advanced nanomaterials for catalytic applications," *Chem. Commun.*, vol. 51, no. 31, pp. 6698–6713, 2015, doi: 10.1039/c4cc09876e.

[146] K. C. B. Yeong, J. Wang, and S. C. Ng, "Mechanochemical synthesis of nanocrystalline hydroxyapatite from CaO and $CaHPO_4$," *Biomaterials*, vol. 22, no. 20, pp. 2705–2712, 2001, doi: 10.1016/S0142-9612(00)00257-X.

[147] S. Lala, B. Satpati, T. Kar, and S. K. Pradhan, "Structural and microstructural characterizations of nanocrystalline hydroxyapatite synthesized by mechanical alloying," *Mater. Sci. Eng. C*, vol. 33, no. 5, pp. 2891–2898, 2013, doi: 10.1016/j.msec.2013.03.015.

[148] B. Nasiri-Tabrizi, P. Honarmandi, R. Ebrahimi-kahrizsangi, and P. Honarmandi, "Synthesis of nanosize single-crystal hydroxyapatite via mechanochemical method," *Mater. Lett.*, vol. 63, no. 5, pp. 543–546, 2009, doi: 10.1016/j.matlet.2008.11.030.

[149] A. A. Hamidi, M. N. Salimi, and A. H. M. Yusoff, "Synthesis and characterization of eggshell-derived hydroxyapatite via mechanochemical method: A comparative study," *AIP Conf. Proc.*, vol. 1835, 2017, doi: 10.1063/1.4981867.

[150] S. C. Wu, H. C. Hsu, Y. N. Wu, and W. F. Ho, "Hydroxyapatite synthesized from oyster shell powders by ball milling and heat treatment," *Mater. Charact.*, vol. 62, no. 12, pp. 1180–1187, 2011, doi: 10.1016/j.matchar.2011.09.009.

[151] C. C. Silva, A. G. Pinheiro, M. A. R. Miranda, J. C. Góes, and A. S. B. Sombra, “Structural properties of hydroxyapatite obtained by mechanosynthesis,” *Solid State Sci.*, vol. 5, no. 4, pp. 553–558, 2003, doi: 10.1016/S1293-2558(03)00035-9.

[152] T. Tsuzuki and P. G. McCormick, “Mechanochemical synthesis of nanoparticles,” *J. Mater. Sci.*, vol. 39, no. 16–17, pp. 5143–5146, 2004, doi: 10.1023/B:JMSC.0000039199.56155.f9.

[153] T. Mandal, B. K. Mishra, A. Garg, and D. Chaira, “Optimization of milling parameters for the mechanosynthesis of nanocrystalline hydroxyapatite,” *Powder Technol.*, vol. 253, pp. 650–656, 2014, doi: 10.1016/j.powtec.2013.12.026.

[154] B. Nasiri-Tabrizi, A. Fahami, and R. Ebrahimi-Kahrizsangi, “Effect of milling parameters on the formation of nanocrystalline hydroxyapatite using different raw materials,” *Ceram. Int.*, vol. 39, no. 5, pp. 5751–5763, 2013, doi: 10.1016/j.ceramint.2012.12.093.

[155] A. Pal *et al.*, “Mechanochemical synthesis of nanocrystalline hydroxyapatite from Mercenaria clam shells and phosphoric acid,” *Biomed. Phys. Eng. Express*, vol. 3, no. 1, p. 015010, 2017, doi: 10.1088/2057-1976/aa54f5.

[156] J. Pena, R. P. del Real, L. M. Rodriguez-Lorenzo, and M. Vallet-Regi, “Mechanochemistry: a new route for the preparation of carbonateapatite,” *Bioceramics*, vol. 12, no. October, pp. 149–152, 1999.

[157] A. Fahami, B. Nasiri-Tabrizi, and R. Ebrahimi-Kahrizsangi, “Synthesis of calcium phosphate-based composite nanopowders by mechanochemical process and subsequent thermal treatment,” *Ceram. Int.*, vol. 38, no. 8, pp. 6729–6738, 2012, doi: 10.1016/j.ceramint.2012.05.064.

[158] A. Kumar *et al.*, “Solid-State Reaction Synthesis of Nanoscale Materials: Strategies and Applications,” *Chem. Rev.*, vol. 122, no. 15, pp. 12748–12863, 2022, doi: 10.1021/acs.chemrev.1c00637.

[159] M. Sadat-Shojai, M. T. Khorasani, E. Dinpanah-Khoshdargi, and A. Jamshidi, “Synthesis methods for nanosized hydroxyapatite with diverse structures,” *Acta Biomater.*, vol. 9, no. 8, pp. 7591–7621, 2013, doi: 10.1016/j.actbio.2013.04.012.

[160] M. Lakrat, H. Jodati, E. M. Mejdoubi, and Z. Evis, “Synthesis and characterization of pure and Mg, Cu, Ag, and Sr doped calcium-deficient hydroxyapatite from brushite as precursor using the

dissolution-precipitation method," *Powder Technol.*, vol. 413, no. October 2022, p. 118026, 2023, doi: 10.1016/j.powtec.2022.118026.

[161] A. Ashokan, V. Rajendran, T. S. Sampath Kumar, and G. Jayaraman, "Eggshell derived hydroxyapatite microspheres for chromatographic applications by a novel dissolution - precipitation method," *Ceram. Int.*, vol. 47, no. 13, pp. 18575–18583, 2021, doi: 10.1016/j.ceramint.2021.03.183.

[162] K. Benataya, M. Lakrat, L. L. Elansari, and E. Mejdoubi, "Synthesis of B-type carbonated hydroxyapatite by a new dissolution-precipitation method," *Mater. Today Proc.*, vol. 31, pp. S83–S88, 2020, doi: 10.1016/j.matpr.2020.06.100.

[163] A. Kizalaite *et al.*, "Dissolution-precipitation synthesis and characterization of zinc whitlockite with variable metal content," *ACS Biomater. Sci. Eng.*, vol. 7, no. 8, pp. 3586–3593, 2021, doi: 10.1021/acsbiomaterials.1c00335.

[164] J. S. Reed, *Principles of ceramics and processing*, II edition. John Wiley and Sons, 1995.

[165] M. Biesuz, S. Grasso, and V. M. Sglavo, "What's new in ceramics sintering? A short report on the latest trends and future prospects," *Curr. Opin. Solid State Mater. Sci.*, vol. 24, no. 5, p. 100868, 2020, doi: 10.1016/j.cossms.2020.100868.

[166] E. A. Olevsky and D. V. Dudina, *Field-Assisted Sintering Science and Applications*. Springer, 2018.

[167] S. Grasso *et al.*, "A review of cold sintering processes," *Adv. Appl. Ceram.*, vol. 119, no. 3, pp. 115–143, Apr. 2020, doi: 10.1080/17436753.2019.1706825.

[168] C. Vakifahmetoglu and L. Karacasulu, "Cold sintering of ceramics and glasses: A review," *Curr. Opin. Solid State Mater. Sci.*, vol. 24, no. 100807, 2020, doi: 10.1016/j.cossms.2020.100807.

[169] M. Bram *et al.*, "Application of Electric Current-Assisted Sintering Techniques for the Processing of Advanced Materials," *Adv. Eng. Mater.*, vol. 22, no. 6, p. 2000051, Jun. 2020, doi: 10.1002/adem.202000051.

[170] M. Kermani *et al.*, "Flash cold sintering: Combining water and electricity," *J. Eur. Ceram. Soc.*, vol. 40, no. 15, pp. 6266–6271, 2020, doi: 10.1016/j.jeurceramsoc.2020.06.051.

[171] J. Guo, S. S. Berbano, H. Guo, A. L. Baker, M. T. Lanagan, and C. A. Randall, "Cold Sintering Process of Composites : Bridging the Processing Temperature Gap of Ceramic and Polymer Materials," pp. 7115–7121, 2016, doi: 10.1002/adfm.201602489.

[172] J. Guo, A. L. Baker, H. Guo, M. Lanagan, and C. A. Randall, "Cold sintering process: A new era for ceramic packaging and microwave device development," *J. Am. Ceram. Soc.*, vol. 100, no. 2, pp. 669–677, Feb. 2017, doi: 10.1111/jace.14603.

[173] H. Guo, A. Baker, J. Guo, and C. A. Randall, "Protocol for Ultralow-Temperature Ceramic Sintering: An Integration of Nanotechnology and the Cold Sintering Process," *ACS Nano*, vol. 10, no. 11, pp. 10606–10614, Nov. 2016, doi: 10.1021/acsnano.6b03800.

[174] C. A. Randall, J. Guo, A. Baker, M. Lanagan, and H. Guo, "Cold sintering ceramics and composites," 2017.

[175] E. Y. Gutmanas, A. Rabinkin, and M. Roitberg, "Cold sintering under high pressure," *Scr. Metall.*, vol. 13, no. 1, pp. 11–15, Jan. 1979, doi: 10.1016/0036-9748(79)90380-6.

[176] E. Y. Gutmanas, "High-pressure compaction and cold sintering of stainless steel powders," *Powder Metall. Int.*, vol. 12, no. 4, pp. 178–182, 1980.

[177] F. Bouville and A. R. Studart, "Geologically-inspired strong bulk ceramics made with water at room temperature," *Nat. Commun.*, vol. 8, no. 1, p. 14655, Mar. 2017, doi: 10.1038/ncomms14655.

[178] M. Haug, F. Bouville, C. Ruiz-Agudo, J. Avaro, D. Gebauer, and A. R. Studart, "Cold densification and sintering of nanovaterite by pressing with water," *J. Eur. Ceram. Soc.*, vol. 40, no. 3, pp. 893–900, 2020, doi: 10.1016/j.jeurceramsoc.2019.10.034.

[179] A. Ndayishimiye *et al.*, "Roadmap for densification in cold sintering: Chemical pathways," *Open Ceram.*, vol. 2, no. July, p. 100019, 2020, doi: 10.1016/j.oceram.2020.100019.

[180] J. Guo *et al.*, "Cold Sintering : Progress , Challenges , and Future Opportunities," *Annu. Rev. Mater. Res.*, vol. 49, pp. 275–295, 2019, doi: 10.1146/annurev-matsci-070218- 010041.

[181] C. Vakifahmetoglu and L. Karacasulu, "Cold sintering of ceramics and glasses: A review," *Curr. Opin. Solid State Mater. Sci.*, vol. 24, no. 1, p. 100807, Feb. 2020, doi: 10.1016/j.cossms.2020.100807.

[182] A. Galotta and V. M. Sglavo, “The cold sintering process: A review on processing features, densification mechanisms and perspectives,” *J. Eur. Ceram. Soc.*, vol. 41, no. 16, pp. 1–17, 2021, doi: 10.1016/j.jeurceramsoc.2021.09.024.

[183] J. P. Maria *et al.*, “Cold sintering: Current status and prospects,” *J. Mater. Res.*, vol. 32, no. 17, pp. 3205–3218, 2017, doi: 10.1557/jmr.2017.262.

[184] D. Wang, H. Guo, C. S. Morandi, C. A. Randall, and S. Trolier-McKinstry, “Cold sintering and electrical characterization of lead zirconate titanate piezoelectric ceramics,” *APL Mater.*, vol. 6, no. 1, p. 016101, Jan. 2018, doi: 10.1063/1.5004420.

[185] S. Kang, H. Guo, J. Wang, X. Zhong, and B. Li, “Influence of surface coating on the microstructures and dielectric properties of BaTiO3ceramic: Via a cold sintering process,” *RSC Adv.*, vol. 10, no. 51, pp. 30870–30879, 2020, doi: 10.1039/d0ra03849k.

[186] T. Sada, K. Tsuji, A. Ndayishimiye, Z. Fan, Y. Fujioka, and C. A. Randall, “Enhanced high permittivity BaTiO 3 –polymer nanocomposites from the cold sintering process,” *J. Appl. Phys.*, vol. 128, no. 8, p. 084103, Aug. 2020, doi: 10.1063/5.0021040.

[187] K. Tsuji *et al.*, “Single Step Densification of High Permittivity BaTiO3 Ceramics at 300 °C,” *J. Eur. Ceram. Soc.*, 2019, doi: 10.1016/j.jeurceramsoc.2019.12.022.

[188] I. J. Induja and M. T. Sebastian, “Microwave dielectric properties of mineral sillimanite obtained by conventional and cold sintering process,” *J. Eur. Ceram. Soc.*, vol. 37, no. 5, pp. 2143–2147, 2017, doi: 10.1016/j.jeurceramsoc.2017.01.007.

[189] W. Bin Hong, L. Li, M. Cao, and X. M. Chen, “Plastic deformation and effects of water in room-temperature cold sintering of NaCl microwave dielectric ceramics,” *J. Am. Ceram. Soc.*, vol. 101, no. 9, pp. 4038–4043, Sep. 2018, doi: 10.1111/jace.15572.

[190] I. J. Induja and M. T. Sebastian, “Microwave dielectric properties of cold sintered Al2O3-NaCl composite,” *Mater. Lett.*, vol. 211, no. September, pp. 55–57, 2017, doi: 10.1016/j.matlet.2017.09.083.

[191] D. Wang *et al.*, “Temperature Stable Cold Sintered (Bi0.95Li0.05)(V0.9Mo0.1)O4-Na2Mo2O7 Microwave Dielectric Composites,” *Materials (Basel).*, vol. 12, no. 1370, pp. 1–10, 2019.

[192] S. S. Faouri *et al.*, “High quality factor cold sintered Li2MoO4 -

BaFe12O19 composites for microwave applications," *Acta Mater.*, vol. 166, pp. 202–207, 2019, doi: 10.1016/j.actamat.2018.12.057.

[193] D. Zhou, L. X. Pang, D. Wang, and I. M. Reaney, "Novel water-assisting low firing MoO3 microwave dielectric ceramics," *J. Eur. Ceram. Soc.*, vol. 39, no. 7, pp. 2374–2378, 2019, doi: 10.1016/j.jeurceramsoc.2019.01.052.

[194] J. Guo, H. Guo, D. Sohrabi, B. Heidary, S. Funahashi, and C. A. Randall, "Semiconducting properties of cold sintered V2O5 ceramics and Co-sintered V2O5 - PEDOT : PSS composites," *J. Eur. Ceram. Soc.*, vol. 37, pp. 1529–1534, 2017.

[195] J. A. Liu, C. H. Li, J. J. Shan, J. M. Wu, R. F. Gui, and Y. S. Shi, "Preparation of high-density InGaZnO4 target by the assistance of cold sintering," *Mater. Sci. Semicond. Process.*, vol. 84, no. April, pp. 17–23, 2018, doi: 10.1016/j.mssp.2018.04.030.

[196] Y. Liu, Q. Sun, D. Wang, K. Adair, J. Liang, and X. Sun, "Development of the cold sintering process and its application in solid-state lithium batteries," *J. Power Sources*, vol. 393, no. May, pp. 193–203, 2018, doi: 10.1016/j.jpowsour.2018.05.015.

[197] D. Wang, D. Zhou, K. Song, A. Feteira, C. A. Randall, and I. M. Reaney, "Cold-Sintered C0G Multilayer Ceramic Capacitors," *Adv. Electron. Mater.*, vol. 5, no. 7, pp. 1–5, 2019, doi: 10.1002/aelm.201900025.

[198] D. Wang *et al.*, "Direct Integration of Cold Sintered, Temperature-Stable Bi2Mo2O9-K2MoO4 Ceramics on Printed Circuit Boards for Satellite Navigation Antennas," *J. Eur. Ceram. Soc.*, vol. 40, no. 12, pp. 4029–4034, 2020, doi: 10.1016/j.jeurceramsoc.2020.04.025.

[199] D. Wang *et al.*, "Cold sintered CaTiO3-K2MoO4 microwave dielectric ceramics for integrated microstrip patch antennas," *Appl. Mater. Today*, vol. 18, p. 100519, 2020, doi: 10.1016/j.apmt.2019.100519.

[200] T. Ibn-mohammed, C. A. Randall, K. B. Mustapha, J. Guo, J. Walker, and S. Berbano, "Decarbonising ceramic manufacturing : A techno-economic analysis of energy efficient sintering technologies in the functional materials sector," *J. Eur. Ceram. Soc.*, vol. 39, no. 16, pp. 5213–5235, 2019, doi: 10.1016/j.jeurceramsoc.2019.08.011.

[201] K. Jayasayee, S. Clark, C. King, P. I. Dahl, J. R. Tolchard, and M. Juel, "Cold sintering as a cost-effective process to manufacture porous zinc electrodes for rechargeable zinc-air batteries," *Processes*, vol. 8, no. 5, pp. 1–12, 2020, doi: 10.3390/PR8050592.

[202] J. G. Pereira da Silva *et al.*, “Sintering of a sodium-based NASICON electrolyte: A comparative study between cold, field assisted and conventional sintering methods,” *J. Eur. Ceram. Soc.*, vol. 39, no. 8, pp. 2697–2702, 2019, doi: 10.1016/j.jeurceramsoc.2019.03.023.

[203] D. Sohrabi Baba Heidary, M. Lanagan, and C. A. Randall, “Contrasting energy efficiency in various ceramic sintering processes,” *J. Eur. Ceram. Soc.*, vol. 38, no. 4, pp. 1018–1029, 2018, doi: 10.1016/j.jeurceramsoc.2017.10.015.

[204] A. Indurkar, R. Choudhary, K. Rubenis, and J. Locs, “Advances in Sintering Techniques for Calcium Phosphates Ceramics,” *Materials (Basel).*, vol. 14, p. 6133, 2021, doi: doi.org/10.3390/ ma14206133.

[205] J. Cockburn and R. Boston, “Cold sintering of YBa2Cu3O7-: δ,” *RSC Adv.*, vol. 9, no. 70, pp. 40917–40923, 2019, doi: 10.1039/c9ra08744c.

[206] H. Guo, J. Guo, A. Baker, and C. A. Randall, “Cold sintering process for ZrO2-based ceramics: significantly enhanced densification evolution in yttria-doped ZrO2,” *J. Am. Ceram. Soc.*, vol. 100, no. 2, pp. 491–495, 2017, doi: 10.1111/jace.14593.

[207] M. Y. Sengul, J. Guo, C. A. Randall, and A. C. T. van Duin, “Water-Mediated Surface Diffusion Mechanism Enables the Cold Sintering Process: A Combined Computational and Experimental Study,” *Angew. Chemie Int. Ed.*, vol. 58, no. 36, pp. 12420–12424, Sep. 2019, doi: 10.1002/anie.201904738.

[208] J. Guo *et al.*, “Cold Sintering: A Paradigm Shift for Processing and Integration of Ceramics,” *Angew. Chemie - Int. Ed.*, vol. 55, no. 38, pp. 11457–11461, 2016, doi: 10.1002/anie.201605443.

[209] A. Ndayishimiye *et al.*, “Comparing Hydrothermal Sintering and Cold Sintering Process: Mechanisms, Microstructure, Kinetics and Chemistry,” *J. Eur. Ceram. Soc.*, no. November, 2019, doi: 10.1016/j.jeurceramsoc.2019.11.049.

[210] J. Gonzalez-julian *et al.*, “Unveiling the mechanisms of cold sintering of ZnO at 250 C by varying applied stress and characterizing grain boundaries by Kelvin Probe Force Microscopy,” *Acta Mater.*, vol. 144, pp. 116–128, 2018, doi: 10.1016/j.actamat.2017.10.055.

[211] S. Funahashi *et al.*, “Demonstration of the cold sintering process study for the densification and grain growth of ZnO ceramics,” *J. Am. Ceram. Soc.*, vol. 100, no. 2, pp. 546–553, Feb. 2017, doi: 10.1111/jace.14617.

[212] S. H. Bang *et al.*, “Toward a size scale-up cold sintering process at reduced uniaxial pressure,” *J. Am. Ceram. Soc.*, vol. 103, no. 4, pp. 2322–2327, Apr. 2020, doi: 10.1111/jace.16976.

[213] S. H. Bang, T. Herisson De Beauvoir, and C. A. Randall, “Densification of thermodynamically unstable tin monoxide using cold sintering process,” *J. Eur. Ceram. Soc.*, vol. 39, no. 4, pp. 1230–1236, 2019, doi: 10.1016/j.jeurceramsoc.2018.11.026.

[214] C. Yang *et al.*, “ZrW2O8 with Negative Thermal Expansion Fabricated at Ultralow Temperature: An Energy-Efficient Strategy for Metastable Material Fabrication,” *ACS Sustain. Chem. Eng.*, vol. 7, no. 17, pp. 14747–14755, 2019, doi: 10.1021/acssuschemeng.9b02682.

[215] A. Ndayishimiye, K. Tsuji, K. Wang, S. Hwi, and C. A. Randall, “Sintering mechanisms and dielectric properties of cold sintered (1-x) SiO 2 - x PTFE composites,” *J. Eur. Ceram. Soc.*, vol. 39, no. 15, pp. 4743–4751, 2019, doi: 10.1016/j.jeurceramsoc.2019.07.048.

[216] A. Ndayishimiye, Z. A. Grady, S. H. Bang, and C. A. Randall, “Thermosetting polymers in cold sintering : The fabrication of ZnO-polydimethylsiloxane composites,” no. August 2019, pp. 3039–3050, 2020, doi: 10.1111/jace.17009.

[217] M. Si *et al.*, “Preparation of zinc oxide/poly-ether-ether-ketone (PEEK) composites via the cold sintering process,” *Acta Mater.*, vol. 215, p. 117036, 2021, doi: 10.1016/j.actamat.2021.117036.

[218] N. Guo, H. Z. Shen, and P. Shen, “Cold sintering of chitosan/hydroxyapatite composites,” *Materialia*, vol. 21, no. December 2021, p. 101294, 2022, doi: 10.1016/j.mtla.2021.101294.

[219] Y. Hu *et al.*, “Cold sintering constructed in situ drug-loaded high strength HA-PLA composites: Potential bone substitution material,” *Ceram. Int.*, vol. 49, no. 7, pp. 11655–11663, 2023, doi: 10.1016/j.ceramint.2022.12.014.

[220] E. Champion, “Sintering of calcium phosphate bioceramics,” *Acta Biomater.*, vol. 9, no. 4, pp. 5855–5875, 2013, doi: 10.1016/j.actbio.2012.11.029.

[221] M. Hassan and H. J. Ryu, “Cold sintering and durability of iodate-substituted calcium hydroxyapatite (IO-HAp) for the immobilization of radioiodine,” *J. Nucl. Mater.*, vol. 514, pp. 84–89, 2019, doi: 10.1016/j.jnucmat.2018.11.024.

[222] M. ul Hassan, S. Venkatesan, and H. J. Ryu, “Non-volatile immobilization of iodine by the cold-sintering of iodosodalite,” *J. Hazard. Mater.*, vol. 386, no. May 2019, p. 121646, 2020, doi: 10.1016/j.jhazmat.2019.121646.

[223] M. ul Hassan, M. Akmal, and H. J. Ryu, “Cold sintering of as-dried nanostructured calcium hydroxyapatite without using additives,” *J. Mater. Res. Technol.*, vol. 11, pp. 811–822, 2021, doi: 10.1016/j.jmrt.2021.01.060.

[224] H. zhen Shen, N. Guo, L. Zhao, and P. Shen, “Role of ion substitution and lattice water in the densification of cold-sintered hydroxyapatite,” *Scr. Mater.*, vol. 177, pp. 141–145, 2020, doi: 10.1016/j.scriptamat.2019.10.024.

[225] H. Z. Shen, N. Guo, Y. H. Liang, and P. Shen, “Synthesis and densification of hydroxyapatite by mechanochemically-activated reactive cold sintering,” *Scr. Mater.*, vol. 194, p. 113717, 2021, doi: 10.1016/j.scriptamat.2020.113717.

[226] C. Drouet *et al.*, “Bioceramics: Spark Plasma Sintering (SPS) of Calcium Phosphates,” *Adv. Sci. Technol.*, vol. 49, pp. 45–50, Oct. 2006, doi: 10.4028/www.scientific.net/AST.49.45.

[227] O. Guillon *et al.*, “Field-assisted sintering technology/spark plasma sintering: Mechanisms, materials, and technology developments,” *Adv. Eng. Mater.*, vol. 16, no. 7, pp. 830–849, 2014, doi: 10.1002/adem.201300409.

[228] M. Nygren and Z. Shen, “On the preparation of bio-, nano- and structural ceramics and composites by spark plasma sintering,” *Solid State Sci.*, vol. 5, no. 1, pp. 125–131, 2003, doi: 10.1016/S1293-2558(02)00086-9.

[229] D. Grossin *et al.*, “Low temperature consolidation of nanocrystalline apatites. Toward a new generation of calcium phosphate ceramics,” in *33rd International Conference and Exposition on Advance Ceramics and Composites (ICACC 2009)*, 2009, no. January, doi: 10.4028/www.scientific.net/MSF.508.621.

[230] C. Ortali, I. Julien, C. Drouet, and E. Champion, “Influence of carbonation on the low-temperature consolidation by Spark Plasma Sintering of carbonated calcium phosphate bioceramics,” *Ceram. Int.*, vol. 46, no. 5, pp. 5799–5810, 2020, doi: 10.1016/j.ceramint.2019.11.030.

[231] M. Luginina *et al.*, “First successful stabilization of consolidated

amorphous calcium phosphate (ACP) by cold sintering: Toward highly-resorbable reactive bioceramics," *J. Mater. Chem. B*, vol. 8, no. 4, pp. 629–635, 2020, doi: 10.1039/c9tb02121c.

[232] F. Brouillet *et al.*, "Biomimetic apatite-based composite materials obtained by spark plasma sintering (SPS): physicochemical and mechanical characterizations," *J. Mater. Sci. Mater. Med.*, vol. 26, no. 8, pp. 1–11, 2015, doi: 10.1007/s10856-015-5553-9.

[233] C. Ortali, I. Julien, M. Vandenhende, C. Drouet, and E. Champion, "Consolidation of bone-like apatite bioceramics by spark plasma sintering of amorphous carbonated calcium phosphate at very low temperature," *J. Eur. Ceram. Soc.*, vol. 38, no. 4, pp. 2098–2109, 2018, doi: 10.1016/j.jeurceramsoc.2017.11.051.

[234] Y. Wang *et al.*, "Water-mediated structuring of bone apatite," *Nat. Mater.*, vol. 12, no. 12, pp. 1144–1153, Dec. 2013, doi: 10.1038/nmat3787.

[235] R. J. Egli, S. Gruenenfelder, N. Doebelin, W. Hofstetter, R. Luginbuehl, and M. Bohner, "Thermal treatments of calcium phosphate biomaterials to tune the physico-chemical properties and modify the in vitro osteoclast response," *Adv. Eng. Mater.*, vol. 13, no. 3, pp. 102–107, 2011, doi: 10.1002/adem.201080037.

[236] S. Al-Maawi *et al.*, "Thermal treatment at 500°C significantly reduces the reaction to irregular tricalcium phosphate granules as foreign bodies: An in vivo study," *Acta Biomater.*, vol. 142, pp. 414–429, 2022, doi: 10.1016/j.actbio.2022.01.011.

[237] A. Galotta, F. Agostinacchio, A. Motta, S. Dirè, and V. M. Sglavo, "Mechanochemical synthesis and cold sintering of mussel shell-derived hydroxyapatite nano-powders for bone tissue regeneration," *J. Eur. Ceram. Soc.*, vol. 43, no. 2, pp. 639–647, 2023, doi: 10.1016/j.jeurceramsoc.2022.09.024.

[238] F. Cestari, G. Chemello, A. Galotta, and V. M. Sglavo, "Low-temperature synthesis of nanometric apatite from biogenic sources," *Ceram. Int.*, vol. 46, no. 15, pp. 23526–23533, 2020, doi: 10.1016/j.ceramint.2020.06.123.

[239] M. M. H. Al Omari, I. S. Rashid, N. A. Qinna, and A. M. Jaber, "Calcium Carbonate," in *Profiles of Drug Substances, Excipients, and Related Methodology*, 1st ed., vol. 41, Elsevier Inc., 2016, pp. 31–132.

[240] A. Antonakos, E. Liarokapis, and T. Leventouri, "Micro-Raman and FTIR studies of synthetic and natural apatites," *Biomaterials*, vol. 28,

no. 19, pp. 3043–3054, 2007, doi: 10.1016/j.biomaterials.2007.02.028.

[241] M. Frasnelli *et al.*, "Synthesis and characterization of strontium-substituted hydroxyapatite nanoparticles for bone regeneration," *Mater. Sci. Eng. C*, vol. 71, pp. 653–662, Feb. 2017, doi: 10.1016/j.msec.2016.10.047.

[242] L. Stipniece *et al.*, "Strontium substituted hydroxyapatite promotes direct primary human osteoblast maturation," *Ceram. Int.*, vol. 47, no. 3, pp. 3368–3379, 2021, doi: 10.1016/j.ceramint.2020.09.182.

[243] E. Landi *et al.*, "Biomimetic Mg- and Mg,CO3-substituted hydroxyapatites: synthesis characterization and in vitro behaviour," *J. Eur. Ceram. Soc.*, vol. 26, no. 13, pp. 2593–2601, Jan. 2006, doi: 10.1016/j.jeurceramsoc.2005.06.040.

[244] C. F. Ramirez-gutierrez, S. M. Londoño-restrepo, A. Real, and M. A. Mondragón, "Effect of the temperature and sintering time on the thermal , structural , morphological , and vibrational properties of hydroxyapatite derived from pig bone," *Ceram. Int.*, vol. 43, no. 10, pp. 7552–7559, 2017, doi: 10.1016/j.ceramint.2017.03.046.

[245] E. Barua, A. Das, D. Pamu, A. B. Deoghare, P. Deb, and S. Das, "Effect of thermal treatment on the physico-chemical properties of bioactive hydroxyapatite derived from caprine bone bio-waste," *Ceram. Int.*, vol. 45, no. 17, pp. 23265–23277, 2019, doi: 10.1016/j.ceramint.2019.08.023.

[246] A. Galotta, K. Rubenis, J. Locs, and V. M. Sglavo, "Dissolution-precipitation synthesis and cold sintering of mussel shells-derived hydroxyapatite and hydroxyapatite/chitosan composites for bone tissue engineering," *Open Ceram.*, vol. 15, p. 100418, Sep. 2023, doi: 10.1016/j.oceram.2023.100418.

[247] M. M. Almeida *et al.*, "Strontium ranelate increases osteoblast activity," *Tissue Cell*, vol. 48, no. 3, pp. 183–188, 2016, doi: 10.1016/j.tice.2016.03.009.

[248] J. E. Fonseca and M. L. Brandi, "Mechanism of action of strontium ranelate: What are the facts?," *Clin. Cases Miner. Bone Metab.*, vol. 7, no. 1, pp. 17–18, 2010.

[249] P. Horák, M. Skácelová, and A. Kazi, "Role of Strontium Ranelate in the Therapy of Osteoporosis," *J. Rheum. Dis. Treat.*, vol. 3, no. 2, pp. 1–6, 2017, doi: 10.23937/2469-5726/1510050.

[250] T. A. Rodrigues *et al.*, "Prophylactic and therapeutic use of strontium

ranelate reduces the progression of experimental osteoarthritis," *Front. Pharmacol.*, vol. 9, no. SEP, pp. 1–9, 2018, doi: 10.3389/fphar.2018.00975.

[251] M. Pilmane, K. Salma-Ancane, D. Loca, J. Locs, and L. Berzina-Cimdina, "Strontium and strontium ranelate: Historical review of some of their functions," *Mater. Sci. Eng. C*, vol. 78, pp. 1222–1230, 2017, doi: 10.1016/j.msec.2017.05.042.

[252] D. Loca *et al.*, "Development of local strontium ranelate delivery systems and long term in vitro drug release studies in osteogenic medium," *Sci. Rep.*, vol. 8, no. 1, pp. 1–10, 2018, doi: 10.1038/s41598-018-35197-7.

[253] C. W. Chiang *et al.*, "Facilitated and controlled strontium ranelate delivery using gcs-ha nanocarriers embedded into pegda coupled with decortication driven spinal regeneration," *Int. J. Nanomedicine*, vol. 16, no. August 2020, pp. 4209–4224, 2021, doi: 10.2147/IJN.S274461.

[254] A. Svarca *et al.*, "Calcium Phosphate/Hyaluronic Acid Composite Hydrogels for Local Antiosteoporotic Drug Delivery," *Front. Bioeng. Biotechnol.*, vol. 10, no. July, pp. 1–21, 2022, doi: 10.3389/fbioe.2022.917765.

[255] E. W. D. Huffman, "Performance of a new automatic carbon dioxide coulometer," *Microchem. J.*, vol. 22, no. 4, pp. 567–573, Dec. 1977, doi: 10.1016/0026-265X(77)90128-X.

[256] A. Gee and V. R. Deitz, "Determination of Phosphate by Differential Spectrophotometry," *Anal. Chem.*, vol. 25, no. 9, pp. 1320–1324, 1953, doi: 10.1021/ac60081a006.

[257] K. A. Hing, S. M. Best, and W. Bonfield, "Characterization of porous hydroxyapatite," *J. Mater. Sci. Mater. Med.*, vol. 10, no. 3, pp. 135–145, 1999, doi: 10.1023/A:1008929305897.

[258] Y. Chen and X. Miao, "Thermal and chemical stability of fluorohydroxyapatite ceramics with different fluorine contents," *Biomaterials*, vol. 26, no. 11, pp. 1205–1210, 2005, doi: 10.1016/j.biomaterials.2004.04.027.

[259] S. Brahimi *et al.*, "Preparation and characterization of biocomposites based on chitosan and biomimetic hydroxyapatite derived from natural phosphate rocks," *Mater. Chem. Phys.*, vol. 276, no. August 2021, 2022, doi: 10.1016/j.matchemphys.2021.125421.

[260] A. Zając, J. Hanuza, M. Wandas, and L. Dymińska, "Determination of

N-acetylation degree in chitosan using Raman spectroscopy," *Spectrochim. Acta Part A Mol. Biomol. Spectrosc.*, vol. 134, pp. 114–120, Jan. 2015, doi: 10.1016/j.saa.2014.06.071.

[261] B. Gieroba *et al.*, "Surface Chemical and Morphological Analysis of Chitosan/1,3-β-D-Glucan Polysaccharide Films Cross-linked at 90 °C," *Int. J. Mol. Sci.*, vol. 23, no. 11, pp. 1–23, 2022, doi: 10.3390/ijms23115953.

[262] F. A. Shah, "Characterization of Synthetic Hydroxyapatite Fibers Using High-Resolution, Polarized Raman Spectroscopy," *Appl. Spectrosc.*, vol. 75, no. 4, pp. 475–479, 2021, doi: 10.1177/0003702820942540.

[263] J. A. Stammeier, B. Purgstaller, D. Hippler, V. Mavromatis, and M. Dietzel, "In-situ Raman spectroscopy of amorphous calcium phosphate to crystalline hydroxyapatite transformation," *MethodsX*, vol. 5, no. October, pp. 1241–1250, 2018, doi: 10.1016/j.mex.2018.09.015.

[264] P. E. Timchenko *et al.*, "Experimental studies of hydroxyapatite by Raman spectroscopy," *J. Opt. Technol.*, vol. 85, no. 3, p. 130, 2018, doi: 10.1364/jot.85.000130.

[265] Z. Ansari *et al.*, "In-Situ Synthesis and Characterization of Chitosan/Hydroxyapatite Nanocomposite Coatings to Improve the Bioactive Properties of Ti6Al4V Substrates," *Materials (Basel).*, vol. 13, no. 17, p. 3772, Aug. 2020, doi: 10.3390/ma13173772.

[266] A. Rogina, M. Ivanković, and H. Ivanković, "Preparation and characterization of nano-hydroxyapatite within chitosan matrix," *Mater. Sci. Eng. C*, vol. 33, no. 8, pp. 4539–4544, 2013, doi: 10.1016/j.msec.2013.07.008.

[267] J. Li, D. Zhu, J. Yin, Y. Liu, F. Yao, and K. Yao, "Formation of nano-hydroxyapatite crystal in situ in chitosan-pectin polyelectrolyte complex network," *Mater. Sci. Eng. C*, vol. 30, no. 6, pp. 795–803, 2010, doi: 10.1016/j.msec.2010.03.011.

[268] S. A. Siddiqi and U. Azhar, *Carbonate substituted hydroxyapatite*. Elsevier Ltd, 2019.

[269] I. Cacciotti, "Cationic and Anionic Substitutions in Hydroxyapatite," in *Handbook of Bioceramics and Biocomposites*, Cham: Springer International Publishing, 2016, pp. 145–211.

[270] J. Sang Cho *et al.*, "Enhanced osteoconductivity of sodium-substituted hydroxyapatite by system instability," *J. Biomed. Mater. Res. - Part B*, vol. 102, no. 5, pp. 1046–1062, 2014, doi: 10.1002/jbm.b.33087.

[271] A. Shavandi, A. E. D. A. Bekhit, A. Ali, and Z. Sun, “Synthesis of nano-hydroxyapatite (nHA) from waste mussel shells using a rapid microwave method,” *Mater. Chem. Phys.*, vol. 149, pp. 607–616, 2015, doi: 10.1016/j.matchemphys.2014.11.016.

[272] S. Cazalbou, C. Combes, D. Eichert, and C. Rey, “Adaptative physico-chemistry of bio-related calcium phosphates,” *J. Mater. Chem.*, vol. 14, no. 14, p. 2148, 2004, doi: 10.1039/b401318b.

[273] D. Eichert, C. Combes, C. Drouet, and C. Rey, “Formation and Evolution of Hydrated Surface Layers of Apatites,” *Key Eng. Mater.*, vol. 284–286, no. 3, pp. 3–6, Apr. 2005, doi: 10.4028/www.scientific.net/KEM.284-286.3.

[274] Y. Jiang, Z. Yuan, and J. Huang, “Substituted hydroxyapatite: a recent development,” *Mater. Technol.*, vol. 35, no. 11–12, pp. 785–796, Oct. 2020, doi: 10.1080/10667857.2019.1664096.

[275] A. Arbel, I. Katz, and S. Sarig, “Dissolution of hydroxyapatite by calcium complexing agents,” *J. Cryst. Growth*, vol. 110, no. 4, pp. 733–738, 1991, doi: 10.1016/0022-0248(91)90630-N.

[276] D. S. Seo and J. K. Lee, “Synthesis of hydroxyapatite whiskers through dissolution-reprecipitation process using EDTA,” *J. Cryst. Growth*, vol. 310, no. 7–9, pp. 2162–2167, 2008, doi: 10.1016/j.jcrysgro.2007.11.028.

[277] H. Verplaetse, R. M. H. Verbeeck, A. Verbaeys, and W. Oosterlinck, “Solubility of calcium oxalate monohydrate and hydroxyapatite in EDTA solutions,” *J. Urol.*, vol. 135, no. 3, pp. 608–611, 1986, doi: 10.1016/S0022-5347(17)45760-0.

[278] U. Anjaneyulu, B. Priyadarshini, S. Arul Xavier Stango, M. Chellappa, M. Geetha, and U. Vijayalakshmi, “Preparation and characterisation of sol–gel-derived hydroxyapatite nanoparticles and its coatings on medical grade Ti-6Al-4V alloy for biomedical applications,” *Mater. Technol.*, vol. 32, no. 13, pp. 800–814, 2017, doi: 10.1080/10667857.2017.1364476.

[279] F. Bakan, O. Laçin, and H. Sarac, “A novel low temperature sol-gel synthesis process for thermally stable nano crystalline hydroxyapatite,” *Powder Technol.*, vol. 233, pp. 295–302, 2013, doi: 10.1016/j.powtec.2012.08.030.

[280] R. N. Panda, M. F. Hsieh, R. J. Chung, and T. S. Chin, “FTIR, XRD, SEM and solid state NMR investigations of carbonate-containing hydroxyapatite nano-particles synthesized by hydroxide-gel

technique," *J. Phys. Chem. Solids*, vol. 64, no. 2, pp. 193–199, 2003, doi: 10.1016/S0022-3697(02)00257-3.

[281] T. Witoon, "Characterization of calcium oxide derived from waste eggshell and its application as CO2 sorbent," *Ceram. Int.*, vol. 37, no. 8, pp. 3291–3298, 2011, doi: 10.1016/j.ceramint.2011.05.125.

[282] S. Pramanik, A. K. Agarwal, K. N. Rai, and A. Garg, "Development of high strength hydroxyapatite by solid-state-sintering process," *Ceram. Int.*, vol. 33, no. 3, pp. 419–426, Apr. 2007, doi: 10.1016/j.ceramint.2005.10.025.

[283] K. Yoshida *et al.*, "Reaction sintering of β-tricalcium phosphates and their mechanical properties," *J. Eur. Ceram. Soc.*, vol. 27, no. 10, pp. 3215–3220, 2007, doi: 10.1016/j.jeurceramsoc.2006.12.004.

[284] S. Kobayashi and T. Murakoshi, "Characterization of mechanical properties and bioactivity of hydroxyapatite/β-tricalcium phosphate composites," *Adv. Compos. Mater.*, vol. 23, no. 2, pp. 163–177, 2013, doi: 10.1080/09243046.2013.844897.

[285] J. E. Ritter, K. Jakus, A. Batakis, and N. Bandyopadhyay, "Appraisal of biaxial strength testing," *J. Non. Cryst. Solids*, vol. 38–39, pp. 419–424, 1980, doi: 10.1016/0022-3093(80)90455-X.

[286] A. Börger, P. Supancic, and R. Danzer, "The ball on three balls test for strength testing of brittle discs: stress distribution in the disc," *J. Eur. Ceram. Soc.*, vol. 22, pp. 1425–1436, 2002, doi: https://doi.org/10.1016/S0955-2219(01)00458-7.

[287] C. Xianmiao, L. Yubao, Z. Yi, Z. Li, L. Jidong, and W. Huanan, "Properties and in vitro biological evaluation of nano-hydroxyapatite/chitosan membranes for bone guided regeneration," *Mater. Sci. Eng. C*, vol. 29, no. 1, pp. 29–35, 2009, doi: 10.1016/j.msec.2008.05.008.

[288] A. Satpathy *et al.*, "Bioactive Nano-Hydroxyapatite Doped Electrospun PVA-Chitosan Composite Nanofibers for Bone Tissue Engineering Applications," *J. Indian Inst. Sci.*, vol. 99, no. 3, pp. 289–302, 2019, doi: 10.1007/s41745-019-00118-8.

[289] H. Z. Shen, N. Guo, Y. Liang, and P. Shen, "Synthesis and densification of hydroxyapatite by mechanochemically-activated reactive cold sintering," *Scr. Mater.*, vol. 194, p. 113717, 2021, doi: 10.1016/j.scriptamat.2020.113717.

[290] I. Reis Lavagnini, J. V. Campos, A. G. Storion, A. O. Lobo, R. Raj, and E. Maria de Jesus Agnolon Pallone, "Influence of flash sintering on phase transformation and conductivity of hydroxyapatite," *Ceram. Int.*, vol. 47, no. 7, pp. 9125–9131, 2021, doi: 10.1016/j.ceramint.2020.12.036.

[291] F. Liu, J. Zhang, P. Liu, Q. Deng, and D. He, "Strengthening of alumina ceramics under cold compression," *Ceram. Int.*, vol. 46, no. 3, pp. 3984–3988, Feb. 2020, doi: 10.1016/j.ceramint.2019.09.257.

[292] A. J. Ruys, M. Wei, C. C. Sorrell, M. R. Dickson, A. Brandwood, and B. K. Milthorpe, "Sintering effects on the strength of hydroxyapatite," *Biomaterials*, vol. 16, no. 5, pp. 409–415, 1995, doi: 10.1016/0142-9612(95)98859-C.

[293] F. Heidari *et al.*, "Mechanical properties of natural chitosan/hydroxyapatite/magnetite nanocomposites for tissue engineering applications," *Mater. Sci. Eng. C*, vol. 65, pp. 338–344, 2016, doi: 10.1016/j.msec.2016.04.039.

[294] L. Feng, M. Chittenden, J. Schirer, M. Dickinson, and I. Jasiuk, "Mechanical properties of porcine femoral cortical bone measured by nanoindentation," *J. Biomech.*, vol. 45, no. 10, pp. 1775–1782, 2012, doi: 10.1016/j.jbiomech.2012.05.001.

[295] A. Ibrahim, N. Magliulo, J. Groben, A. Padilla, F. Akbik, and Z. Abdel Hamid, "Hardness, an Important Indicator of Bone Quality, and the Role of Collagen in Bone Hardness," *J. Funct. Biomater.*, vol. 11, no. 85, pp. 1–10, Dec. 2020, doi: 10.3390/jfb11040085.

[296] M. L. Lau, K. T. Lau, H. Ku, F. Cardona, and J. H. Lee, "Analysis of heat-treated bovine cortical bone by thermal gravimetric and nanoindentation," *Compos. Part B Eng.*, vol. 55, pp. 447–452, 2013, doi: 10.1016/j.compositesb.2013.06.027.

[297] X. WANG, X. CHEN, P. HODGSON, and C. WEN, "Elastic modulus and hardness of cortical and trabecular bovine bone measured by nanoindentation," *Trans. Nonferrous Met. Soc. China*, vol. 16, pp. s744–s748, Jun. 2006, doi: 10.1016/S1003-6326(06)60293-8.

[298] P. K. Zysset, X. Edward Guo, C. Edward Hoffler, K. E. Moore, and S. A. Goldstein, "Elastic modulus and hardness of cortical and trabecular bone lamellae measured by nanoindentation in the human femur," *J. Biomech.*, vol. 32, no. 10, pp. 1005–1012, Oct. 1999, doi: 10.1016/S0021-9290(99)00111-6.

[299] W. wei Wu *et al.*, "Bone Hardness of Different Anatomical Regions of

Human Radius and its Impact on the Pullout Strength of Screws," *Orthop. Surg.*, vol. 11, no. 2, pp. 270–276, 2019, doi: 10.1111/os.12436.

[300] Y. W. Gu, K. A. Khor, and P. Cheang, "In vitro studies of plasma-sprayed hydroxyapatite/Ti-6Al-4V composite coatings in simulated body fluid (SBF)," *Biomaterials*, vol. 24, no. 9, pp. 1603–1611, 2003, doi: 10.1016/S0142-9612(02)00573-2.

[301] Y. W. Gu, K. A. Khor, and P. Cheang, "Bone-like apatite layer formation on hydroxyapatite prepared by spark plasma sintering (SPS)," *Biomaterials*, vol. 25, no. 18, pp. 4127–4134, Aug. 2004, doi: 10.1016/j.biomaterials.2003.11.030.

[302] A. Zima, "Hydroxyapatite-chitosan based bioactive hybrid biomaterials with improved mechanical strength," *Spectrochim. Acta - Part A Mol. Biomol. Spectrosc.*, vol. 193, pp. 175–184, 2018, doi: 10.1016/j.saa.2017.12.008.

[303] X. Huang and C. S. Brazel, "On the importance and mechanisms of burst release in matrix-controlled drug delivery systems," *J. Control. Release*, vol. 73, no. 2–3, pp. 121–136, Jun. 2001, doi: 10.1016/S0168-3659(01)00248-6.

[304] P. Colombo, R. Bettini, P. Santi, A. De Ascentiis, and N. A. Peppas, "Analysis of the swelling and release mechanisms from drug delivery systems with emphasis on drug solubility and water transport," *J. Control. Release*, vol. 39, no. 2–3, pp. 231–237, 1996, doi: 10.1016/0168-3659(95)00158-1.